Direct Numerical Simulation of Turbulent Flow over a Dimpled Flat Plate Using an Immersed Boundary Technique

by

Jeremiah J. Gutierrez-Jensen

A Thesis Presented in Partial Fulfillment
of the Requirements for the Degree
Master of Science

Approved November 2010 by the
Graduate Supervisory Committee:

Kyle Squires, Chair
Marcus Herrmann
Anne Gelb

ARIZONA STATE UNIVERSITY

December 2011

ABSTRACT

Many methods of passive flow control rely on changes to surface morphology. Roughening surfaces to induce boundary layer transition to turbulence and in turn delay separation is a powerful approach to lowering drag on bluff bodies. While the influence in broad terms of how roughness and other means of passive flow control to delay separation on bluff bodies is known, basic mechanisms are not well understood. Of particular interest for the current work is understanding the role of surface dimpling on boundary layers. A computational approach is employed and the study has two main goals. The first is to understand and advance the numerical methodology utilized for the computations. The second is to shed some light on the details of how surface dimples distort boundary layers and cause transition to turbulence. Simulations are performed of the flow over a simplified configuration: the flow of a boundary layer over a dimpled flat plate. The flow is modeled using an immersed boundary as a representation of the dimpled surface along with direct numerical simulation of the Navier-Stokes equations. The dimple geometry used is fixed and is that of a spherical depression in the flat plate with a depth-to-diameter ratio of 0.1. The dimples are arranged in staggered rows separated by spacing of the center of the bottom of the dimples by one diameter in both the spanwise and streamwise dimensions. The simulations are conducted for both two and three staggered rows of dimples. Flow variables are normalized at the inlet by the dimple depth and the Reynolds number is specified as 4000 (based on freestream velocity and inlet boundary layer thickness). First and second order statistics show the turbulent boundary layers correlate well to channel flow and flow of a zero pressure gradient flat plate boundary layers in the viscous sublayer and the buffer layer, but deviates further away from the wall. The forcing of transition to turbulence by the dimples is unlike the transition caused by a naturally transitioning flow, a small perturbation such as trip tape in experimental flows, or noise in the inlet condition for computational flows.

TABLE OF CONTENTS

LIST OF TABLES

LIST OF FIGURES

Figure Page

Figure Page

I. INTRODUCTION

There exists a need to increase performance for a variety of flow conditions and as such the need for passive flow control. The desire for passive flow control has risen out of this and as such further understanding of the influence of dimples in turbulent flow as a boundary layer modifier is needed. In general, the method for passive flow control is some sort of change in surface morphology by either roughening of the surface, addition of porous media or by dimpling. The applications for this vary greatly from adding bumps on the surface in order to reduce shear stress on the surface [3] to dimpling of golf balls, which delays separation of the flow, which reduces drag for a longer drive. The same effect can also be used to delay separation on turbine blades in a low pressure environment [4]. Also, addition of a porous media to reduce drag has been observed [5]. Modification of surface morphology by adding dimples will induce turbulent transition, which changes the flow characteristics. While the result of the influence of the dimples is understood, the fundamental mechanisms that cause this are not very well understood .

For the present thesis, the Navier-Stokes (NS) equations are modified to be represent incompressible flow and are nondimensionalized for solution over a surface geometry using Computational Fluid Dynamics (CFD). CFD offers the ability to solve complex flows that are difficult to solve analytically or experimentally in a practical sense. The limitations of mathematics to solve the governing equations directly using an analytical approach are beyond present capability due to the closure problem as explained by [6], and the inability to create a robust experiment in the lab has given CFD a niche in the general field of Fluid Dynamics. In addition, many complex turbulent flow features may be thoroughly investigated over a computational domain, which are difficult to tease out of an experiment. Boundary conditions used are designed such that the flow characteristics of interest are isolated as much as possible from other effects as well. For example, the inlet velocity profile is a scaled Blasius profile, and the velocity at the top surface of the computational domain is also prescribed by using the Blasius solution.

This thesis employs a direct numerical simulation (DNS) to solve the incompressible Navier-Stokes equations on a staggered mesh using a fractional step method with a Runge-Kutta (RK) time advancement method. The surface geometry is represented by an immersed boundary (IB) imposed on the computational domain. For this method, all of the scales of turbulence are resolved without the use of a turbulence model.

Fundamental understanding of the influence of the dimple on the boundary layer is investigated in this thesis. The example of surface dimpling most commonly thought of is of course a golf ball, shown in Figure 1. The scope of the present study is limited to the investigating the flow over a dimple, and as such the flow over an entire golf ball is not necessary to understand the fundamental influence of dimples on the flow. In order to eliminate extraneous factors that will confound the results obtained by using a geometry that is more complex than what is required, a flat plate is employed. The plate represents a surface geometry that is similar to a section of the surface geometry of a golf ball without curvature. Simplification of the geometry to achieve this provides two advantages. The first is that the computational setup is simplified, and the second is that the results isolate the effect of the dimples on the boundary layer. The geometry used for this thesis is a flat plate that is immersed near the bottom of the computational domain. For the initial simulation, the flow is computed for a plate without any dimpling. Addition of dimples in a staggered array on the plate, shown for the two row configuration in Figure 2, is a simplified configuration of a golf ball. After evaluating the flow properties from this simulation the addition of a third row was added downstream of the second dimple row to further understand cumulative effects of the dimples on the boundary layer. For the present thesis the depth, d, of the dimples considered is used as the reference length. The diameter of the dimple, D, is $10d$ and the spacing from center to center of the bottom of the dimples is $\sqrt{2}D$ since the spacing in the streamwise and spanwise dimension is 1.0 for both.

A. Background

In order to understand how a dimpled surface influences boundary layer flow, this thesis investigates the influence of dimples and dimple arrangement on a flat plate. This simple case is an approximation of what occurs on the surface of a golf ball. The motivation

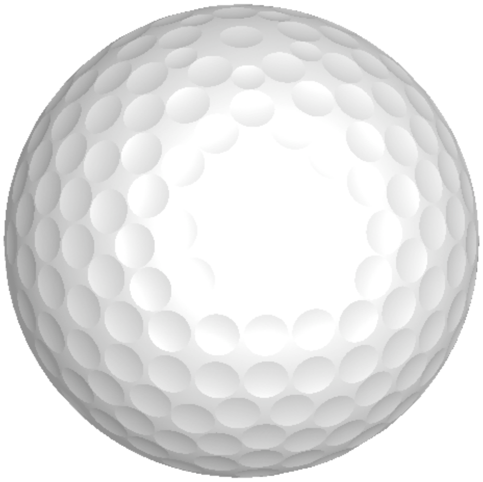

Figure 1. Dimpled surface of a golf ball.

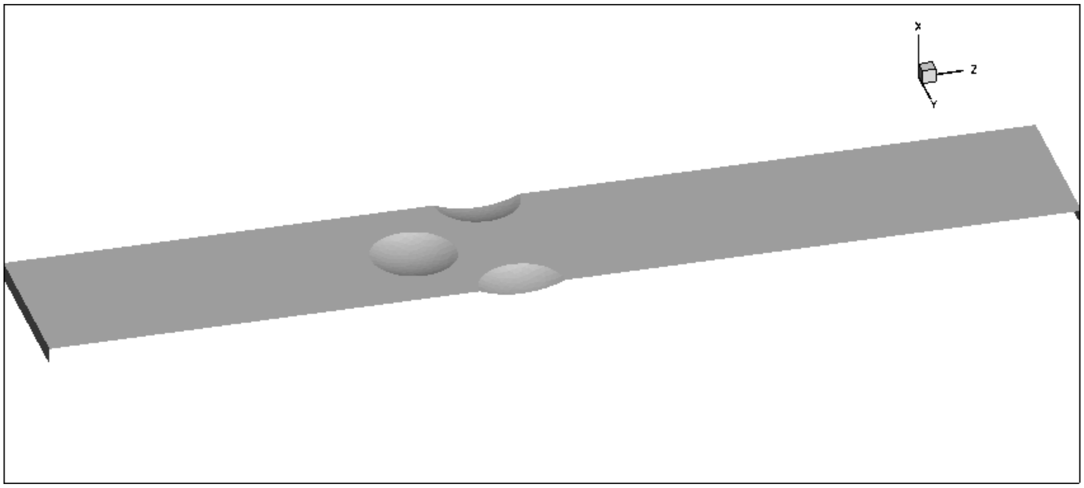

Figure 2. Immersed boundary geometry used in this simulation is a flat plate with staggered rows of dimples.

behind this thesis is to understand fundamentally the characteristics of the turbulence as a direct result of the influence from a dimple. In the golf ball case, the dimpling of the surface modifies the boundary layer such that the separation occurs further downstream along the surface of the ball. This results in a modification of the boundary layer, and understanding the modification of the surface morphology by addition of dimples on the flow is the motivation for the present work.

For the present work, The flow upstream of the dimple rows is laminar, transitions due to influence of the dimples on the boundary layer and becomes turbulent downstream. Isolation of the effect that the dimple has on the boundary layer is desired. Choosing the correct boundary conditions for the flow has a profound impact on how much the effect of the dimples is "felt" by the flow. The inlet condition is chosen such that it is a Blasius solution for a flat plate boundary layer. This condition helps to isolate the effect of the dimples and excludes the vorticity that is produced by a uniform velocity profile at the inlet near the wall. Prescribing an inlet profile such as this is also used in [2] , so that the transition to turbulence is captured by the solution. For [7], [8], [9], and [10] the inflow is a fully turbulent boundary layer. For [11] the approach to the inflow is to include low level disturbances in the boundary layer at the inlet to establish viable turbulence downstream. For the present thesis the transition to turbulence due to the dimples is desired and characterization of the resulting turbulent boundary layer is examined so the induced turbulence by the inlet is not considered. Additionally, preliminary simulations showed that the flow becomes turbulent if a uniform inlet condition is prescribed. Additionally, the intensity of the interaction of dimples in the flow depends on the ratio of the boundary layer height to the depth of the dimple. If the boundary layer is too large the dimple will have little effect on the overall characteristics of the flow, and will not cause turbulence in the flow. The dimples will force a transition in the flow from laminar upstream to turbulent downstream. The transition would not otherwise occur without the dimples. Simulations were run in order to determine if the flow would be turbulent with only a flat plate for the same flow conditions that showed that the boundary layer will remain laminar. The inlet conditions were altered to include random noise perturbations in the inlet boundary layer. The results showed that the boundary layer would not sustain turbulence.

The rows are staggered in order to simulate similar arrangement of dimples [12, 5, 13, 14, 15]. In [16] a non-staggered array was employed. After simulation over one dimpled geometry with two rows of dimples it was hypothesized that adding a third dimple row would cause a cumulative effect in the turbulence characteristics downstream of the dimple rows. The dimple geometry considered for this thesis is shown in Figure 3, where the depth, $d = 1.0$ and diameter, $D = 10.0$. Schematics of the dimple, and the dimple array configurations for two and three rows simulations are shown in Figures 3–5, respectively.

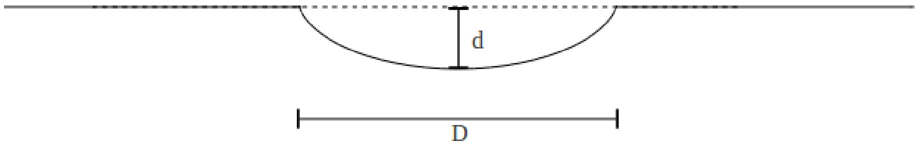

Figure 3. Schematic of a cross section of the dimple.

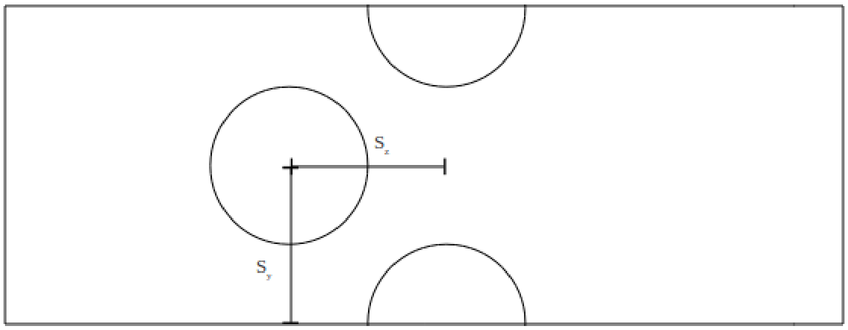

Figure 4. Schematic of 2 row dimple configuration.

1. Coordinate System

For the present thesis the coordinate system used is nonstandard. The streamwise component is z, the wall normal component is x, and the spanwise component is y. The computational grid used is a staggered grid with each component of velocity on the face and the pressure at the cell center. The schematic of the coordinate system is shown in Figure 6.

2. DNS of Wall Bounded Turbulent Flows

Much of the research for turbulent flow over a flat plate with zero pressure gradient has been an extension of the work done in [7], where flow over a zero pressure gradient flat plate was characterized in detail for $Re_\theta = 225$ to $Re_\theta = 1410$ in a statistical manner. For the present

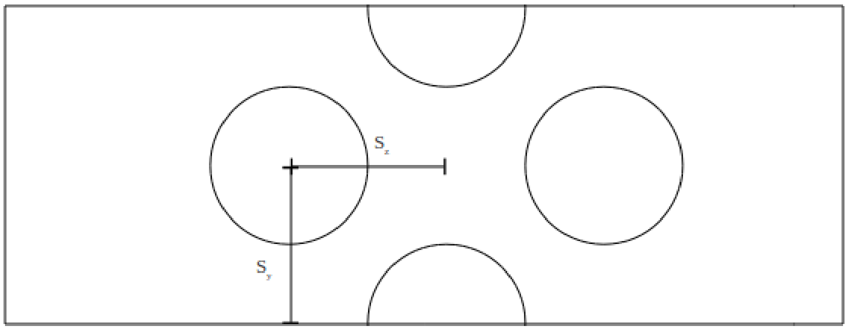

Figure 5. Schematic of 3 row dimple configuration.

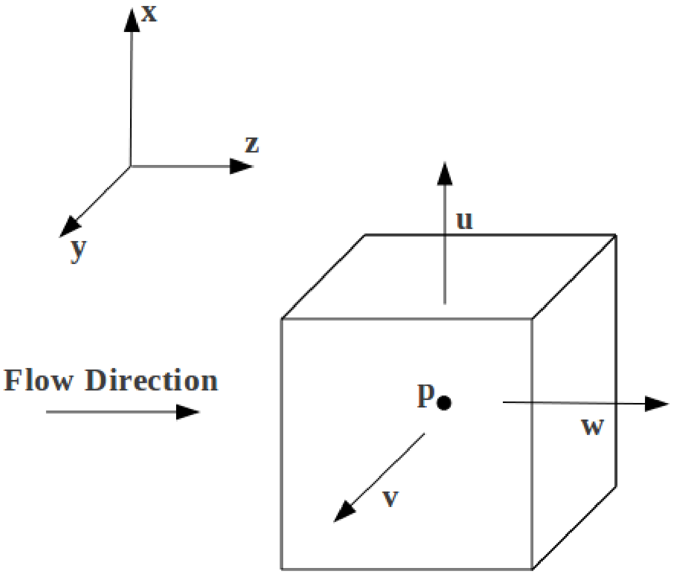

Figure 6. Schematic coordinate system for staggered grid with volume element. The velocity components u, v, and w are shown on the faces, and the pressure, p, is computed at the center of the volume element.

thesis, the θ subscript denoting the length scale of interest is the momentum thickness, θ. The experimental setup was fundamental enough for following work regarding flat plate DNS to be based upon it. The results by [7] are used in the present study along with results from [1], [2] and [9] to show how the turbulence downstream of the dimple rows compares well to previous work.

Many DNS for turbulent flows over flat plate geometries have often employed periodic condition on the streamwise velocity such as in [2] and [7]. The turbulence observed is characterized as self-sustaining and statistically predictable as in [7]. For the present thesis, the turbulent transition is forced to occur at a point upstream of the critical local Reynolds number by the dimples. The flow at the inlet is a laminar Blasius boundary layer profile and the flow remains laminar upstream of the dimples. This is done in order to show the effect that the dimples have in causing a trip in the boundary layer. Since the value of Re_z is less than the critical $Re_z = 3 \times 10^6$ based on a virtual origin upstream of the computational domain, which would permit the flow to become turbulent, the flow has been perturbed in such away as to induce a turbulent boundary layer at a location upstream of the critical Re_z.

Flow structures characteristic of flow over flat plate experiments are compared to the results in the present thesis. Isosurfaces of the second invariant of the velocity gradient tensor reveal flow structures in [2] and [17]. Development of vortical structures known as hairpin vorticies begin at the wall as streamwise vorticies. As these structures grow the vorticity induced by the structures themselves cause a turn away from the wall where they take on the characteristic hairpin structure as they grow [17].

3. *Modified Surface Investigations*

Since the dimples force turbulent production directly in the boundary layer, turbulence is of primary interest here. The interaction of the dimples with the boundary layer perturbs the boundary layer in such a manner to foster transition to turbulence that is correlated to an effective surface roughness. In [12] it was shown that there are a pair of longitudinal vortical structures that are shed from dimples in an array shown in an experiment, which occur with periodicity and are continuous. The result is inflow advection into the dimple cavity. The turbulent structures that occur as a result of surface dimpling are predictable and correlated to the Reynolds normal stress and mixing [12]. The vortical structures observed are also seen in smoke visualization in [15].

Dimples in channel flow have been shown to augmenting properties of flow in a heat transfer. A parametric study of dimples in an array with various geometries for a depth to diameter ratio of 0.3 was done in [14]. The results from [14] showed that the spherical dimples and tilted cylindrical dimple arrays offer the most significant change in heat transfer characteristics as well as eddy diffusivity of both heat and momentum. In [18] experiments were conducted that showed flow structures similar to those in [13] and [15] for $d/D = 0.2$, for [13] $d/D = 0.3$ and for [15] $d/D = 0.2$. Streamwise vortical structures are produced along the edges of the dimples as well as in the center of the dimples [18]. Additionally, impinging a jet normal to a dimpled flat plate has shown that separated flow caused by the dimple on the surface reduced heat transfer to the plate from the working fluid [19].

Alternatively, In [16] dimple shaped bumps were used to represent effective roughness correlated to known flow through duct data by using a friction factor. The results in [16] show that the heat transfer can be enhanced considerably by employing the surface roughness. Even though the surface modification is by way of of raising the surface as opposed to dimpling, using a depression in the surface can be considered to be a roughened surface. The dimple-shape used for [16] has a ratio of the height to diameter of 1.

4. Concerning Golf Balls

Direct numerical simulations performed by [20] show that the turbulent structures revealed by the instantaneous vorticity resulting from the dimples on the golf ball have length scales of the same size as the dimples themselves. It was shown in [20] that there exist shear layers that begin at the leading edge of the dimple, and is similar to observations from both [21] and shear layers resulting from the separation bubble from [11].

Experiments in [21] showed that the dimples on the golf ball will delay the separation by causing instabilities in the shear layer along the ball by causing local flow separation. The turbulence intensity is increased significantly in the shear layer as a result [21]. How effective the dimples are can be related to the effective surface roughness of the ball [20]. Though viewing the surface morphology of a golf ball in a similar manner to surface roughness, it should be noted that a “sand” rough surface that does not have the coherent dimple structures does not behave the same way aerodynamically as a gold ball [22]. The difference between a rough sphere and a dimpled sphere is primarily in the relationship of the drag as a function of Reynolds number. The drag coefficient, C_D, does not recover to a higher value as in a “sand roughened” sphere, but instead remains lower in the higher Re_D regime. In research on the aerodynamics of golf balls it is effective to consider the roughness of the ball in terms of the ratio of the depth of the dimple to the maximum diameter of the ball, k/D. In [20] $k/D = 6 \times 10^{-3}$, in [22] $k/D = 9 \times 10^{-3}$, and in [21] $k/D = 4 \times 10^{-3}$. To appropriately compare the roughness of the dimpled region, the imprint diameter of the dimple is used to scale the dimple to the golf ball so for the present study, $k/D = 9.5 \times 10^{-3}$.

The overall drag characteristics are compared using the coefficient of drag, C_D. The results in [20] coincide with the results in [22] very well, but are slightly different than [21]. The differences in the C_D curves between [22] and [21] are small, but a result in the differnce in the dimples.

5. *On Bypass Transition*

Normal transition to turbulence occurs on an orderly path marked by growth of Tollmien-Schlichting waves that eventually break down the laminar flow [23]. Bypass transition is defined as the mode of transition to turbulence that bypasses development of Tollmien-Schlichting instabilities to transition to turbuelence. Direct numerical simulations done in [24] show the structures of bypass transition by use of a DNS. Free stream disturbances cause inception of the transistion by creating a turbulent spot that occurs as a result of the perturbation of the boundary layer. The spot rings modes within the boundary layer that grows into streamwise streaks that turn to a turbulent boundary layer downstream [24].

Bypass transition has been investigated extensively by perturbation of the boundary layer by turbulence that exists in the free stream that causes the boundary layer to bypass the orderly transition. In [25] investigation of the interaction of continuous modes with the bypass transition. They found that with only two Orr-Sommerfeld modes at the inlet are used to describe the non-linear mode development in the boundary layer by using a penetrating mode [25]. Further investigation in [23] of this by using a similar method of DNS to investigate the coupling coefficient to identify the penetration depth to investigate the effect on bypass transition. As the penetration increases in the boundary layer the intensity of the turbulent spots increases as well [23] indicating that the spot inception is similar to a Kelvin-Helmholtz type of instability. As the instability grows through the boundary layer as a result of this inception, which is dependent on the mode in the free-stream disturbance.

In the present thesis the transition from laminar to turbulence is perceived to be a type of bypass transition, but the method of the disturbance is completely upside down. Instead of turbulence created in the freestream, the disturbance comes from the interaction of the boundary layer with the wall.

For the use of bypass transition as a method of flow control, work done in [26] shows that the maximum spatial energy scales linearly with the distance from the leading edge for Reynolds numbers larger than $100,000$. The empirical model developed in [26] can be used then as a design for flow control for turbulent boundary layers as the mode and intensity as the distance from the leading edge of the surface to the inception of turbulence in predictable. This work is important when considering the transition mechanisms of the present thesis.

II. OBJECTIVES

A. Costs and Benefits of DNS and IB

Direct numerical simulations offer a complete computation of the full range of length and time scales of turbulence active within the fluid of interest [6]. In DNS the Navier-Stokes equations are by definition solved directly at every point of the grid without the use of a turbulence model, and for this reason is the method of choice for learning about fundamental properties of turbulence [6]. The benefit of DNS for this setup is that since all scales of turbulence are resolved, the data that are obtained here are valuable in studying fundamental flow problems, and since the equations are solved directly the accuracy of the turbulence observed is dependent only the grid and the solver, but not on a turbulence model.

Historically the difficulty considering DNS is that of feasibility, and of the ability to compute the equations efficiently enough. DNS requires considerable computational resources to resolve even mildly complex flows, and this means that computations will take a considerable amount of time to complete a simulation. In order to resolve all the levels of turbulence for Reynolds number of 10^5 the computational power required is $O\left(Re^3\right) = 10^{15}$. In order to evaluate how well the simulation is characterizing the turbulence the grid spacing is evaluated in wall units. For the present thesis, the levels of turbulence that are able to be resolved are determined by the fluid grid used to perform the computations. Basing the gridding requirements off of work done by previous researchers the construction of the computational mesh used in this work is sufficient to resolve all applicable levels of turbulence without truncation of the information of the higher energy spectra that dominate the small scale turbulence. The difficulty of DNS is resolving the higher levels of turbulent energy well enough to resolve the flow without compromising the time required to perform the calculations. Considering a number of prior simulations the values of the grid spacing for streamwise, spanwise, and wall-normal dimensions are $O\left(15\right)$, $O\left(15\right)$, and $O\left(1\right)$, respectively [2],[7], [8], [9], and [10]. The grid spacing used in this thesis is compared to reference values to verify that the experiments resolving enough scales of turbulence and grid convergence study is run.

The method of IB handling employed for this thesis requires no special modification of the grid near the surface or the use of an overset grid method. of the surface, and the method has proven to be quite robust for turbulent flows [27]. This is of great advantage as the main concern when creating the surface geometry is only to ensure that the triangular mesh created to represent the geometry is robust. The disadvantage of this requirement is that additional simulations are required for the present study to validate solutions, which require additional resources. The greatest advantage of the IB technique is that changing the boundary surface is simple and requires minimal effort in terms of gridding. Gridding for the code used in the present thesis is straightforward, because the grid points in the streamwise and wall-normal directions are defined as 1D arrays to build a 3D structured mesh at run time. For example, increasing the number of points is done in the present work without changing the surface mesh with no changes in the solution due to the surface mesh.

B. Scope of Investigation

The purpose of this thesis is to further an understanding of the influence of dimple geometry on turbulent flows using a DNS with an immersed boundary method. The geometry investigated here is that of a flat plate with no dimples, two staggered rows of dimples and three staggered rows of dimples with the third row dimple in line of the flow with the first dimple.

The discussion of how the equations are solved and the immersed boundary method are in the next section followed by the computational set up, the results and discussion of the simulations, and finally the summary of the thesis work.

III. GOVERNING EQUATIONS

In computational fluid dynamics the equations that are solved in some for or another for any flow are the the Navier-Stokes (NS) equations. In many turbulent flows a model is used to account for scales of turbulence that are too small for the grid such as in large eddy simulations or are solved using a Reynolds averaged approach. The governing equations solved in this thesis are solved directly without a turbulence model and are given below in dimensional form and is signified by an overbar in Equations 1 and 2.

$$\frac{\partial}{\partial \bar{x}_i}(\bar{u}_i) = 0 \tag{1}$$

$$\frac{\partial}{\partial \bar{t}}(\bar{u}_i) + \frac{\partial}{\partial \bar{x}_j}(\bar{u}_i \bar{u}_j) = -\frac{1}{\rho}\frac{\partial \bar{P}}{\partial \bar{x}_i} + \nu \frac{\partial^2 \bar{u}_i}{\partial \bar{x}_j^2} + f_i \tag{2}$$

where u_i is the velocity, P is the pressure, ρ is the density, and f_i is a body force term that is used to handle the immersed boundary. For direct numerical simulations (DNS) these equations are solved without the use of a turbulence model as is done in this thesis. Equations 1 and 2 are solved in nondimensionalized form given by

$$\frac{\partial}{\partial x_i}(u_i) = 0 \tag{3}$$

$$\frac{\partial}{\partial t}(u_i) + \frac{\partial}{\partial x_j}(u_i u_j) = -\frac{\partial P}{\partial x_i} + \frac{1}{Re}\frac{\partial^2 u_i}{\partial x_j^2} \tag{4}$$

The Reynolds number, given in Equation 5, is defined in terms of the dimple depth, d, and the velocity is nondimensionalized such that the inlet freestream velocity, w_0 is unity. The kinematic viscosity, ν, is used in the code as the parameter to define the Reynolds number.

$$Re_d = \frac{w_0 d}{\nu} \tag{5}$$

It is common to define the flow near boundaries in wall units. For this a friction velocity is defined as shown in Equation 6. This characterizes the velocity near the wall in terms of the stress on the wall. For this thesis the density nondimensionalized by the inlet density.

The shear stress is given by Equation 7.

$$U_\tau \equiv \sqrt{\frac{\tau_w}{\rho}} \tag{6}$$

$$\tau_w = \mu \left. \frac{\partial w}{\partial x} \right|_{x=0} \tag{7}$$

The wall normal coordinate, x, is scaled by the friction velocity and the viscosity,

$$x^+ = \frac{w_\tau x}{\nu} \tag{8}$$

All other wall scaling in this thesis is performed in the same manner. In addition the present thesis presents the turbulent energy by using the root mean square (RMS) velocity. The RMS velocity is computed using Equation 9, and is used to evaluate the turbulent energy.

$$U_{i_{RMS}} = u_i^2 \tag{9}$$

For boundary layer statistics, Equations 10, 11 and 12 give the relationship of the momentum thickness, the momentum shape factor, and the displacement thickness, respectively, to the velocity. These equations are used in the integral momentum equation for laminar flow, but will provide for important statistics to analyze the boundary layer in the present thesis [28].

$$\theta = \int_0^\infty \frac{\bar{w}}{W_\infty} \left(1 - \frac{\bar{w}}{W_\infty} \right) dy \tag{10}$$

$$H = \frac{\delta^*}{\theta} \tag{11}$$

$$\delta^* = \int_0^\infty \left(1 - \frac{\bar{w}}{W_\infty} \right) dy \tag{12}$$

IV. DIMPLED SURFACE INVESTIGATION

A. Prior Investigations

The results in the present thesis are compared to DNS investigations of turbulent flow over a flat plate since the turbulence on the flat plate in the current simulation is similar to the solutions of turbulent flow over flat plates and the boundary layers of turbulent pipe flows. Understanding the flow physics of a simplified geometry is key to understanding the influence of the dimples on the flow. The main simulations in this thesis are of two configurations of the dimples on the flat plate, one of two rows of dimples and another of three dimple rows. The first of these investigations performed contains two rows of dimples, as shown in Figure 4. The array of dimples used here is similar to arrays used in [12, 13, 14, 15, 18]. The dimples in each row are staggered in the spanwise direction on the plate. The results of this experiment prompted further investigation into the interaction of additional dimples downstream; so an additional row of dimples was thus added downstream as seen in Figure 5. The third row of dimples that has been added behind the first two aligns with the first row in the span to keep the same staggered row principle. The results will show a cumulation of turbulent intensity not previously seen with only one or two rows of dimples.

This thesis compares flow statistics downstream of the dimples with work that is done for DNS of turbulence over flat plates from [2] and [8]. The turbulent structures of the most interest occur downstream as a direct result of the presence of the dimples, and include streamwise vortical structures that are shed at the streamwise edges and the center of the dimples [12]. The perturbation on the laminar boundary layer caused by the dimples as observed by [12] is different to the turbulent boundary layer transitions seen in [2] and [7]. This is a direct result of the large contributions of streamwise vortices that the dimple has inside of the boundary layer.

B. Coordinate system

For simplicity with the geometry the simulation is run with a Cartesian mesh. For the coordinate system used in this thesis, the streamwise direction is z, the wall-normal direction is x, and the spanwise component is y as seen in Figure 6. A picture of the geometry with an outline of the computational domain overlay is shown in Figure 7. The red box is the computational domain, and the gray surface is the 3 row configuration geometry. The surface used is larger than the computational domain, and extends upstream of the inlet. This can be seen as an example of the versatility of the IB technique. The original computational domain was much further upstream but to save wasted computations the inflow boundary was moved up to $0.5D$ from the leading edge of the first dimple row. The domain extends $5D$ downstream of the last dimple or at $z = 85$, and statistics are captured up to $z = 65$ to accommodate the nonphysical convective boundary at the exit. In the span, the domain extends from $y = -15$ to $y = 15$, and in the wall-normal dimension the domain begins at $x = 0.$ at the bottom of the dimples and extends to $x = 40$

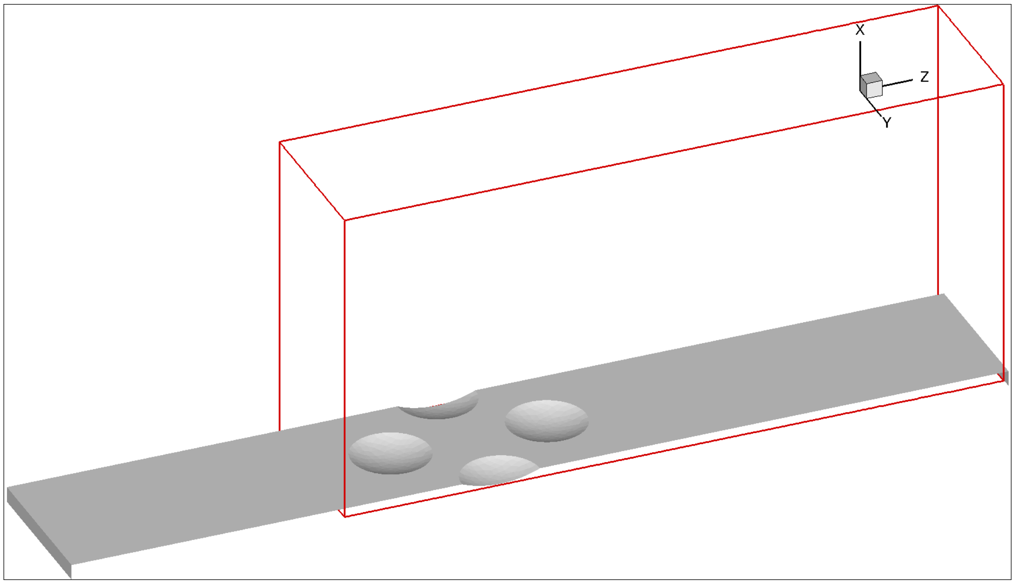

Figure 7. Surface geometry of the immersed boundary with computational domain outline.

C. Geometry

The geometry chosen for this thesis is designed to isolate the effect that the dimple has on flow characteristics from any confounding effects. Therefore, a flat plate with dimpled rows is chosen. This is similar to [12], [13], [14], [15] and [18] for research of heat transfer characteristics of dimpled surfaces for use in everything from ducts, tubing, and cooling systems as well as golf balls such as shown in Figure 1 where the dimples are arranged in a staggered configuration. Initial investigations were run without dimples and addition of dimples began with addition of two rows. The dimples are made with $d = 1$ and $D = 10$

as shown in Figure 3, and arranged in the configurations shown in Figure 4 and Figure 5 for two and 3 row configurations, respectively. For both of these configurations the spacing S_z and S_y in z and y, respectively, is 1.0.

This d/D ratio chosen such that the d/D ratio is similar enough to both golf balls (for golf ball the d/D ratio observed is 0.038153) as well as the heat transfer dimples of 0.2 for [18], [12] and [15] and 0.3 for [14] and [13]. The spacing chosen is such that the spacing between the dimple edges at the flat plate surface is $0.4142D$, which is similar to the spacing on a golf ball of $0.463D$ The width of the geometry spans the computational domain, which is designed to split through the center of each dimple in the second row for a span of 30, such that there is one total dimple in each row. Since the condition in the spanwise direction is periodic the flow will actually “see” an infinite row of dimples. This will be discussed later in detail.

D. Grid Creation and Refinement

The grids used in this analysis are created for DNS. Initial investigations were computed for the present thesis to identify how the dimples are influencing the flow field, and understanding of how the grid must be refined in what areas to evaluate all levels of turbulence. The number of points and the grid spacing in wall units is tabulated in Table 2. The spacing in the grids as they are refined are chosen to give the fastest computation time to understand the basics of the flow and effects of the setup on the flow. The initial work to define boundary conditions and initial conditions was performed on the first two grids. The final computational work was done on the third grid where the spacing was chosen to resolve enough scales of turbulence to not introduce errors. This method of evaluating the boundary layer is consistent with work done in [24] where they used a refined zone to determine if the grid they were using was “good enough” for the resolution of turbulence for DNS quality results.

In order to make the grid fine enough to resolve all of the turbulence scales the simulations run were compared to that of literature. The grid is compared by assessing the grid spacing in wall units. The grid was refined in such a way that the spacing near the wall for Δx^+, Δy^+, and Δz^+ are about 1, 15, and 15, respectively, at a z location of 60, which is in the wake in the fully turbulent downstream region. This ensures that the scales of turbulence are resolved by the mesh [2]. This baseline for grid spacing is taken from a variety of sources tabulated in Table 1.

Table 1. Literature values for grid spacing for DNS.

Grid	[9]	[8]	[2]	[10]	[7]
Min Δx^+	N/A	0.05	N/A	0.3	<1
Max Δy^+	5-10	7	11.13	15	6.7
Max Δz^+	8-16	12	5.91	10	20

Table 2. Grid refinement with wall unit values for 3 dimple row simulations used for grid refinement.

Grid	1	2	3
NX	231	324	355
NY	130	130	322
NZ	486	486	834
Min Δx^+	6.71	1.26	0.80
Max Δy^+	55.73	33.00	12.42
Max Δz^+	27.78	31.53	16.56

E. Boundary Conditions

In order to isolate the influence of the dimpled geometry on the flow, little influence from the boundary conditions is imposed on the flow regime. The inlet and top surface velocity condition is a Blasius profile scaled such that the inlet boundary layer thickness is equal to the dimple depth, d by using a virtual origin at some location upstream of the inlet. This technique is used in a similar manner as in [2]. The streamwise velocity is given in non-dimensional form in Equation 13. The non-dimensional wall-normal velocity is calculated by using the non-dimensional stream function, f, relationship between the streamwise velocity given by Equation 14. This relationship and the stream function, ψ, are used to solve for the wall normal velocity component on the top surface given in Equation 15.

$$u = \frac{\partial f}{\partial \eta} = f'(\eta) \tag{13}$$

$$f(\eta) \equiv \frac{\psi}{\sqrt{\eta z w_0}} \tag{14}$$

$$u \equiv -\frac{\partial f}{\partial z} = \frac{w}{\sqrt{\frac{\nu w_0}{z}}} = \frac{1}{2}\left(\eta f' - f\right) \tag{15}$$

Equations 13–15 are substituted into the momentum equation to obtain the Blasius form given by

$$f''' + \frac{1}{2} f'' = 0 \tag{16}$$

This equation is solved with the boundary conditions in Equation 17–20.

$$w(z, x = 0) = 0 \rightarrow f'(\eta = 0) = 0 \tag{17}$$

$$u(z, x = 0) = 0 \rightarrow f(\eta = 0) = 0 \tag{18}$$

$$w(z, x \rightarrow \infty) = w_\infty \rightarrow f'(\eta \rightarrow \infty) = 1 \tag{19}$$

$$w(z = 0, x) = w_\infty \rightarrow f'(\eta \rightarrow \infty) = 1 \tag{20}$$

Equations 19 and 20 collapse in this form however so a fourth condition is required to achieve the required number of conditions of degrees of freedom in Equation 16. The fourth condition is achieved by using $f''(0) = 0.33206$ [29]. The solution of the Blasius equation is scaled as mentioned above, and the entry length is then related to the velocity, δ_{99}, and the viscosity by η, defined in Equation 21. η is a similarity variable used to make the scaling of the Blasius boundary layer simpler.

$$\eta = 5.0 = \delta \sqrt{\frac{w_\infty}{\nu z_0}} \tag{21}$$

where η is a scale factor used for the Blasius solution, w_∞ is the freestream velocity, ν is the kinematic viscosity and z_0 is the distance of the virtual origin to the inlet [28]. This equation along with Equation 22 are solved simultaneously to determine z_o and ν. Both of these parameters are given as inputs to the solver for scaling the Blasius solution as the inlet velocity field.

$$Re_{z_0} = \frac{w_0 z_0}{\nu} \tag{22}$$

This condition on the top surface eliminates acceleration in the boundary layer instead of having a slip wall on the top surface causing acceleration in the boundary layer as shown in Figure 8.

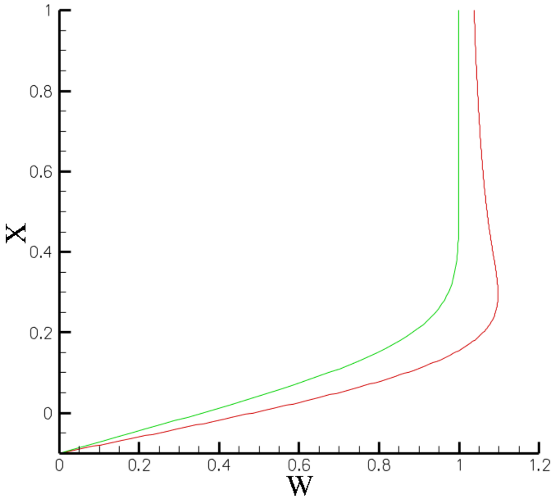

Figure 8. Acceleration in the boundary layer. Green line is inlet profile and red line is downstream at $z = 3$.

To enforce continuity across the domain as a control volume the outlet condition is a convective condition. The convective condition assumes a constant velocity profile at the exit and is scaled using the inlet as well as the fluid that crosses the top surface due to the Blasius condition on the top surface. This ensures that continuity is enforced across the domain. The convective condition is computed in a three step process, first Equation 23 is used to calculate the volumetric flow rate, Q, at the inlet and outlet, then a scale factor, C is computed, shown in Equation 24. Lastly the new outlet velocity profile is calculated using C as shown in Equation 25.

$$Q = w\dot{c}A \tag{23}$$

where A is the area, and w is the streamwise velocity, and c is a constant to scale the outlet velocity based off of the flow out of the domain.

$$C = \frac{Q_{in}}{Q_{out}} \tag{24}$$

$$w_{new} = w_{old} \times C \tag{25}$$

The condition on the bottom is the immersed boundary. The geometry spans both the spanwise and streamwise directions so that the surface boundary condition is the bottom surface. All points underneath the boundary are marked as zero velocity, and separated from the computational domain of interest.

In the spanwise direction the flow is assumed periodic. The periodic condition is common among flat plate solutions [9], and eliminates any effect that having a wall or other condition has on the flow. The periodic condition is not necessarily physical [2], but in general will reflect a flat plate that is infinite in the spanwise direction.

F. Flow Parameters

In order to isolate the influence of geometry on the turbulent flow, the parameters defining the flow are held constant throughout the work in this thesis. The input to the code uses $1/Re_d$, δ_{99}, and z_0, which for this thesis are 2.5×10^{-5}, 1.0, and 160.0 respectively. To determine the inlet conditions Re_{z_0} is chosen to be about 600,000, which is a value that is sufficiently high enough to sustain turbulence over the flat plate, but is much lower than the critical Re_z. After ν is determined to satisfy the inlet scales δ at the inlet and z_0, Re_d is computed by Equation 5 with the non-dimensional values of d and w_0, which both are used as the scales so they are 1. The computed value of Re_d is thus 4000.

V. METHODOLOGY

A. Flow Solver

The simulations are computed using the code described by [27, 30, 31], an immersed boundary, parallel, structured, direct numerical solver. This code solves the Navier-Stokes equations with a fractional step method over a staggered grid with a third order Runge-Kutta (RK3) time advancement [31]. The staggered grid is created such that the pressure is calculated at the cell center and the three velocity components are solved on the cell faces. To illustrate this the picture in Figure 6 shows the staggered grid with face-centered velocity components and the volume-centered pressure. The coordinate system is atypical of many fluids solutions with the streamwise component as z, the wall-normal component is x and the spanwise component is y.

The first step in the fractional step method is the predictor step, and is called such because the velocity field is not divergence free [30]. This step is given by,

$$\frac{\hat{u}_i^k - u_i^{k-1}}{\Delta t} = \gamma_k H\left(u_i^{k-1}\right) + \rho_k H\left(u_i^{k-2}\right) - \alpha_k \frac{\partial p^{k-1}}{\partial x_i} + f_i^k \tag{26}$$

where $\hat{u}_i$ is the intermediate nonphysical velocity vector, H is a spatial operator that contains the viscous and convective terms, and the script, k, denotes the step level of the fractional step method. The intermediate non-solenoidal velocity field is missing the pressure influence, which is accounted for in the correction step. The correction step consists of solving the Laplacian of Φ, the projection operator with the gradient of the intermediate velocity field, given in Equation 27. This operator is not exactly physical pressure, but is such for flows where mass flow is conserved [27, 8].

$$\frac{\partial^2 \Phi^k}{\partial x_i^2} = \frac{1}{\alpha_k \Delta t} \frac{\partial \hat{u}_i^k}{\partial x_i} \tag{27}$$

The last step is to project the Φ field onto the solenoidal grid given in Equation 28. The superscript denotes the fractional step and is used here to identify the advancement level. This step enforces continuity across the entire domain. The pressure field is corrected with the new value of Φ as in Equation 29. The projection in Equation 27 is approximated by a series of two dimensional problems using trigonometric expansions which are solved directly [31]. The disadvantage of this is that one dimension of the computational domain must be uniformly spaced [31].

$$u_i^k = \hat{u}_i - \alpha_k \Delta t \nabla \Phi^{n+1} \tag{28}$$

$$p^k = p^{k+1} + \Phi^k \tag{29}$$

For equations 26–28 the RK3 coefficients used are: $\alpha_1 = 8/15$, $\gamma_1 = 8/15$, $\rho_1 = 0$, $\alpha_2 = 2/15$, $\gamma_2 = 5/12$, $\rho_2 = -17/60$, $\alpha_3 = 1/3$, $\gamma_3 = 3/4$, and $\rho_3 = -5/12$.

B. Immersed Boundary Technique

In an immersed boundary method, the geometry of interest is interpreted by the flow solver in such a way as to reflect the geometry of the object into the Eulerian fluid grid. The advantages of this method are that the solver is efficient because the grid is a simple structured grid, and allows for complex geometries to be used with a simple grid. The immersed method with this solver has proven to be both efficient and second order accurate with the use of fairly complex geometries including flow over a cylinder, and flow through a wavy channel [27]. The wavy channel in [27] consists of a channel in which one side is a sinusoidal wall. The dimpled wall of interest in the present thesis is similar to the wavy channel geometry.

For the present thesis, the surface geometry is defined by a triangular mesh created in Pointwise. The surface mesh is interpreted by the solver as a no-slip boundary by imposing the boundary conditions on the fluid grid at neighboring points to the mesh. The imposition of the body in the domain is accounted for as the body force term, f, in Equation 26. The forcing is handled in a three step process, which is the same as in [31] and [20]. In the first step to the code handling the surface mesh is to locate the object within the fluid grid. This is done by marking points that lie within the boundary as solid points, the points that are outside the surface are marked as fluid points and the forcing points.

The forcing points are grid points in the fluid mesh that have at least one neighboring point within the solid region [20]. The velocity on the forcing points is altered by interpolation of the velocity from the neighboring points within the fluid region and the location of the boundary where the velocity is zero.This is illustrated in Figure 9 where the fluid points are marked as blue dots, the solid points are marked as black squares, and the forcing points are red triangles. Identification of these three types of points is shown on a fluid domain with an arbitrary boundary immersed shown in Figure 9.

The mechanism to identify the points is straightforward. Rays are shot normal to the boundary surface through the forcing point to identify the neighboring fluid grid points, which are then used to create an interpolation stencil. The interpolation of the velocity is computed from the neighboring fluid points to the intersection of the stencil with the fluid grid. Ultimately the velocity at the forcing points is altered such that the velocity respects the no slip condition at the surface geometry and the velocity in the fluid region. In Figure 9 the intersection of the ray with the fluid grid is marked with a red x. The velocity at that intersection is used to determine the velocity of the forcing point. The lines shown in Figure 9 are rays that are used to make the interpolation stencil with the surrounding points to reconstruct the velocity.

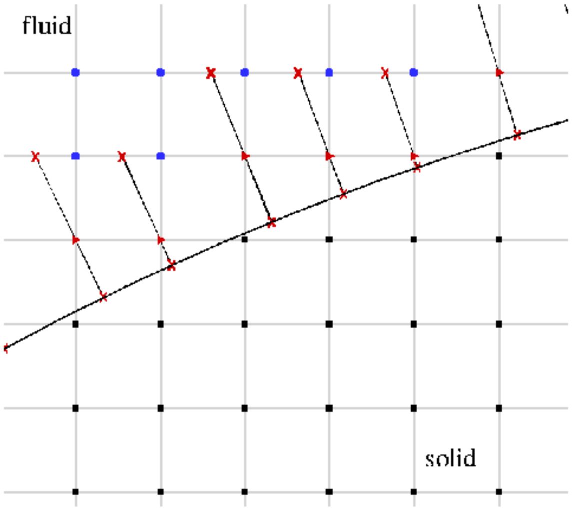

Figure 9. Grid points as marked by the normal lines. Blue dots are fluid points, black dots are the solid, red triangles are forcing points, and crosses are the intersection points.

The no-slip boundary condition is then enforced onto the fluid grid by reconstructing the velocity at the forcing points such that the velocity at the wall is zero. The force, f, of the solid on the fluid phase is computed by altering the velocity at the forcing points. The body force is calculated from the solution to Equation 30.

$$f_i^k = \frac{\hat{U}_i^k - u_i^{k-1}}{\Delta t} - \gamma_k H\left(u_i^{k-1}\right) + \rho_k H\left(u_i^{k-2}\right) - \alpha_k \frac{\partial p^{k-1}}{\partial x_i} \tag{30}$$

where $\hat{U}_i^k$ is the reconstructed velocity that satisfies the no-slip condition at the immersed boundary. Further detail can be found in [27, 30, 31].

C. Flow Parameters

For this solver the velocity profile at the inlet is a Blasius laminar profile scaled by providing the virtual origin of the boundary layer, z_0 and height of the boundary layer at the inlet, δ_i. To understand characteristic results the reference length is chosen as d, the dimple depth. All length variables are non-dimensionalized by d. The value input for δ_i is 1, which is of course non-dimensionalized to be the same as the dimple depth. This ensures that the boundary layer height is on the same order as the dimples so that the interaction of the boundary with the dimple is clear in the results. The Reynolds number, Re_d, then reduces to the inverse of the kinematic viscosity, because the length and time scales reduce to 1.

In order to determine z_0 and ν, equations 31 and 32 are solved simultaneously, but since there are four unknowns and only two equations, two parameters, Re_z and δ_i are chosen to give the desired flow conditions. Firstly, $Re_z = 640,000$ was chosen to provide a sufficiently high Reynolds number, but still is an order of magnitude lower than the critical Re_z (3×10^6). The boundary layer height, δ_i at the inlet is chosen as the same height as the dimple. Since, the d is the reference length, the δ_i is also 1. Equations 31 and 32 are then solved simultaneously for ν and z_0, which yields $\nu = 2.5 \times 10^{-4}$ and $z_0 = 160.0$. The Reynolds number in terms of the dimple depth used is $4,000$, ans is equivalent to a Reynolds number of 42,000 for a golf ball. This would be roughly the Reynolds number for a well struck ball.

The following equations are used to determine the conditions on the flow at the inlet,

$$Re_z = \frac{w_\infty z_0}{\nu} \tag{31}$$

$$\eta = \delta_i \sqrt{\frac{w_\infty}{\nu z_0}} \tag{32}$$

where w_∞ is the streamwise velocity at the inlet, η is a parameter to scale the boundary layer from the Blasius solution and is 4.95 [28], and Re_z is the local Reynolds number relative to a virtual origin upstream of the inlet.

VI. RESULTS AND DISCUSSION

A. Preliminary Investigation

The first simulation run for the present thesis was designed to show that the flow remains laminar over a flat plate throughout the domain, and the solver will produce the expected result. The expected result is for the flow to remain laminar and for the boundary layer to grow as expected with a selfsimilar boundary layer. These results show that the simulation behaves as expected. The flat plate simulation without dimples was run for a Reynolds number in the laminar regime to get an understanding of how an undisturbed boundary layer exists in the set up used for the present thesis. The setup of the inlet parameters for the first simulation is also the same for all subsequent simulations. As discussed previously, the boundary layer height at the inlet, δ_i, of 1.0 is prescribed along with $Re_z = 640,000$ to solve equations 31 and 32 simultaneously for z_0 and ν, which are inputs into the solver to define the flow characteristics desired for the present thesis. Since the freestream velocity and reference length are assumed to be 1 by the solver, the viscosity, ν, is the inverse of the Reynolds number, Re_d input into the solver. As stated before the inputs are $\nu = 2.5e - 4$ and $z_0 = 160.0$, which corresponds to $Re_d = 4000$.

This study is used to show that the Blasius profile as an inlet will produce a velocity field of self similar velocity profiles as would be expected by a laminar boundary layer [28]. The plot of color contours in Figure 10 for streamwise velocity shows the flow does not transition to turbulence. The boundary condition imposed on the top of the domain defines the velocity in the wall normal direction as the Blasius condition in order to avoid issues with the flow accelerating in the boundary layer. Since the velocity computed for the wall normal dimension comes from the Blasius solution the pressure gradient on the surface on the plate is assumed to be zero. The inlet condition is prescribed by a Dirichlet boundary condition of the velocity such that the profile from the surface of the plate to the edge of the boundary layer is a Blasius laminar profile. The location of the top surface was chosen for this simulation such that is is at least 20 units above the plate, and was chosen as $4D$ for the dimpled plate such that the top surface is far enough from the plate to ensure independence from the boundary condition. The grid used for this invesitgation was the second grid described in Table 2. The grid was chosen to compare against results with the dimpled geometry. Since the flow here does not transition, the laminar flow can be solved with a coarser grid than for the turbulent simulations.

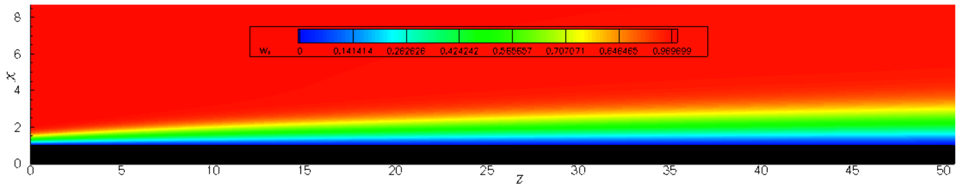

Figure 10. Streamwise velocity contours. Plate surface is at x = 1.

Velocity profiles taken at various points along the length of the flat plate confirm that the flow regime remains laminar, and the boundary layer grows as would be expected for solution to the Blasius equation. This can be seen in Figure 11 as the profiles are scaled using a Blasius scaling such that the velocity profile are self similar. The black line is the inlet condition and the red are the scaled velocity profiles. By scaling the boundary layers down the length of the flat plate the profiles collapse. To verify that the code is indeed solving the Blasius boundary layer profile for this simulation an error evaluation was performed by Jeff Mode in his thesis work [1]. The error of the code observed in his work, which is the code used in the present thesis, was on $O(2)$. In addition to the error, the convergence of the code was tested by E. Balaras in [27], and the same solver is used for the simulations by C. Smith et. al. in [20] for the simulations over a golf ball.

B. Simulation of Two Dimple Rows

In the present thesis the dimples are arranged in staggered rows. the first investigation of dimples in the present thesis has two rows of dimples. In order to save on computational cost the total span of the domain is 20 units. the first dimples is placed at the center of the span. This means that the second row contains a half dimple on either side of the span of the domain. This arrangement is commonly seen where dimpling is used to control flow. Most likely this is done for a couple of reasons the first being that more dimples are able to fit on the surface and that the flow will then be more uniform in the span down the surface. For the

---

[1] Mode, J. 'Simulation of the Flow over a Flat Dimpled Plate'. Master's Thesis. Arizona State University. December 2010

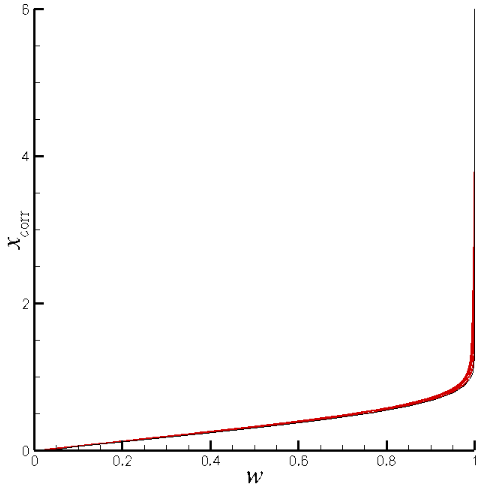

Figure 11. Streamwise velocity profiles. Blasius scaling employed on the wall normal dimension. Plate surface is at x = 1.

present thesis, having only two rows the effect of having one dimple downstream of another but offset will give insight into any possible interactions between the dimples, the flow, and the arrangement of the dimples on the surface of interest. This simple arrangement will give results that will show interactions between the dimple rows as well as fundamentally how the transition mechanisms work when using dimples to control flows.

The schematic in Figure 3 shows dimple depth, d, and dimple diameter, D, as well as how the dimple is part of the wall geometry. The ratio used for the present thesis is $d/D = 0.1$. The arrangement of the dimples is shown in in Figure 4. The spacing in the streamwise and spanwise dimensions is $S_z = 1.0$ and $S_y = 1.0$, respectively. The second row of dimples contains half of a dimple on either side of the plate, and the periodic condition is enforced through the center of the second dimple in the span.

The Re_τ observed at $z = 60$ in the wake of the first dimple is 364, and Re_θ is 926, and Re_τ is 290, and Re_θ is 789 in the wake of the second dimple. Identifying this, it is obvious that the turbulence seen in the wakes of the two dimples is completely different, and between the dimples at $y = 5$, $Re_\tau = 157$ and $Re_\theta = 707$. The Re_τ and Re_θ from [1] are 180 and 287, respectively. Re_θ from [2] is 900. The scaling is indicative of turbulent flow in the wake, and shows that compared to [1] the effective influence of the turbulence on the free stream is on the same order as in the wake of the first dimple.

The streamwise velocity near the wall downstream of the dimples correlates to data from [1] and [2]. At a z location of 60 the plot in Figure 12 shows the streamwise velocity in wall units. The data from [1] ($\Box$) is for a channel flow and the data from [2] (Δ) are for a zero pressure gradient flat plate Near the wall in the viscous sublayer the solutions all collapse on $w^+ = x^+$ in the viscous sublayer up to $x^+ = 30$. The red line shown on the w^+ vs. x^+ plot in Figure 12 is the piecewise function give in Equation 33, and is a reference line of the linear model in the viscous sublayer and the log-law of the wall in the intermediate region. The intermediate or fully turbulent region begins at $x^+ = 30$ and extends to the outer regions. The velocity on the plate begins to deviate from the references in this region. In Figure 12 the velocity deviates greatly in this region due to the flow not being homogeneous in the span.

$$w^+ = \begin{cases} x^+ & x^+ < 10 \\ \frac{1}{0.41}\ln\left(x^+\right) + 5.2 & x^+ > 30 \end{cases} \tag{33}$$

The difference in the intermediate region is indicative of the variation in the span. The velocity profile in Figure 12 is somewhat misleading. The standard approach of ensemble averaging the velocity in the span doe not actually hold true for this simulation due to the nonhomogenous nature of the plate. Though Figure 12 gives a general idea as to the boundary layer properties, an expanded approach of looking at different locations in the span is necessary to understand how the flow varies and the level of variation. The velocity scaled by wall units is replotted for the center of the span, between the dimple rows, and at the edge of the span in Figures 13, 15, and 14, respectively. This is done to view the velocity downstream of each of the dimples, and to see the difference where the flow is less likely to have transitioned i.e. where there is not a dimple perturbing the flow upstream of the location in the span.

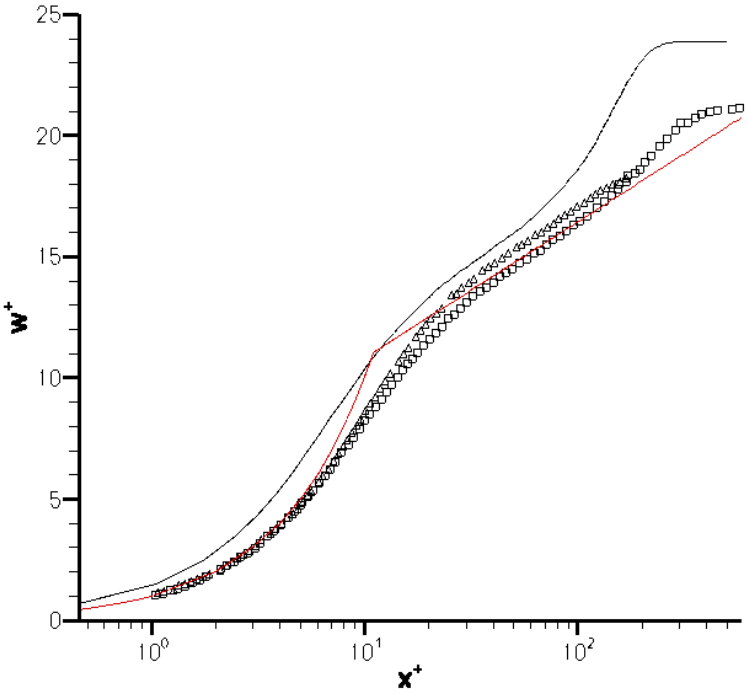

Figure 12. Span averaged mean velocity, w^+ vs. x^+ for two-dimple rows at $z = 60$. $\square$, [1]; $\triangle$, [2].

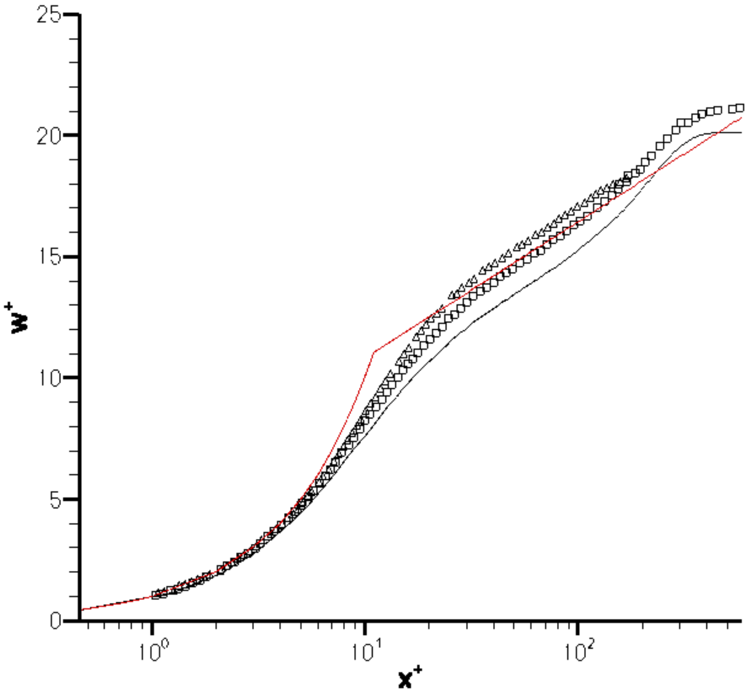

Figure 13. Mean velocity, w^+ vs. x^+ at $y = 0$ for two-dimple rows at $z = 60$. $\square$, [1]; $\triangle$, [2].

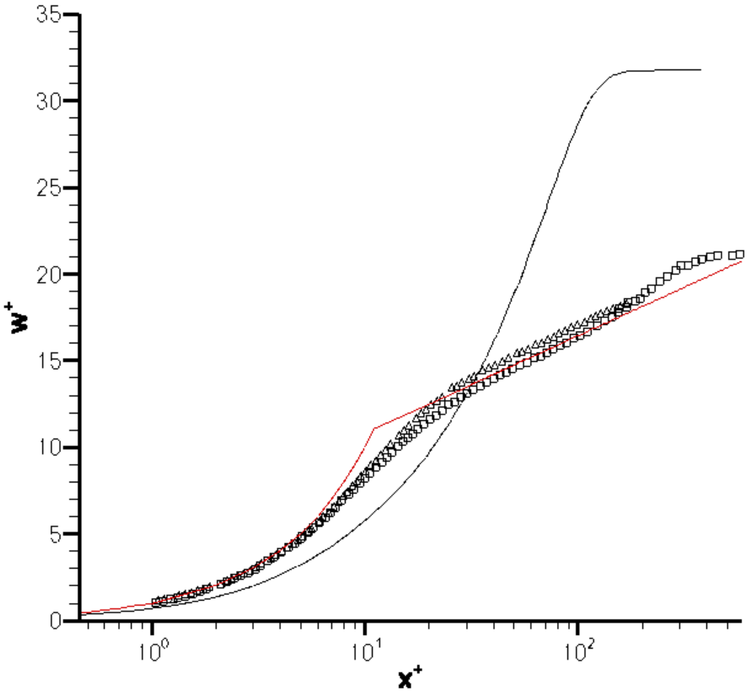

Figure 14. Mean velocity, w^+ vs. x^+ at $y = 5$ for two-dimple rows at $z = 60$. $\square$, [1]; $\triangle$, [2].

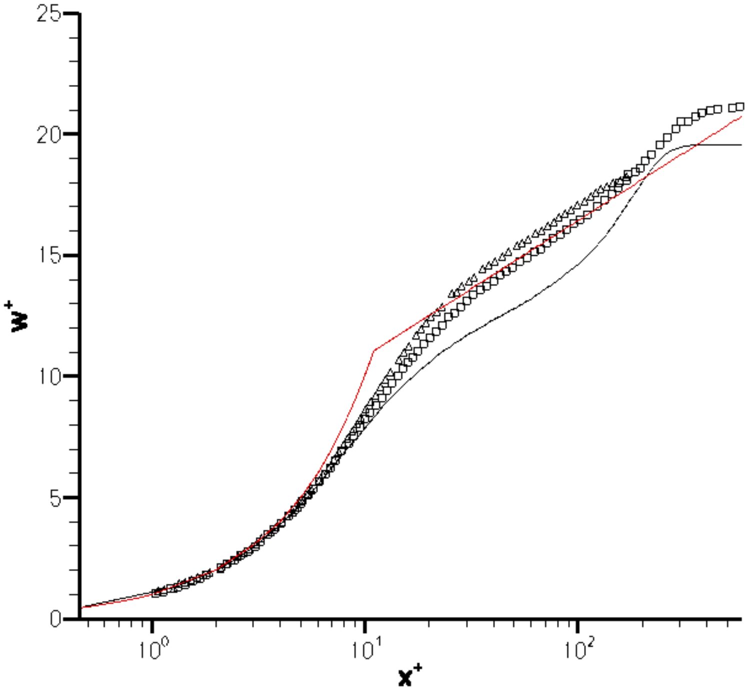

Figure 15. Mean velocity, w^+ vs. x^+ at $y = 10$ for two dimple rows at $z = 60$. $\square$, [1]; $\triangle$, [2].

RMS velocity in the wake region shows characteristics very similar to those observed by [7] and [2]. The plots in Figure 16 show the RMS velocities at a z location of 60, which is $4.5D$ downstream of the trailing edge of the first dimple with values plots from [1] and [2]. In the viscous sublayer the agreement is quite good, but looking in the intermediate and wake region the RMS sustains higher magnitude than either cavity or nominal zero pressure gradient flat plate flows. It seems that influence from the dimples forces more energy to become turbulent kinetic energy. The turbulence observed due to the influence from the dimples agrees well with other experiments in the viscous sublayer, but deviates in the fully turbulent intermediate layer and the wake region of the turbulent boundary layer. This departure from the reference flows is an effect of the dimple imposing more turbulent mixing than is seen in naturally transitioning. The RMS velocity between the dimples also shows an interesting phenomenon. The w_{RMS} component shows a much larger peak of around 4 whereas compared to the literature or even the results inside of the wakes behind the first and second dimples shows a peak of around 2.8.

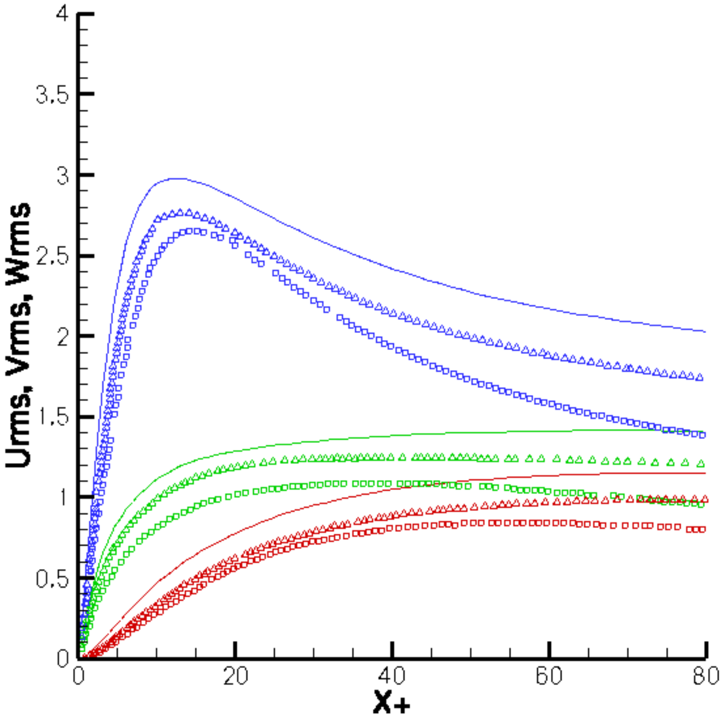

Figure 16. Span averaged components of RMS velocity vs. x^+. □, [2]; △,[1].

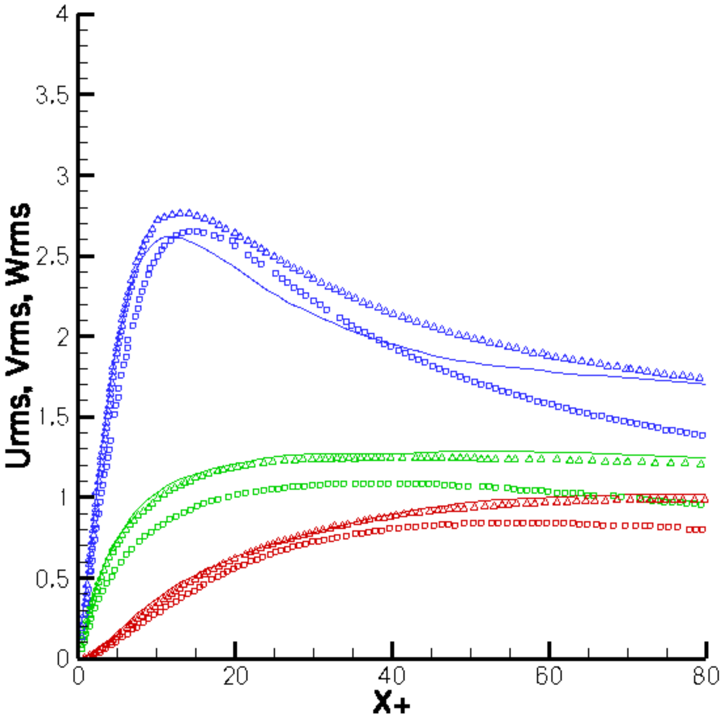

Figure 17. Components of RMS velocity vs. RMS velocity at $y = 0$ vs. x^+. □, [2]; △,[1].

Further investigation shown in Figure 20 of the streamwise RMS velocity over the domain shows that much of the turbulent energy occurs off the trailing edge of the dimples. After the dimples in the wake region where the turbulence caused by the dimples converges the RMS looks much like that of a zero pressure gradient flat plate. The wake is concentrated behind the dimples, and the flow does not transition until further downstream between the dimples.

Between the dimples the flow is less turbulent until about $2D$ downstream of the second dimple. Since this region does not have the perturbation of any part of the dimple depth, i.e. there is no turbulent production directly upstream. In contrast with many experiments the tripping of the boundary layer here does not span the entire spanwise dimension so the the flow must mix in spanwise dimension until about $z/D = 2$ downstream of the dimples. Even at $z/D = 4.5$, the last contour plane shown, the flow does not fully transition across the span. There are still two distinct wakes that exist in the RMS plot. The contour planes

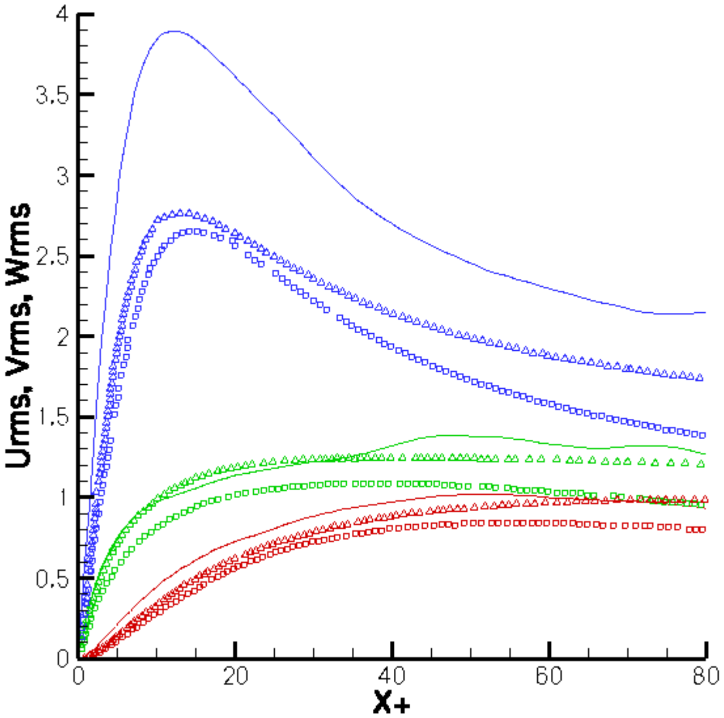

Figure 18. Components of RMS velocity at $y = 5$ vs. x^+. □, [2]; △,[1].

far downstream of the wake also confirm the behavior shown in Figure 18. The contours shown that the higher energy flow is much further in the boundary layer at a y location of 5 than behind the dimples at y locations of 0 and 10. During the transition where the wakes converge there is a very higher energy region near the wall that causes the wake to expand into the laminar regions. The transition in the regions outside of the wake occur as the higher energy flow is entrained by the turbulent eddies next to the wall so that high velocity flow is near the wall where the low velocity region of the laminar flow is. This creates a situation where the higher velocity and lower velocity flow interact causing the laminar flow to be disturbed by the turbulent wakes and thus the transition to turbulence.

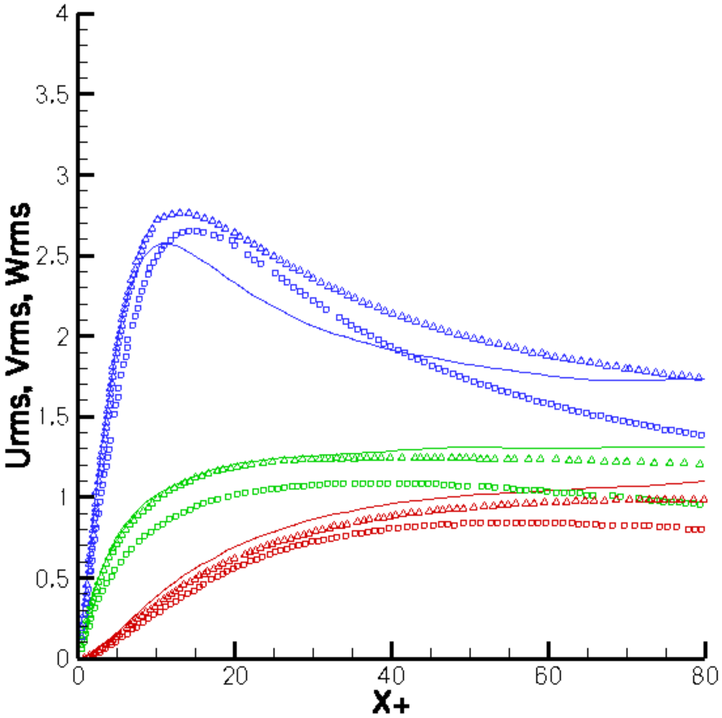

Figure 19. Components of RMS velocity at $y = 10$ vs. x^+. □, [2]; △,[1].

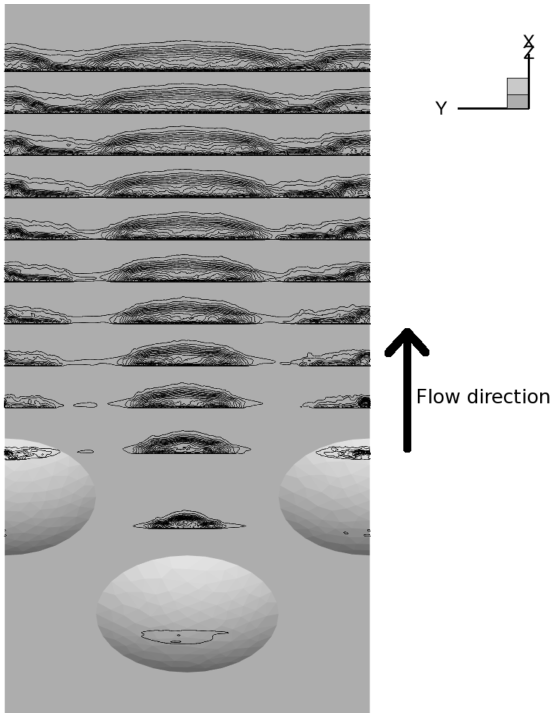

Figure 20. Line contours of RMS velocity in x-y planes along the streamwise direction.

Boundary layer growth is significantly effected by the presence of the dimples. As shown in Figure 21 the displacement thickness, δ^* decreases dramatically downstream of the first dimple row as the flow becomes turbulent as would be expected. As well the momentum thickness, θ increases at a faster rate than the Blasius solution. In Figure 21 the δ^* is the green line, θ, is the blue line, and $H = \delta^*/\theta$ is the red line, the Blasius solution for δ^* and θ are the dashed and dash-dotted lines, respectively. This occurs at a Re_z much further upstream than a natural transition would occur due to the influence of the dimples on the boundary layer.

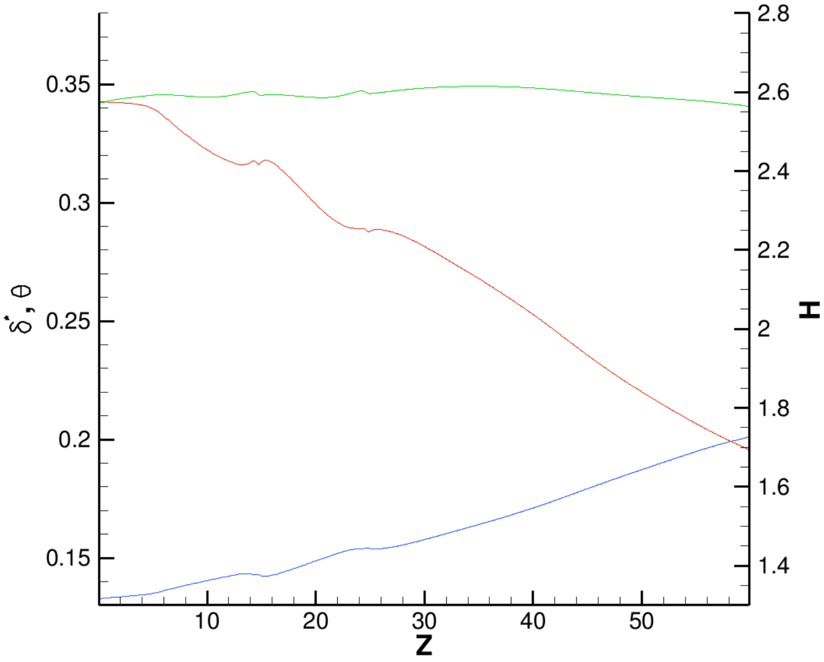

Figure 21. Boundary layer characteristics; green line is δ^*; blue line is θ; red line is H.

Figure 21 compared to either Figure 22, 23 or 24 actually shows how nonhomogeneous the flow is in the span. The boundary layer growth with averaging across the span does not seem to make much sense, and that is due to the nature of the transition over the plate. Since the transition in the first wake is due to the first dimple, this happens further upstream than other locations, the transition due to the second dimple happens $z/D = 1$ downstream of the first, and finally the transition between the rows happens at a much slower rate than either of the wakes. The plots in Figures 22 and 24 show what is happening to the boundary

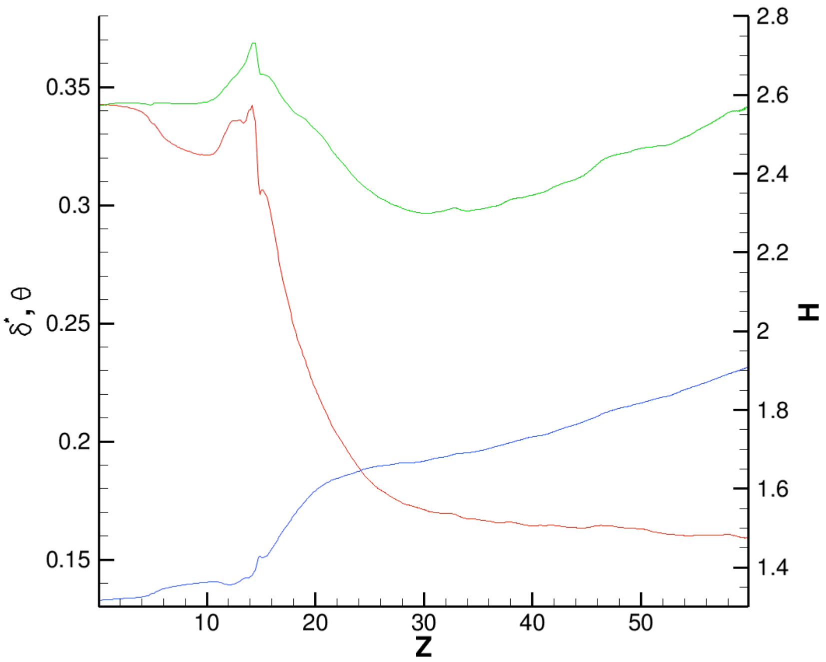

Figure 22. Boundary layer characteristics along the length of the domain at the center of the span; green line is δ^*; blue line is θ; red line is H.

layer thickness over the length of the transition. For example, in Figure 22 the displacement thickness, δ^*, remains constant along the length of the dimple, but then increases sharply after the dimple as the velocity at the edge of the dimple is turned away from the wall and the boundary layer is stretched. After this blip in the thickness, the displacement thickness begins to decrease as the flow transitions. As for the momentum thickness shown in Figure 22, there is an increase where the flow is transitioning, then stabilizes in a constant slope at the same time that the displacement thickness stabilizes. The ratio of these two statistics, the momentum shape factor, H, shows that at about $z = 30$ the flow has almost fully transitioned to turbulence. The momentum shape factor will not, however, be constant since the shape factor in a turbulent flow depends on the skin friction, which is not constant. This same behavior also occurs at the edge of the domain through the center of the second dimple as seen in Figure 24.

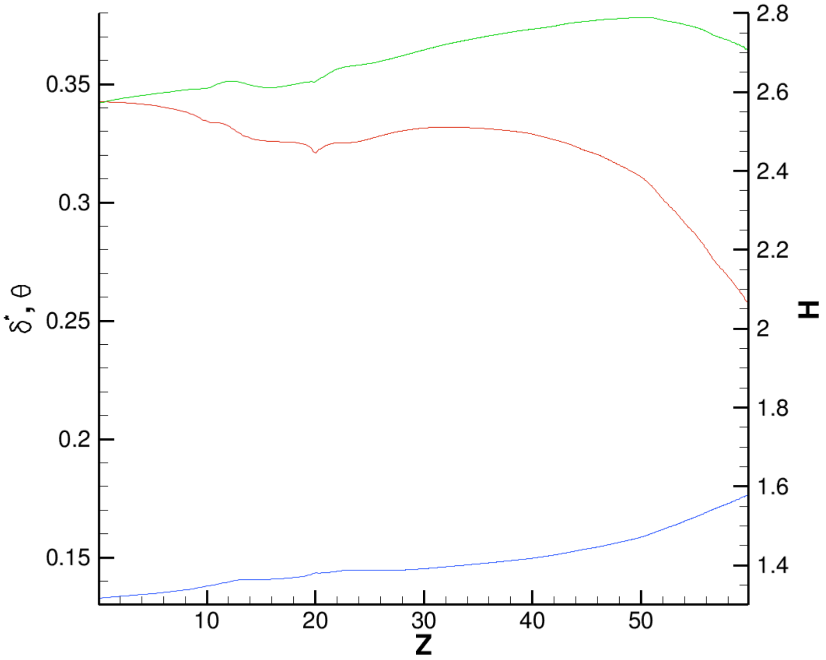

Figure 23. Boundary layer characteristics along the length of the domain between the dimple rows in the span; green line is δ^*; blue line is θ; red line is H.

The plot of the boundary layer statistics between the dimples in Figure 23 shows the transition of the boundary layer has not fully occurred within the domain. The same transistion behavior as seen over the dimples is seen between if not over a much longer distance. The disturbance of the boundary layer is happening at a much slower rate because the transition mechanism between the dimples is much different than in the wake since the disturbance comes from the wake of the dimples. The displacement thickness increases while the flow is in transition. The momentum thickness also increases, and the shape factor begins the decrease to be closer to a turbulent flow.

The boundary layer thickness in terms of 99% of the free stream velocity, $\delta_{99\%}$, is shown in Figure 25 on top of contours of streamwise velocity for three slices in y. The $\delta_{99\%}$ line shows again what was seen in the previous plot regarding the transition of the flow to turbulence. The boundary layer increases as the flow becomes turbulent, and in the wake behind the first dimes the boundary layer is much larger than either of the other two planes. The color contours in Figure 25 show that the boundary layer has much higher velocity

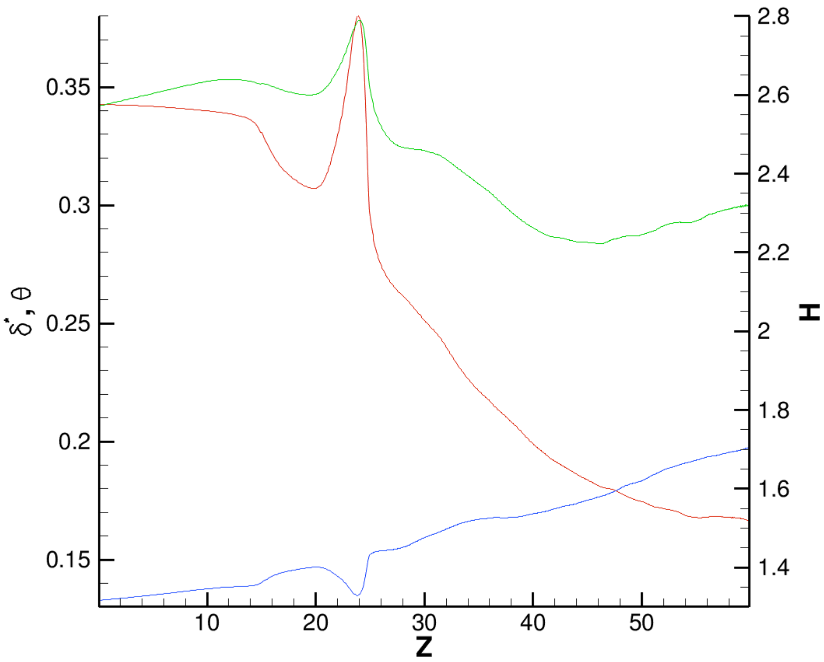

Figure 24. Boundary layer characteristics along the length of the domain at the edge of the span; green line is δ^*; blue line is θ; red line is H.

fluid than the laminar regime.The plane between the dimples shows that the flow has not transitioned, but is transitioning toward the end of the domain.

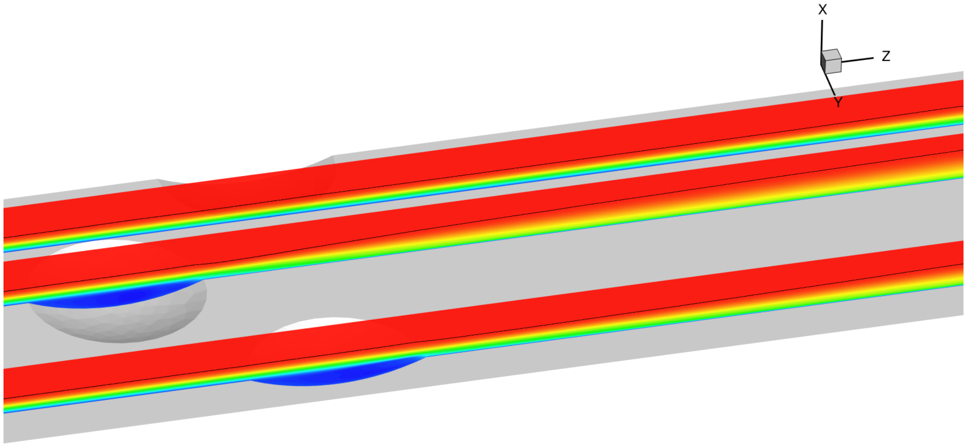

Figure 25. Streamwise velocity contours with $\delta_{99\%}$ line.

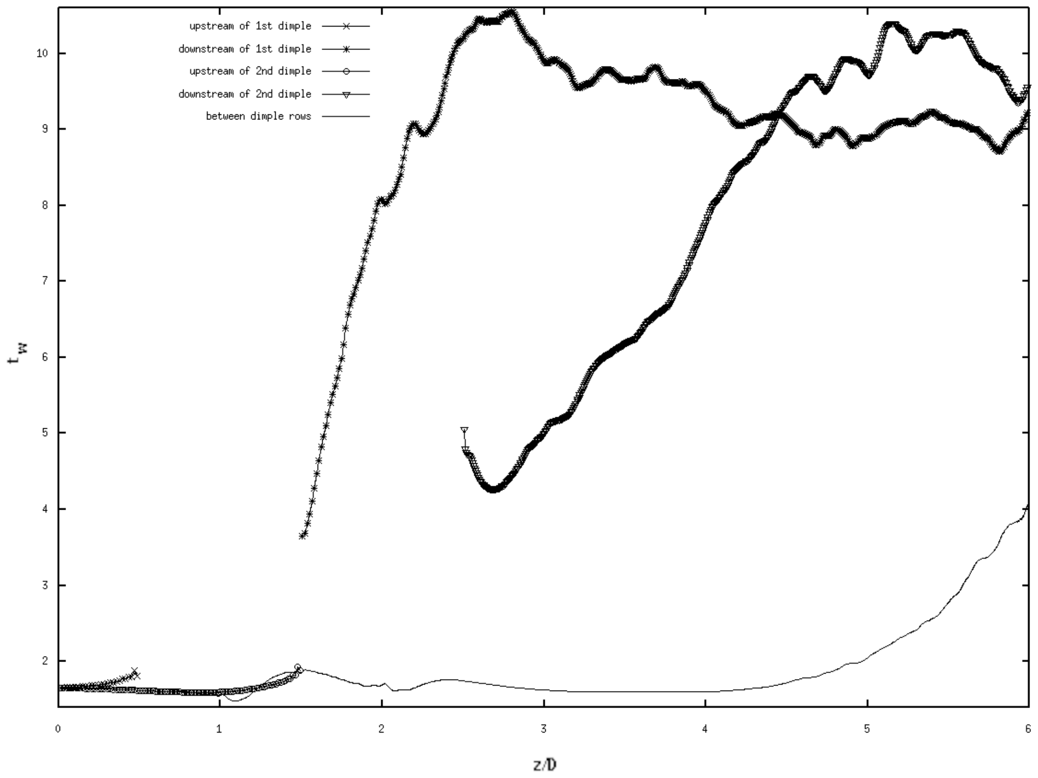

Figure 26. Wall shear stress, τ_W along the flat plate.

The wall shear stress shows the stabilization of the transition to turbulence behind the dimples as shown in Figure 26. The first dimple has a much steeper increase in the shear stress and peaks higher than behind the second dimple, but τ_W decreases after it peaks before leveling out. This same behavior is not seen behind the second dimple. As well there is a drop in the shear stress immediately after the second dimple that is not seen behind the first. This implies that the transition to turbulence due to the second dimple is different than the transition in the first wake. The reason for the difference is the existence of the first dimple row. The disruption in the boundary layer from the first dimple is not confined to the immediate wake region though that is where the majority of the influence lies. The quiescent fluid upstream of the dimples is disrupted across the span and causes the flow inside and the transition by the second dimple to be different than the first. By looking at τ_W between the dimples the effect can be seen. The disturbance in the boundary layer where the first dimple is (z/D =0.5 to 1.5) shows a dip then a peak before the second dimple. The effect is minor compared to the transition caused in the wake, but the result is that there is a difference in that the transition in the second wake is much slower to develop to a fully turbulent flow compared to the wake behind the first dimple row. Though the wakes never meet in this domain the shear stress between the wakes near the edge of the boundary does start to creep up which implies that at some point downstream the flow will transition to turbulence, and the flow is already beginning to transition there, but at a much slower rate than directly behind even the second row.

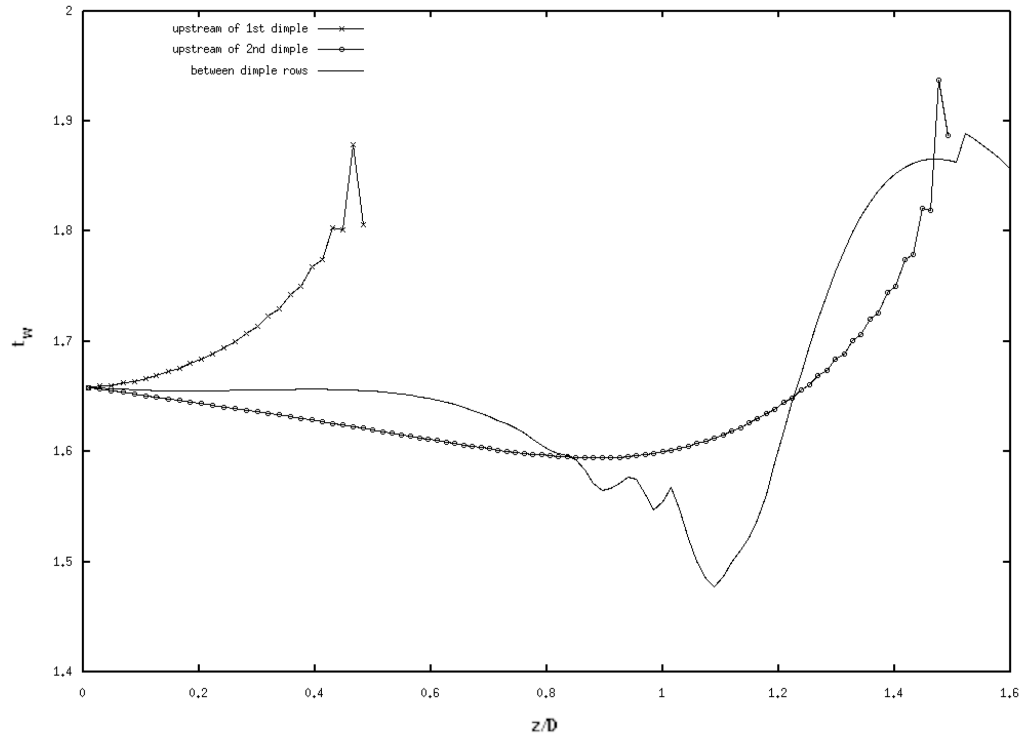

Figure 27. Wall shear stress, τ_W increases as the flow accelerates leading to the dimples.

The wall shear stress before the dimples also has an interesting charateristic that is indicative of influence of the dimple on the boundary layer before the flow even reaches the dimples. The plot in Figure 27 shows that the shear stress increases just before the dimples as the boundary layer is forced to accelerate prior to entering the dimples. By looking at the shear stress at the wall it is apparent that the assumption that the dimple did not influence the flow upstream actually does not hold true. The flow upstream of the dimple very near the wall shows influence of the downstream dimples. This is due to a pressure difference that is caused by the dimples. Since the wall expands away from the flow a lower pressure region is created than the upstream flow, which causes the flow in the boundary layer to accelerate. This acceleration is not seen in the previous simulation, but is clearly an artifact of the presence of the dimples. The entry length of the domain is not far enough from the first dimples. The wall shear stress upstream of the first dimple increases as is indicative of an accelerating boundary layer, but τ_W upstream of the second dimple decreases as would happen with a normally increasing laminar boundary layer, then has an inflection point about $z/D = 0.7$ upstream of the dimple. Since the first dimple is only $z/D = 0.5$ from the inlet, the inlet is too close to the first row to be outside of the influence of the dimple. The effect of the dimple being too close to the inlet is minimal, but the result is important to note nonetheless.

The statistics shown previously approximate an isotropic variation in the spanwise dimension, but due to the nature of how the flow is tripped with a bias in the spanwise dimension this assumption is not entirely valid. There is spanwise variation that exists in the time averaged velocity field as a result of how the flow transitions to turbulence by themselves influence of the dimples. The plots of the streamwise velocity contours in Figures 28 and 30 show that the flow far downstream appears to have greater homogeneity, but there is still a clear difference in the velocity field behind the dimples and between the dimples. The approximation of the constant velocity field for this simulation breaks down in the intermediate layer, and the part deviation from [1] and [2] in the velocity is accounted for here. In Figure 30 the velocity at $y = 0$ and $y = 10$ shows a lower velocity further away from the wall than at $y = 5$, and also has a higher velocity nearer to the wall. This is due to the flow being turbulent in the wake regions and only beginning to transition between the wakes. The difference in the velocity contours at $z = 60$ against the velocity contours at $z = 25$ shows how the wake grows in terms of velocity. The turbulent boundary layer at $y = 0$ at $y = 10$ grows toward each other. The resulting mixture of the wakes causes the flow to transition in between the dimples. If the second dimple was placed closer the flow would be more homogeneous since the transition that occurs in the wakes of the dimples would be closer. In addition, since higher velocity fluid in the turbulent boundary layer is closer to the wall a dimple within the wake would cause an even larger effect on the fluid as the perturbation of the boundary layer would be influenced more. The idea is that the higher momentum boundary layer will have much more interaction with the dimple and the separation within the dimple will be much smaller in the dimple in a turbulent boundary layer than in a laminar boundary layer.

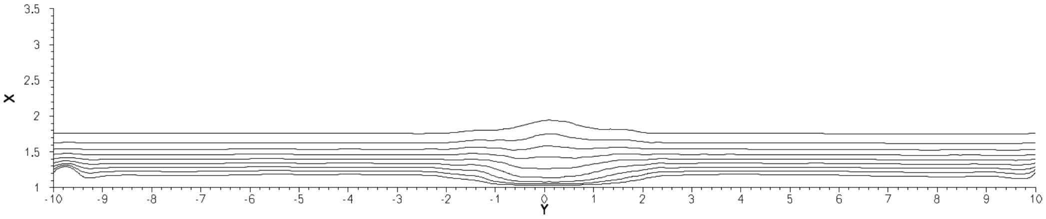

Figure 28. Streamwise velocity contours in an x-y plane at $z = 25$ shows variation in the span.

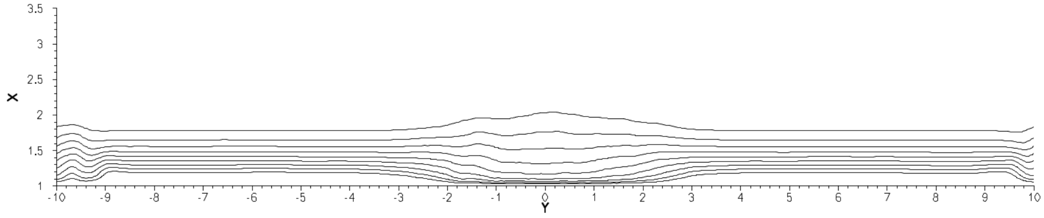

Figure 29. Streamwise velocity contours in an x-y plane at $z = 35$ shows variation in the span as the wake grows.

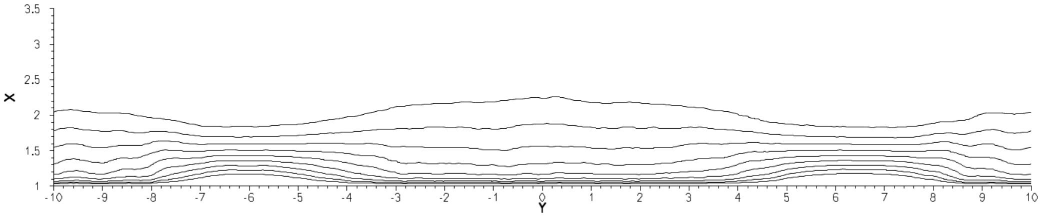

Figure 30. Streamwise velocity contours in an x-y plane at $z = 60$ where the wakes have not converged at the edge of the domain.

To understand how isotropic the turbulence is at locations downstream of the dimples w_{RMS} is plotted in Figures 31, 29 and 33 for $z = 25$, $z = 35$ and 60, respectively. The beginning of the turbulent transition caused by the dimple rows is distinct just at the trailing edge of the dimples. The transition structure is also apparent in these plots. The effect that the turbulent wake has on the laminar regions downstream of the dimple is also apparent in these plots. The dimples in the laminar flow cause the transition to occur, but only in a small region in the center at the trailing edge of the dimple. The distinct turbulent structure of the wake appears as a large oblong shapes in the plot of the w_{RMS} velocity contours in Figure 31 grow down the plate. The flow between the wakes of the dimples grow as the high turbulent energy fluid near the wall disturbs the quiescent flow and in turn the flow begins to transition. The flow between the wakes begins transition before the wakes grow enough to converge. Though the turbulent flow does not fully develop within the computational domain it is apparent with the dimple arrangement that the wakes converge before the flow between transitions.

Of interest is how the region from the first dimple $z/D = 1$ downstream is still localized. As the wakes expand from the dimples into one another the turbulence tends towards quasi-isotropic turbulence in the y. At $z = 60$ there is still influence of the dimple seen. regions localized between the dimples where the edges are upstream is still a region of localized fluctuations. Additionally, the fluctuations caused by the second row are larger than the rest of the flow. Further downstream the flow may be able to fully mix as would be expected, but the domain is restricted before this would occur.

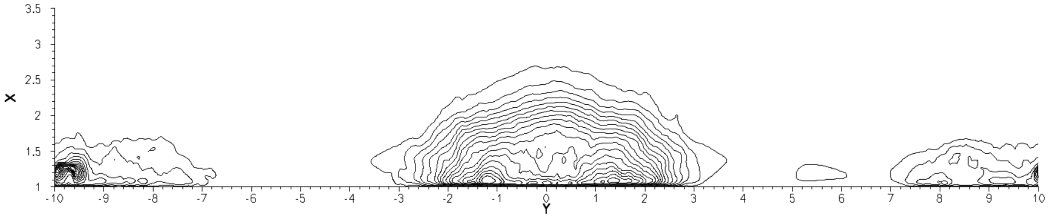

Figure 31. Streamwise RMS velocity in an x-y plane at $z = 25$ shows the distinct wake of the first dimple.

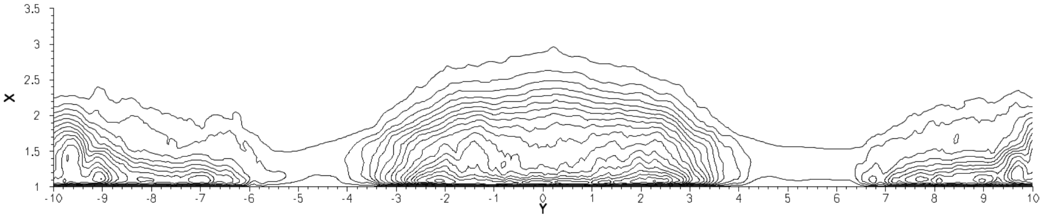

Figure 32. Streamwise RMS velocity in an x-y plane at $z = 35$ where the first dimple has grown and the second is developing.

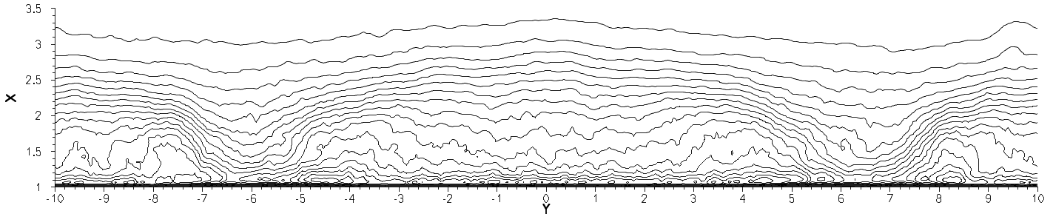

Figure 33. Streamwise RMS velocity in an x-y plane at $z = 60$ with the transition across the span.

The contour plots of the streamwise velocity inside of the dimples show the flow structure at the center of the dimples. In the plot in Figure 34, the flow is separated over nearly the entire length of the dimple. The flow reattaches on the back side of the dimple. The boundary layer is perturbed at the trailing edge of the dimple which shows downstream as the flow transitions to turbulence. The transition to turbulence is immediately active in the entire domain as can be seen in the second dimple row.

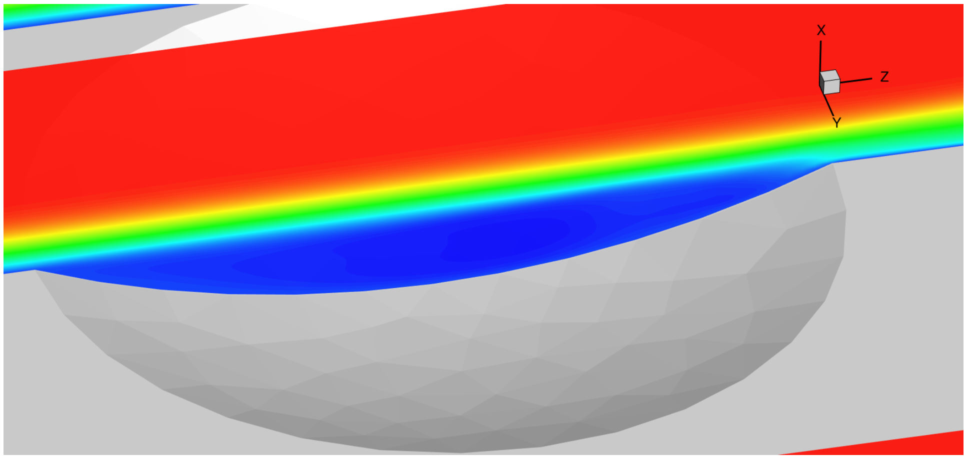

Figure 34. Time averaged streamwise velocity contours at the center of the first dimple.

The time averaged flow inside of the dimple is better characterized by streamtraces shown in Figure 35. There are two distinct eddies on either side of the center of the dimple. The eddies inside are turning counter the bulk flow. There also is a directional bias in the dimple from right to left as the flow moves through the dimples that appears in the streamtraces. The production of turbulence in the dimples occurs on the back side of the dimples. The boundary layer is thick enough to flow over most of the dimple, but does reattach inside of the dimple. The result is production of streamwise vortices that initiate turbulence. The region where the flow reattaches on the back side of the dimple distorts the eddies to form a butterfly shape, and contains a region where there are more streamwise vortical structures. The production of turbulence in the first dimple is localized on the trailing edge since the eddies interact with the free stream velocity in this region. The streamwise vortical structures are seen in experiments as well, and are a characteristic of flow over dimples and initiation of transition to turbulence [18]. As a result of inducing the change in the spanwise component in the velocity field non-localized regions are affected. The streamtraces in Figure 36 are above the dimple at an x location of 1.1. The vortical structure on the backside can be seen here as well as influence in the spanwise velocity field.

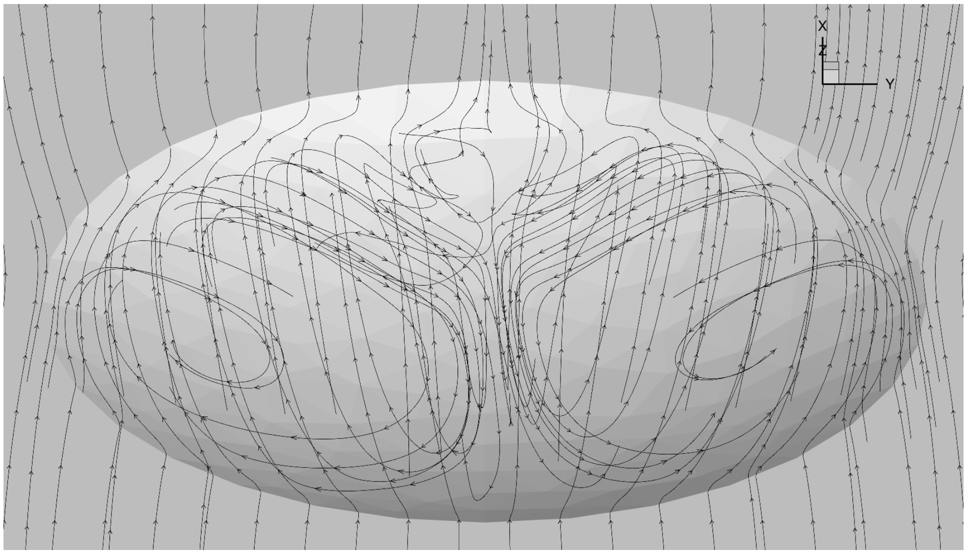

Figure 35. Streamtraces in the time averaged velocity field in the first dimple.

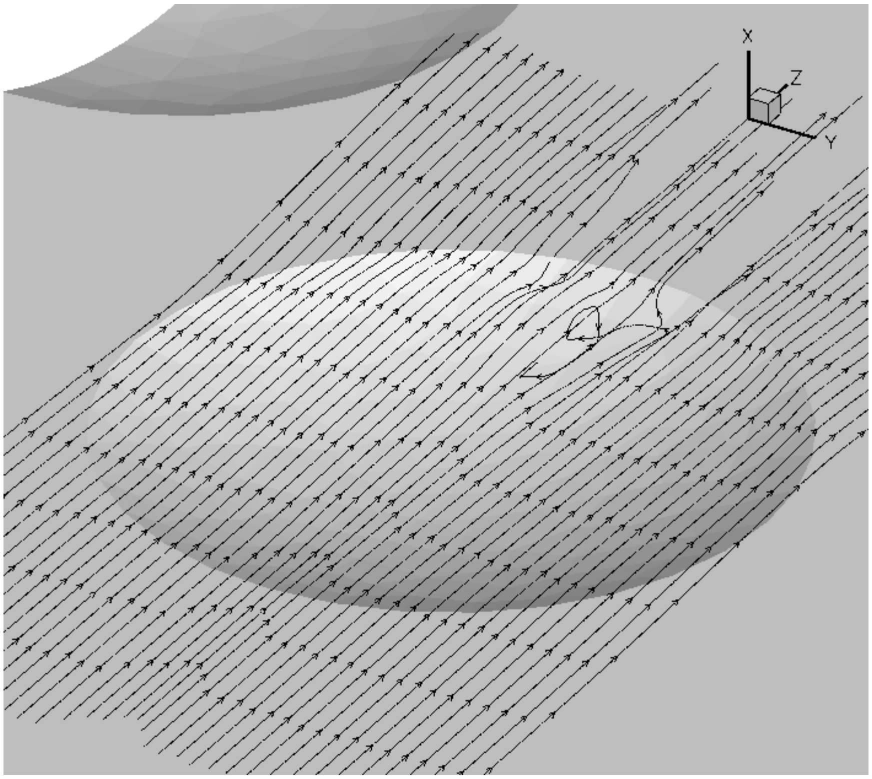

Figure 36. Streamtraces in the time averaged velocity field at a location of 0.1 above the wall.

The same flow structures in the first dimple are also present in the second dimple. The reattachment point in the second dimple is roughly at the same location in the dimple as in the first, near the top edge on the trailing edge of the dimple. There is interaction between the staggered dimples, as can be seen with the stream traces in Figure 38. Though this influence does exist, the effect appears to be minimal, because the effect is too small compared to the influence of the bulk flow.

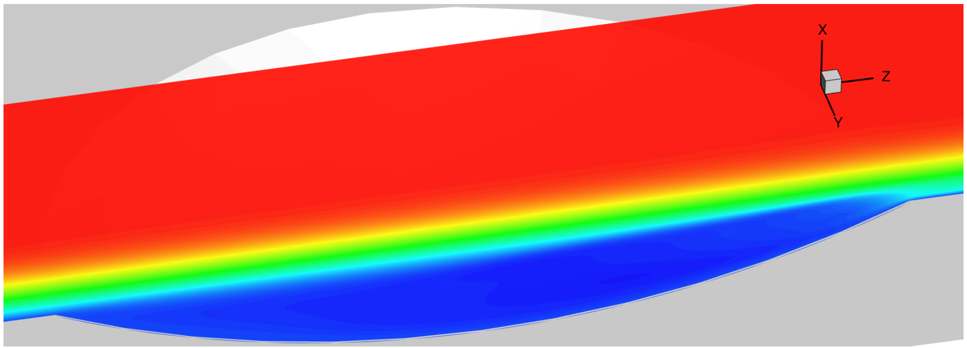

Figure 37. Time averaged streamwise velocity contours in the second dimple.

This small alteration in the mean flow has profound influence in the flow inside of the second dimple. Shown in Figure 38, the recirculating eddy inside of the dimple does not have a singular distinct eddy structure, but instead has an irregular flow that increases the amount of the turbulent production. The region of flow where the turbulent production is highest is not significantly larger in the spanwise direction, but is further upstream inside of the dimple as well as deeper in the dimple. Comparing the stream traces in Figure 39 shows that the structures inside of the dimples is nearly identical. Even though there is influence of the first dimple onto the second with the velocity field being distorted in the spanwise direction i.e. the fluid from the first dimple moves laterally into the second. It is also apparent that this same influence from the first onto the second is also occurring upstream of the first dimple as a result of the low pressure region of the first dimple.

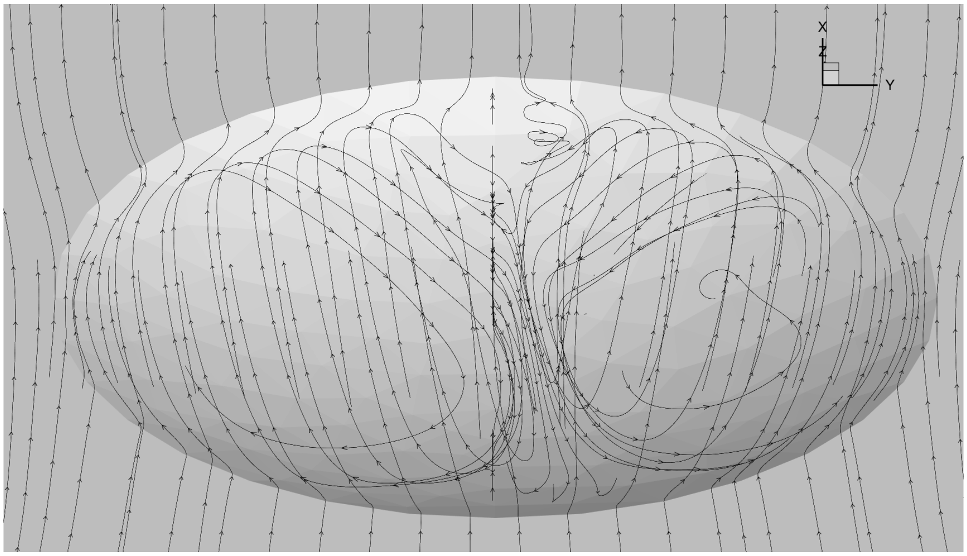

Figure 38. Streamtraces in the time averaged velocity field inside of the second dimple.

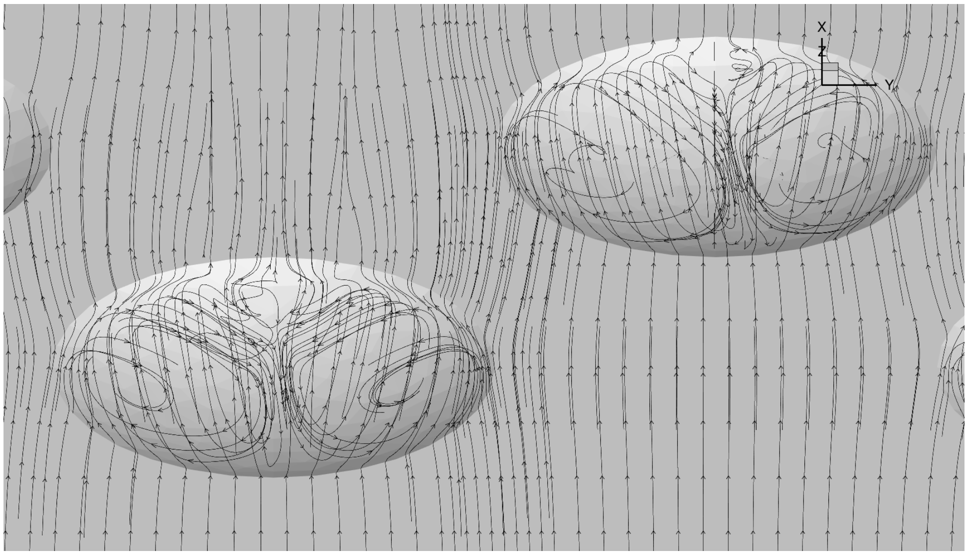

Figure 39. Streamtraces in the first and second dimples show the interaction between the dimples.

The flow over the first dimple shows characteristics of flow over a cavity where the flow is separated and reattaches downstream inside of the dimple. The initiation of turbulence occurs on the backside of the cavity due to the perturbation on the boundary layer and the influence on the bulk flow. The instabilities in the boundary layers the primary mode of initiation for transition mechanisms seen in the dimple. The instabilities can be seen by the rotation seen in the stream traces in Figure 36.

Unlike a flat plate with a backward facing step the dimple does not allow for reattachment along a flat surface. Instead the reattachment occurs on the upward curvature of the dimple. The separation causes instabilities in the shear layer to propagate turbulence downstream as the reattachment point inside of the dimple changes over time. Investigation of this is beyond the scope of the current work. In the instantaneous plot, however, slight oscillations in the streamwise velocity above the dimple show that there is some instabilities manifest over the dimples.

The reattachment point in the center of the first dimple is visualized by the zero streamwise velocity line and with the vectors in the time averaged plot in Figure 40. Since the boundary layer is the same thickness at the dimple as the dimple depth, d, the momentum in the boundary layer carries it over most of the dimple. Since the boundary layer is separated for most of the dimple and only reattaches very near the outer edge of the dimple where the effective length of the dimple relative to the streamwise velocity, the most significant perturbation in the boundary layer is localized to where the boundary layer interacts directly with the dimple. The influence of this first dimple is enough however to cause the flow to transition. The effects are seen immediately in the second row of dimples.

Even with the strongest perturbation residing near the center of the cavity, the effect of a dimple being offset from the second row is that the flow at the leading edge of the dimple is the same as the freestream, but the separation in the second dimple is less compared to the first row as seen in Figure 41. Since the separation is less in the second row there is a cumulative effect of dimples downstream and an interaction between staggered dimples that will manifest in more turbulent production in downstream dimples.

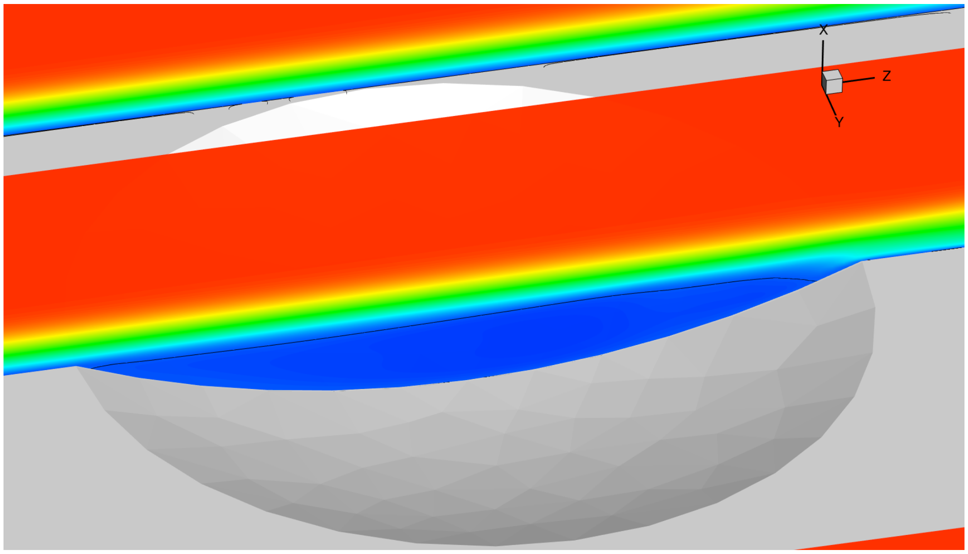

Figure 40. Separation of the boundary layer visualized by velocity color contours with a zero streamwise velocity contour line inside of the first dimple.

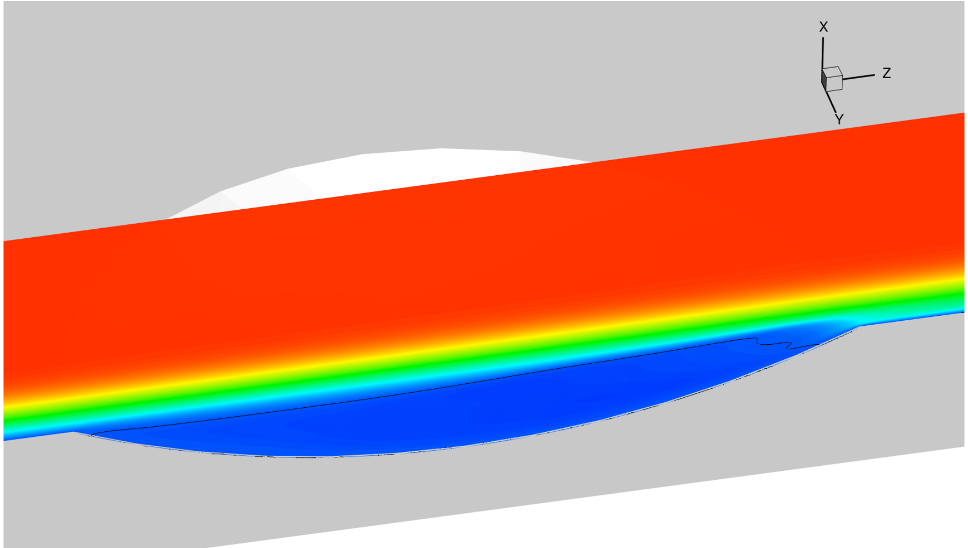

Figure 41. Separation of the boundary layer visualized by velocity color contours with a zero streamwise velocity contour line inside of the second dimple.

On a nominal flat plate Blasius solution the laminar boundary layer grows. For this Re_d the same behavior was confirmed in the preliminary investigation, but the dimpling of the plate causes an interesting phenomenon in the boundary layer. Instead of the expected growth the boundary layer actually does not increase. This is due to a low level acceleration that was seen in τ_W with the constant boundary layer height seen in Figure 22.

The freestream flow above the dimple is affected as well. The flow in the outer boundary begins transitioning towards turbulence as can be seen in the slight fluctuations in the streamwise velocity shown in Figure 42. These minor fluctuations propagate downstream to become much larger eddies in the wake region caused by small movement of the fluid within the dimple. The low velocity of fluid rotates in the dimple in much the same way as flow in a cavity driven by velocity on the top surface and is indicative of bypass transition [24]. The dominance of the perturbation of the boundary makes the initiation of bypass transition difficult to discern directly behind the first dimple, but the transition of the laminar flow between the dimples is more indicative of this behavior.

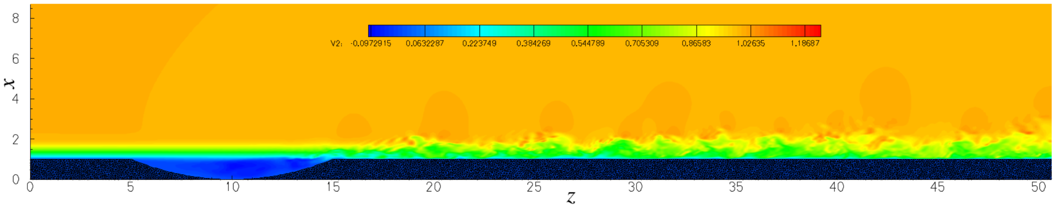

Figure 42. Instantaneous streamwise velocity contours in an x-z plane at $y = 0$.

The oscillations seen in the second dimple shown in Figure 43 are less pronounced than the first possibly due to the larger boundary layer thickness at the second dimple. The periodicity of the fluctuations is still present are not necessarily the same shedding frequency as the first dimple. Since the influence of the second dimple does not interact as significantly with the higher velocity fluid the modes of disturbance have a longer wavelength than in the first dimple, and does not have the same short wavelength disturbance that is present in the first dimple resulting in transition that does not develop as quickly as in the wake of the first dimple. The result, however of the disturbances in the boundary layer is similar to dirsturbing the boundary layer by using turbulence in the freestream to penetrate the boundary layer and ring modes to initiate turbulence as the result from [23] and [25] shows. The dimples at the wall cause this disturbance to occur at the wall-boundary layer interface. The disturbance of the boundary layer by the dimples must disturb the boundary layer and initiate turbulence. In the present thesis the turbulent spot occurs at the same point in space at the trailing edge of the dimple and initiates turbulent transition in the wake.

The contours of streamwise velocity in Figure 45 show for a certain point in time how the perturbation caused by the dimples grows and forces turbulent transition at three planes in the span. There is also a periodicity to the fluctuations similar to vortex shedding of bluff bodies or flows over cavities. The plot of the contour slices through the different dimple rows in Figures 44 show that the velocity fluctuations in the wakes of the dimples are essentially different. Since the perturbation in the first row is higher there are more intense eddies in the wake than those downstream of the second dimple. The initiation of the transition to turbulence in the wake of the first dimple is also immediate, whereas there is a significant delay in the transition in the wake of the second. This behavior was also seen in the τ_W. As the wakes themselves interact it also becomes apparent that the turbulence becomes more isotropic in the spanwise dimension. The transition to turbulence due to the dimple row directly downstream is telling about how the dimples interact with the boundary layer. It is evident that the first dimple row has much greater influence immediately in the turbulent transition because of the magnitude of the perturbation is much greater due to the thinner boundary layer incoming to the dimple. More subtle is that the first dimple row has changed the flow dynamic immediately downstream in a way that alters how the second dimple interacts with the boundary layer in a profound manner. The flow structures of both dimples is very close in shape, but the region within the dimple that interacts and perturbs the flow in the first dimple is wider than in the second dimple. This implies that the first dimple has more interaction and thus a greater perturbation on the boundary layer than the second dimple. Since the perturbation in the second dimple is small, onset of the turbulent transition occurs a slower pace.

Figures 45 and 44 show the difference of the wakes by visualization of instantaneous velocity by plotting color contours. It is very clear in these two plots the difference in the initiation to transition occurring much further downstream of the second dimple compared to the transition in the first wake. In Figure 44 the mechanism for the transition of the regions between the wakes is also apparent. The wakes "grow" as a result of the turbulent energy in the wake as it perturbs the neighboring laminar boundary layer. The shape of the wake is also telling of how the transition occurs over the dimples. Essentially the entire span is “covered” in dimples, but the entire span does not transition as a result of the dimples. The reasoning is simple, the boundary layer height is 1, which is the deepest location on the dimple, and so the transition is localized from the interaction from a small region on the backside of the dimple. Even the small increase in boundary layer has a profound impact on the transition in the second dimple. The reattachment line of the boundary layer within the second dimple is so small that the level that the flow is perturbed is significantly less than the perturbation from the first dimple. Even at the same Re_d it would be expected that having a slightly smaller δ_i will have a profound impact on the result. If the dimples were $1D$ further upstream in the boundary, the wakes of both dimples will be more pronounced, such that the wake of the second dimple would look very much like the current results of the wake of the first dimple, and the wake of the first dimple will be even more pronounced.

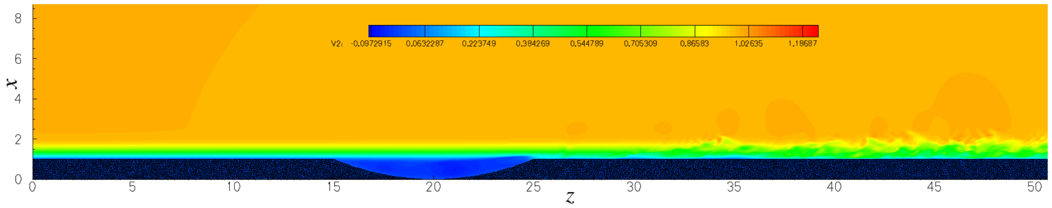

Figure 43. Instantaneous streamwise velocity contours in an x-z plane at $y = 10$.

To visualize the turbulent structures in the wake of the dimples the Q-criterion is used in a similar way as in [20]. Q is the second invariant of the velocity tensor, and is used as a flow visualization technique to identify convex, low pressure vortex cores [20]. The result shows how the turbulent structures take shape in the wake as well as define the shape of the wake. The plot of Q in Figure 46 is an isosurface at 0.3 with color contours from streamwise velocity, w. The transition in the wake behind the first dimple initiates immediately, whereas the transition of the second dimple has a bit of a delay before beginning the transition. Clearly the transition in the second wake takes on a different mechanism for transition than the first. The perturbation from the first dimple forces the transition immediately without the delay seen in the second dimple.

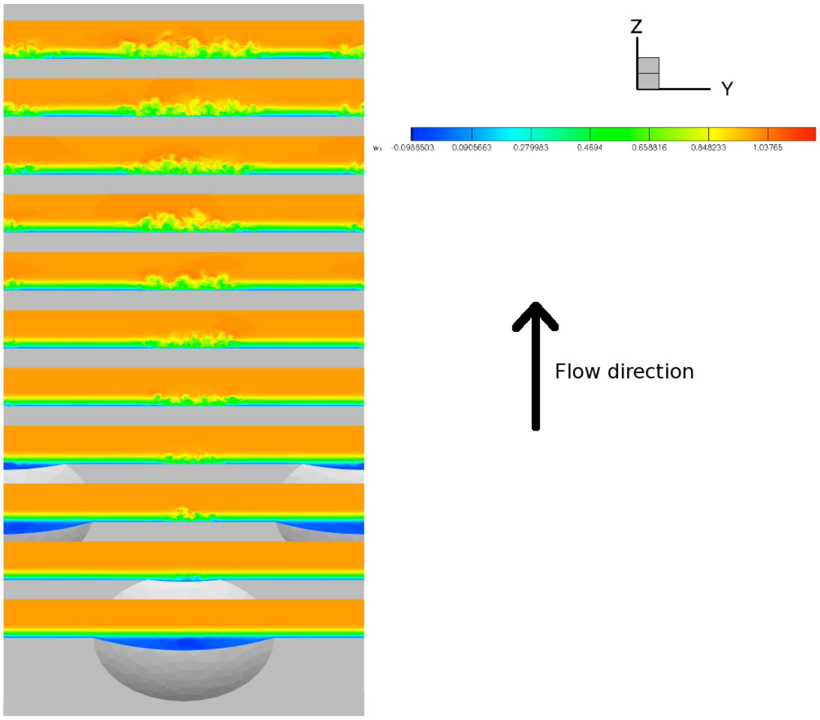

Figure 44. Instantaneous streamwise velocity contours in x-y planes at locations along z.

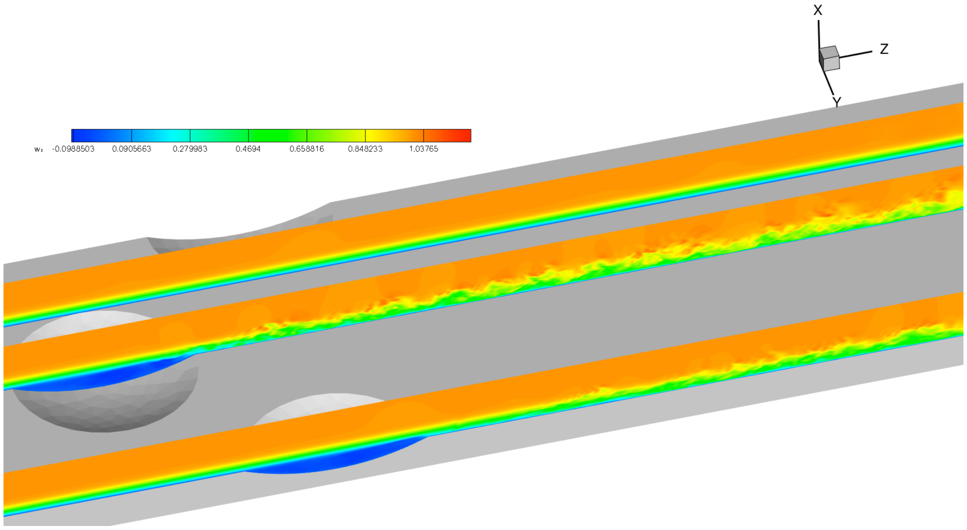

Figure 45. Instantaneous streamwise velocity contours in planes at $y = 0$, -5 and 10.

The turbulent production begins in the first dimple and occurs on the trailing edge where the instabilities in the boundary layer begin, and there is interaction of the turbulent wakes downstream of the dimple rows at about $z/D = 2$ downstream of the second dimple row.

This is in good agreement with what would be expected based on the velocity contours where the instabilities occur off the trailing edge and begin to mix downstream at $z/D = 2$ from the leading edge of the second dimple. The turbulent production is driven by the interaction of the boundary layer with the dimple. Since the momentum in the reattachment and detachment off the trailing edge is changing drastically turbulent production is expected to be high. The turbulence due to the first dimple in the wake is apparent as a cone downstream of the dimple but do not enter the second dimple row directly. As would be expected the turbulent production in the second dimple is larger and over a larger region inside of the dimple. The turbulence in the wakes converge downstream. Since the turbulence intensities in the wakes are different complete mixing cannot occur immediately.

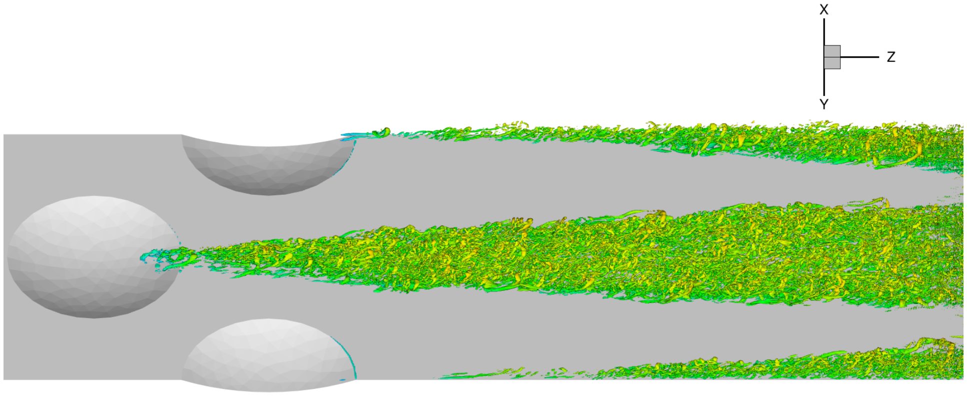

Figure 46. Isosurface of $Q = 0.3$ colored with streamwise velocity.

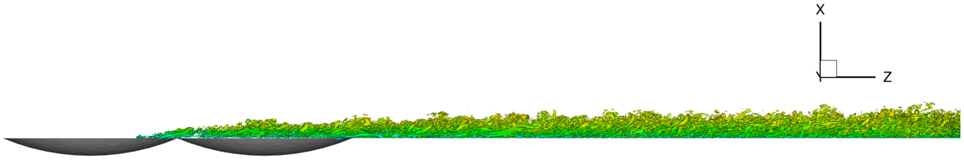

Figure 47. Side-view of isosurface of $Q = 0.3$ colored with streamwise velocity.

The vorticity contours in Figure 48 serve to visualize the structures in the boundary layer in a way that cannot be seen by the visualization by Q. Vorticity in the first dimple confirm that the instabilities begin towards the trailing edge where instabilities begin. The vorticity in the wake of the first dimple row shows how the boundary layer is perturbed slightly and turbulence develops in the wake as those initial instabilities grow in the wake.

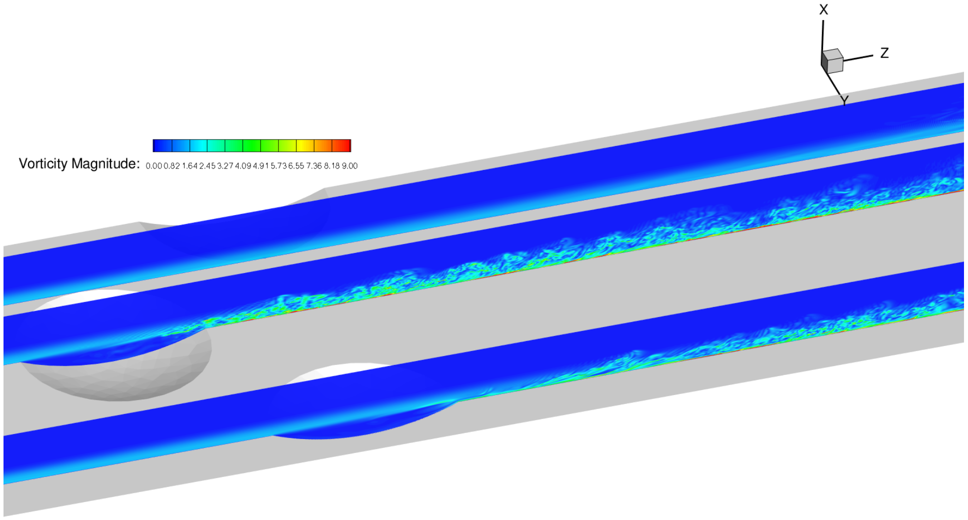

Figure 48. Vorticity magnitude contours in planes at $y = 0$, -5 and 10.

In contrast, the turbulence downstream of the second dimple develops much slower, because the level of perturbation from the second dimple is lower than in the first dimple. This is a direct result of the thickness of the boundary layer at the location of the second dimple being thick enough to separate over nearly the entire dimple, as opposed to the thickness at the first dimple which cause the separation to be less. Considering these results it seems that there is a bit of a balance to consider for the depth of the dimple against the thickness of the boundary layer. If the boundary layer is too short, i.e. Re_z is small, compared to the depth of the dimple then the boundary layer will remain attached through the dimple. With a boundary layer that is too thick, even at higher Re_z the perturbation in the boundary layer will be too small to cause the flow to transition to turbulence at the same rate as in the first dimple.

Vorticity isosurfaces of level 5 with streamwise velocity contours to show the wake region in Figure 49 show again how the transition is similar, yet develops at a different rate downstream of each of the dimples. Apparent with this level of vorticity visualized is the longitudinal structures in the boundary layer near the wall and the smaller structures that are ejected out of the boundary layer as the energy in the boundary layer increases toward the boundary layer edge. On the trailing edge of the dimple the vorticity also highlights a structure that is indicative of how the fluid is moving out of the surface is causing the flow to turn. This effect also will have a stronger impact on the flow in a regime where the boundary is thinner. The geometry of the dimple allows for such a condition. The reattachment of the flow just before the end of the dimple causes higher velocity flow to be nearer to the wall which acts as a very thin boundary layer that will be disturbed. The disturbance in the flow is amplified by the momentum of the fluid. The result is shown in the rate turbulent transition in the first wake compared to the transition in the second wake.

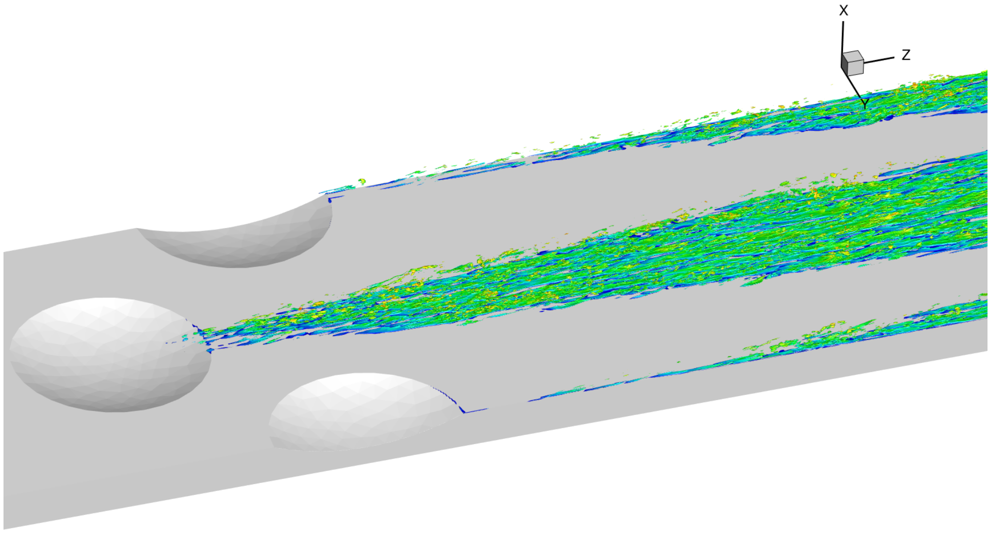

Figure 49. Vorticity magnitude isosurface of 5, with streamwise velocity color.

To visualize coherent structures in the turbulence the level of turbulence used in the isosurface is increased to 10 in Figure 50. The streamwise vortical structures become apparent at this level about $z/D = 0.5$ downstream of the first dimple in the wake. This confirms the notion that the transition to turbulence is delayed as a result of the perturbation in the second dimple. By contrast, the turbulent intensity created by the first dimple is much higher as the structures in the wake do not have a delay in the same manner.

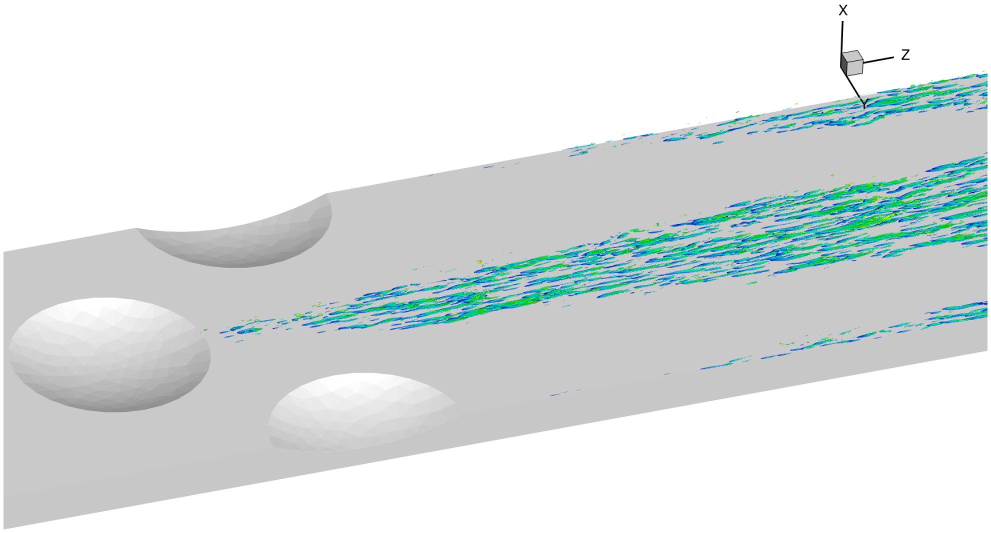

Figure 50. Vorticity magnitude isosurface of 10, with streamwise velocity color.

The same vortical structures are seen in Figures 52 and 53 where the wakes have converged. The coherent structure of the longitudinal vortices is characteristic of the structures observed by [17] in the boundary layer closest to the wall.

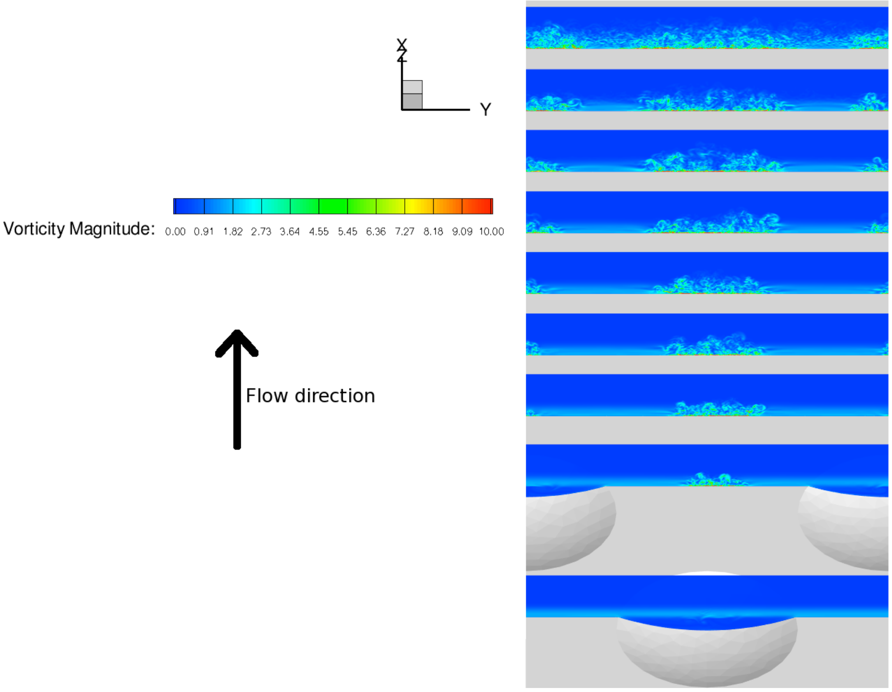

Figure 51. Streamwise vorticity contours at x-y planes at planes along the z-axis.

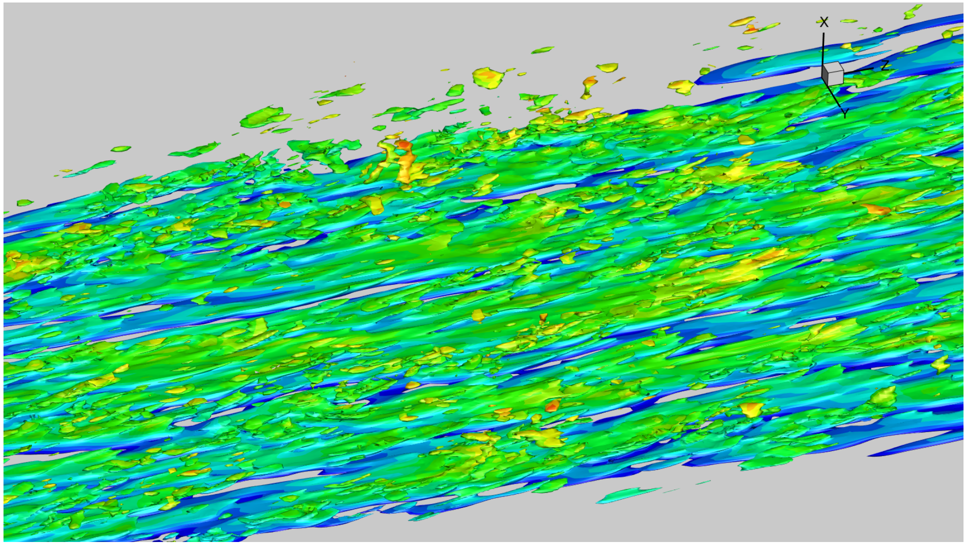

Figure 52. Vorticity magnitude isosurface of 5, with streamwise velocity color in the wake region to illustrate longitudinal vortices.

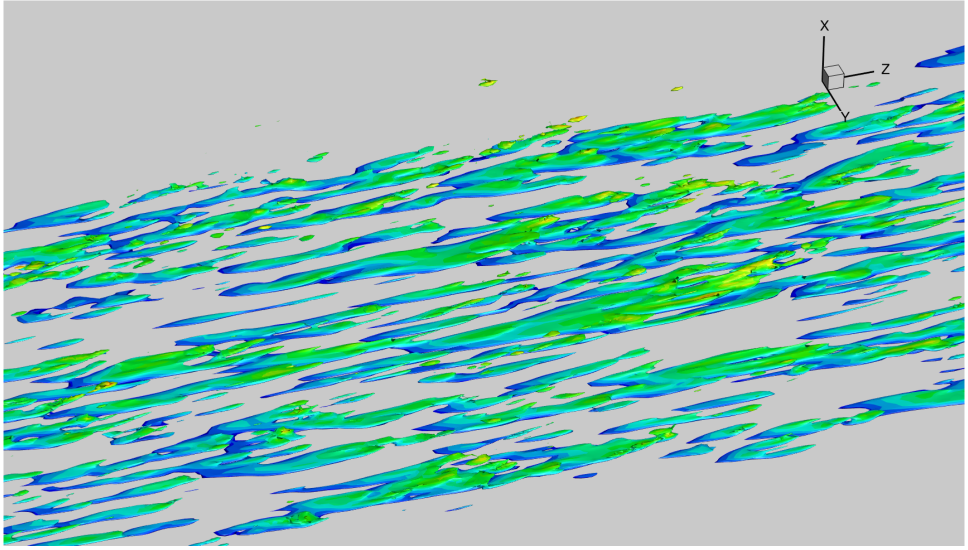

Figure 53. Vorticity magnitude isosurface of 10, with streamwise velocity color in the wake region to illustrate longitudinal vortices.

C. Simulation of Three Dimple Rows

The results from the two dimple row simulation drives the motivation to investigate into the cumulative effect of dimples downstream. Such a configuration is common in practice e.g. a golf ball, where there are more than one or two rows of dimples. The transition to turbulence in the boundary layer due to the first rows of dimples will alter how the boundary layer/dimple interaction in downstream dimples. Momentum near the wall is higher causing dimples downstream to have a more profound effect on the turbulent production. This turbulent production is higher where the velocity near the wall has larger momentum changes by the dimples.

There was some hint that the rows of dimples are influencing each other, but since there was not direct influence in the wake the cumulative effect cannot be seen unless placed directly in the wake of the first dimple. The hypothesis is that the third row will have received more influence in the transition mechanisms, and the transition will be much different, but how it will be different is intriguing. The second row of dimples actually showed the transition to not occur as fast in the wake, and there was two distinct wake patterns that did not converge even after $z/D = 3.5$ downstream. The interaction between the first row on the second row is indirect in terms of the turbulent energy, but addition of a third row in line with the first row will mean that the turbulent transition will have begun to occur directly upstream of the dimple. The fluid entering the third dimple will have a transitioning boundary layer, which is considerably thinner than a laminar boundary layer and will have turbulent energy entering the dimple. The third dimple will then enhance the transition.

As compared to two rows of dimples we can see that the velocity in the boundary layer in the wake $z/D = 2.5$ downstream of the last dimple in Figure 54 the velocity in the intermediate region is much different. In the viscous sublayer however the flow is very much correlated to expected values. The boundary layer shape is altered considerably by the addition of another row of dimples. The velocity in the viscous sublayer collapses to $w^+ = x^+$, but the velocity in the wake region does not fit the same trend for the plots with spanwise averaged statistics. This implies that velocity As well the variation in the span is much less. Figures 55 through 57 are much closer together than for the two row configuration. The addition of the third row forces additional turbulent production and mixing, which in turn causes the velocity field to reflect more homogeneous characteristics than the wake in the two row configuration.

The span-averaged profile from the three-row simulation shows that the flow has the characteristics of a turbulent boundary layer compared to the simulation of two dimple rows. The intermediate region still does show a difference from flat plate and pipe flow solutions, however. this may be due to the nature in how the flow transitions. Since the dimples force perturbations to occur in locations further away from the wall than the viscous sublayer the velocity in this region may be slower than for a flow with a much more subtle transition mechanism.

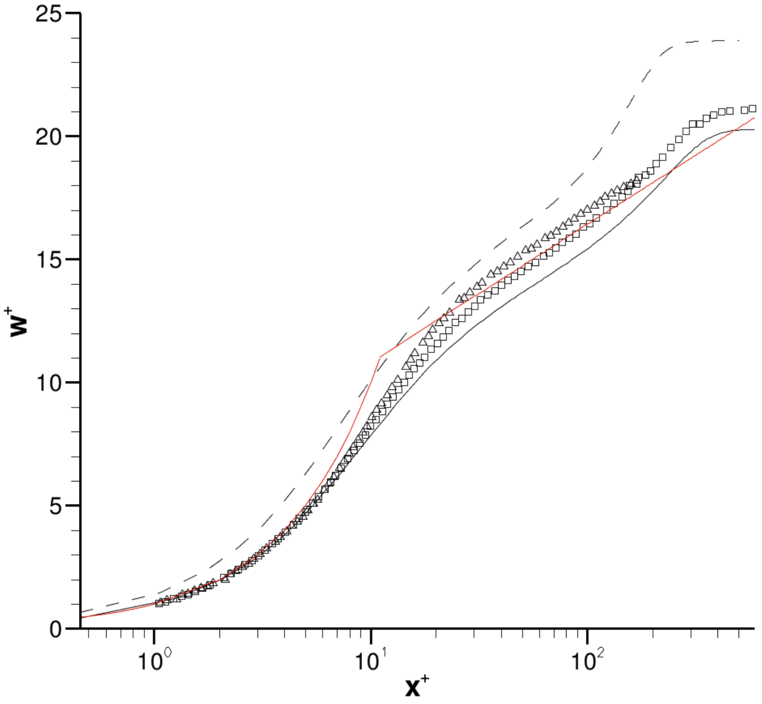

Figure 54. Mean velocity, w^+ against x^+. $-$ at $z = 60$, 3-row simulation; $--$, 2-row simulation; □, [1]; △, [2].

At the center of the span of the domain ($y = 0$), there is not much difference in the boundary layer veloctiy from the two-row simulation to the three-row simulation. The difference is mainly in the intermediate layer where the velocity shows a more developed turbulent boundary layer shape. The slight deviation from the reference in the intermediate seen in the two-row simulation is because the turbulence has not fully developed. The wake of the second dimple shows the same behavior. This means that the boundary layer in the second wake is not any more developed in the three-row simulation, because there is limited influence of the third dimple on the second wake.

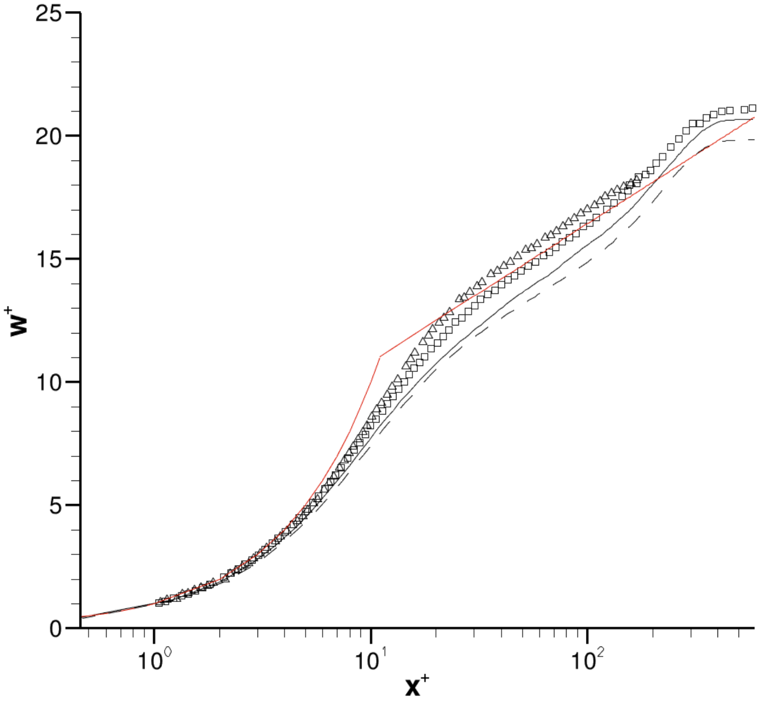

Figure 55. Mean velocity, w^+ vs. x^+ for three dimple rows at $y = 0$ and $z = 60$. $-$, 3-row simulation; $--$, 2-row simulation; $\square$, [1]; $\triangle$, [2].

The difference in the boundary layer at $z = 60$ between the center of the dimples ($y = 5$) for simulation with two rows compared to the boundary layer at the same location for the simulation with three dimples is great. The boundary layer seen in Figure 56 for the three-row simulation is clearly a turbulent boundary layer, whereas the boundary layer for two rows is beginning to transition only. The boundary layer at $y = 5$ is also showing more development than the boundary layer at $y = 10$. This shows how the wake of the third dimple is much wider than the wake of either the first or second dimples due to the level of turbulent production in the third row compared to the other two. How this production increases will become clear by examining the RMS velocity.

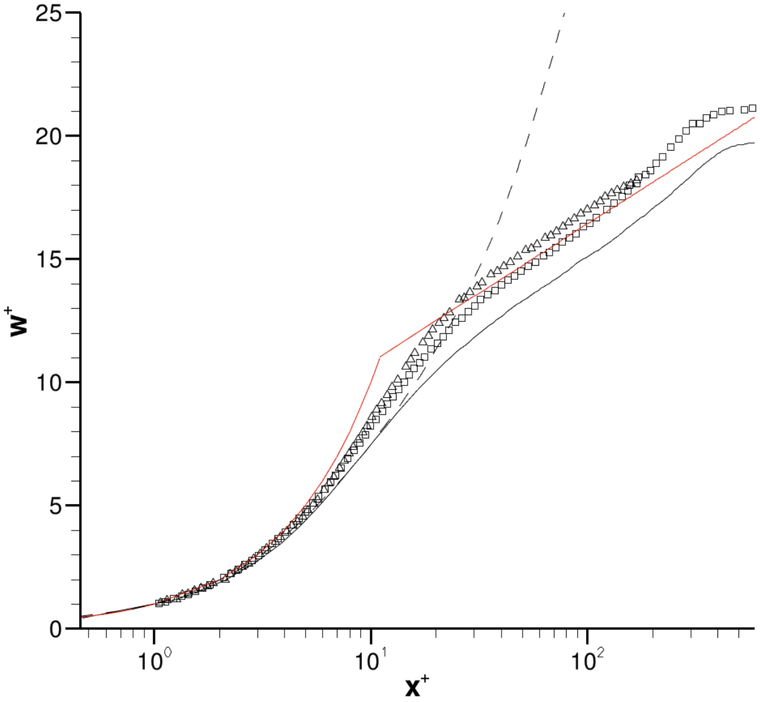

Figure 56. Mean velocity, w^+ vs. x^+ for three dimple rows at $y = 5$ and $z = 60$. $-$, 3-row simulation; $--$, 2-row simulation; □, [1]; △, [2].

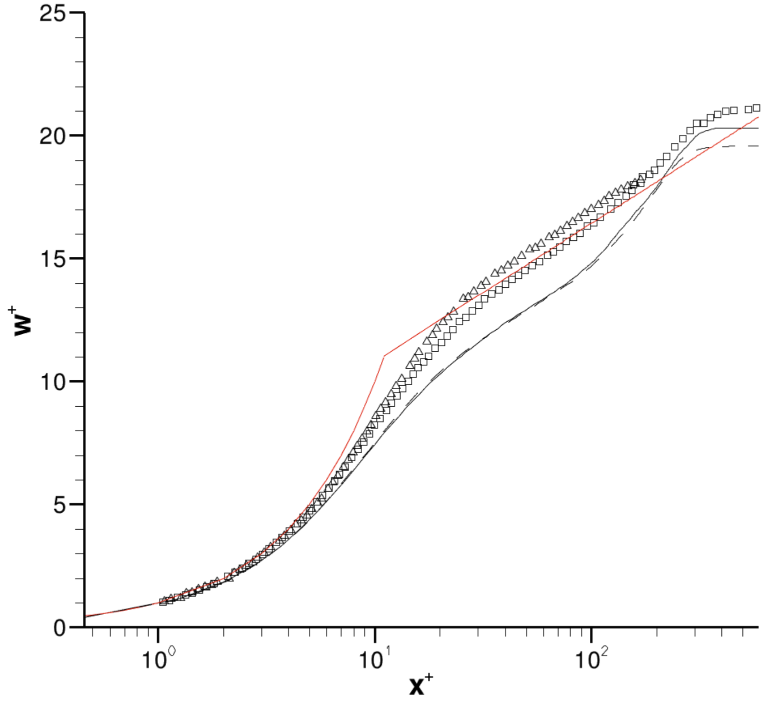

Figure 57. Mean velocity, w^+ vs. x^+ for three dimple rows at $y = 10$ and $z = 60$. $-$, 3-row simulation; $--$, 2-row simulation; $\square$, [1]; $\triangle$, [2].

RMS velocity contours at x-y planes along the z axis in Figure 58 show that the turbulent production in the third row dominates the center of the domain. The transition of the boundary layer due to the first dimple rows cause the flow to carry more momentum closer to the wall in the third row. The energy peaks off the trailing edge where the boundary layer separates and there is a localized region of highly fluctuating flow. The diminished boundary layer is caused by the first and second dimple rows allow the third row of dimples to cause higher fluctuations near the wall. The turbulent wake of the third dimple is also pronounced. At the edge of the domain the wake of the third dimple has almost forced transition over the entire domain. As well, the wake of the second dimple is still showing immature compared to the wake from the third dimple. The influence of the transitioning boundary layer incoming to the third row is clear in how the wake develops.

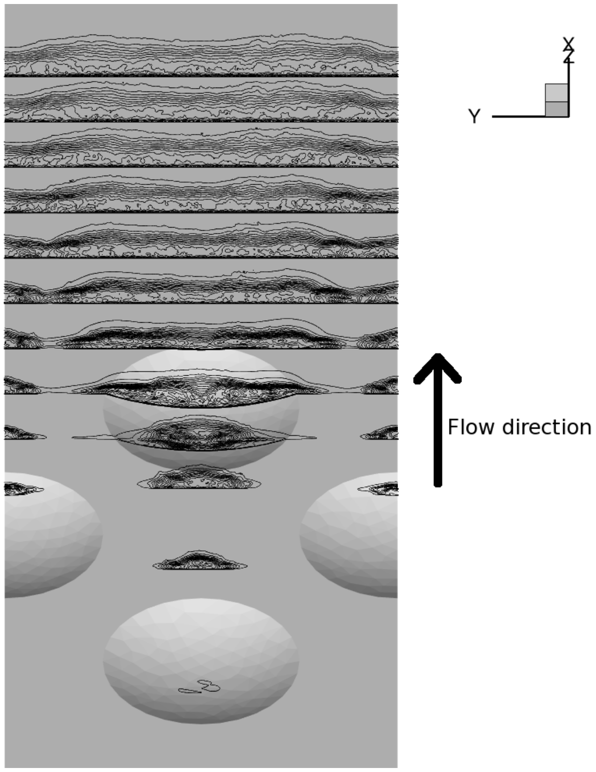

Figure 58. Contours of streamwise RMS velocity in x-y planes along the z-axis.

The incoming turbulent energy present in the boundary layer directly effects the strength of the turbulence caused by the dimple. The turbulent production in the boundary layer is amplified in the third dimple row from the wake of the first dimple. It is because of this that the third dimple row causes more turbulent mixing than either of the first or second dimples. Though the transition caused by the third dimple is high, it is unclear by the results in the present thesis if a dimple downstream of the third will cause a faster transition, however the production of turbulence of a downstream turbulence will be high, because the dimple will again perturb the boundary layer. Even in a turbulent boundary layer a small perturbation, such as a change in surface roughness can cause another inner layer to exist inside of the original boundary layer [32]. Additional dimples downstream might also have this effect as the dimple can be described as an effective roughness in this case, because the perturbation into the boundary layer is exactly at the wall and will propagate through the boundary layer.

Additionally, the RMS velocity at a z-location $2D$ downstream of the last dimple shows that the flow has more kinetic energy due to the fluctuations described by the RMS velocity shown in Figure 59. The energy in the wake of the three-row simulation do not die out in the intermediate and wake regions like that for the two-row simulation. This gives some insight into the transition mechanisms due to the dimples. Since the turbulent energy does not taper off higher in the boundary layer it is apparent that the effect of the dimple perturbing the flow is felt in the fluid far downstream of the dimple. Not only does the streamwise RMS velocity remain higher in the intermediate layer, but also the spanwise and wall-normal components experience much greater turbulent energy levels. Unlike the turbulent boundary layers of [1] or [2] the boundary layer in the present thesis shows a much greater energy level further downstream where the flow has completely transitioned to turbulence in the wake behind the third dimple. This result is also shared with the two-row simulation. Since the turbulence is nearly isotropic at $z = 60$ the plots in Figures 60, 61, and 62 show similar level and characteristics; particularly in the intermediate region.

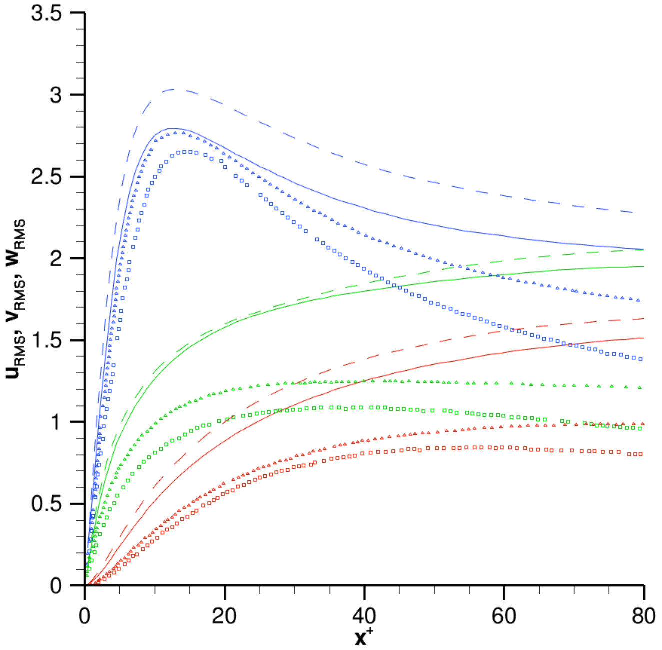

Figure 59. RMS velocity at $z/D = 2$ downstream of the trailing edge of the last dimple for $-$, 3 row; $--$, 2 row simulation,□, [1]; △, [2].

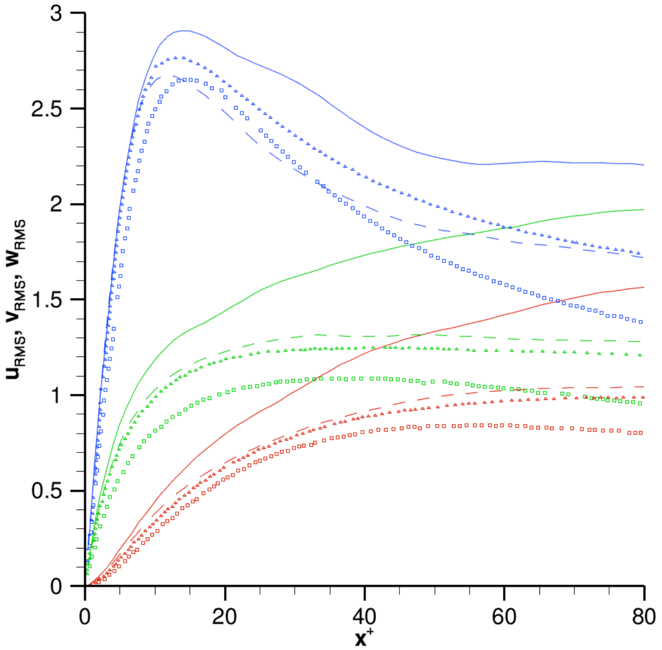

Figure 60. RMS velocity behind the first and third rows of dimple at $z/D = 2.5$ downstream of the trailing edge of the last dimple for $-$, 3 row; $--$, 2 row simulation,□, [1]; △, [2].

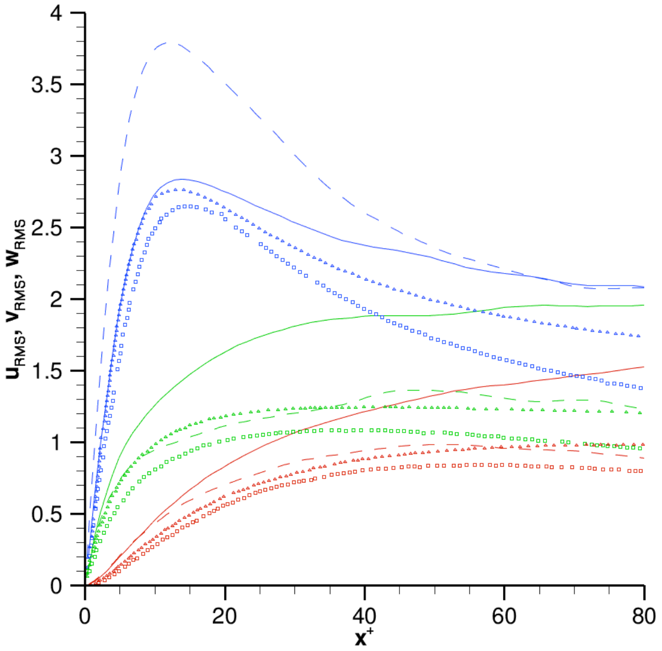

Figure 61. RMS velocity between the dimple rows at $z/D = 2.5$ downstream of the trailing edge of the last dimple for $-$, 3 row; $--$, 2 row simulation,□, [1]; △, [2].

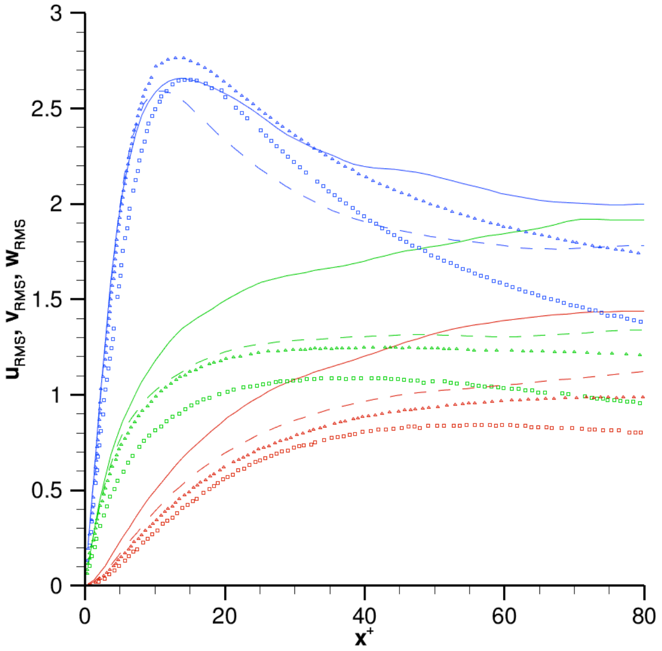

Figure 62. RMS velocity at the edge of the domain at $z/D = 2.5$ downstream of the trailing edge of the last dimple for $-$, 3 row; $--$, 2 row simulation,□, [1]; △, [2].

The boundary layer growth is much different in the presence of the third dimple. The plot of the boundary layer is shown for the three row simulation and the two row simulation in Figure 63. Again, the boundary layer growth as an ensemble averaged statistic is quite poor; instead breaking the growth at different characteristic locations across the span makes more sense, and is valuable in understanding how the boundary layer varies across the span in regions where the flow is more homogeneous in general. The three-row simulation correlates well with the growth to the middle of the first dimple, but begins to diverge from this solution just after the two-row configuration. The growth of θ follows the transition to turbulence as seen before, but has a bump as a result of the third dimple. After the third dimple θ increases at the same rate as the two-row configuration. The displacement thickness has a completely different trend as a result of the addition of a third dimple. After the third dimple the displacement thickness actually increases much sooner in contrast to the two row configuration where the δ^* decreases in the wake region until about $2D$ downstream where δ^* begins to increase when the flow is mixed enough in the wake. The addition of the third row increases the turbulent production to force the turbulent transition to occur further upstream.

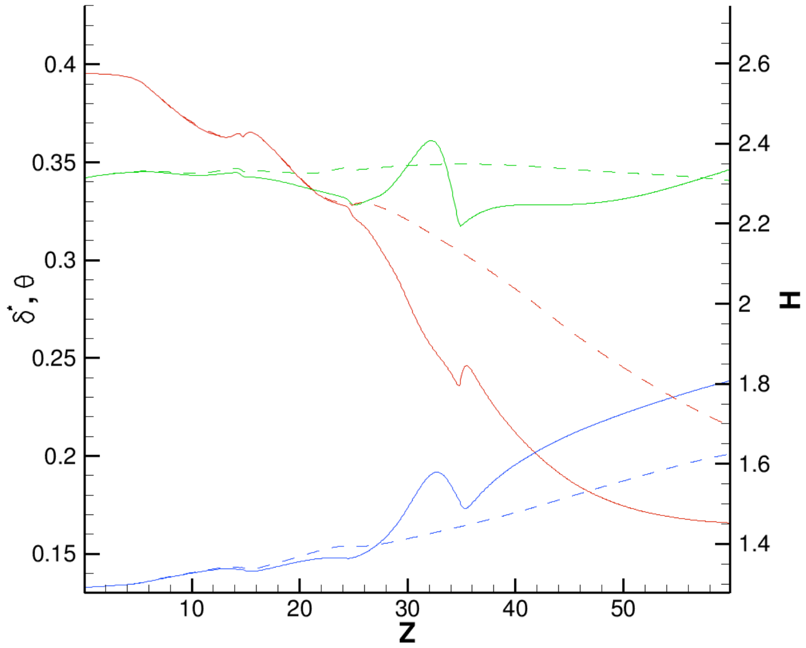

Figure 63. Displacement thickness, δ^*, momentum thickness, θ, and shape factor, H. $-$, 3-row simulation; $--$, 2-row simulation; δ^* and θ on left y-axis and H averaged in the span.

At the center of the span the shape factor, H, shows that the addition of the third row of dimples does not change the location where the flow appears fully transition. The momentum and the displacement thicknesses are larger with the addition of the third row. In the gap between the first and the third dimples the boundary layer statistics are much different as well. The boundary layer fluctuates with both δ^* and θ indicating that the third dimple is profoundly affecting the transition in the wake of the first dimple. Consistent with the results from the two-row simulation, the effect of a dimple downstream on the boundary layer causes the boundary layer to become thinner.

The boundary layer between the dimples at $y = 5$ shows the transition to turbulence occurs compared to the two-row simulation where it does not. Though the effects are similar from the first two dimples, the third dimple is causing the transition to occur across the span. Most interesting of this result is the effect the third dimple has on the displacement thickness shows how the boundary transitions at this location is similar to the transition at the center of the span. The boundary does not experience the acceleration at center of the dimples, but

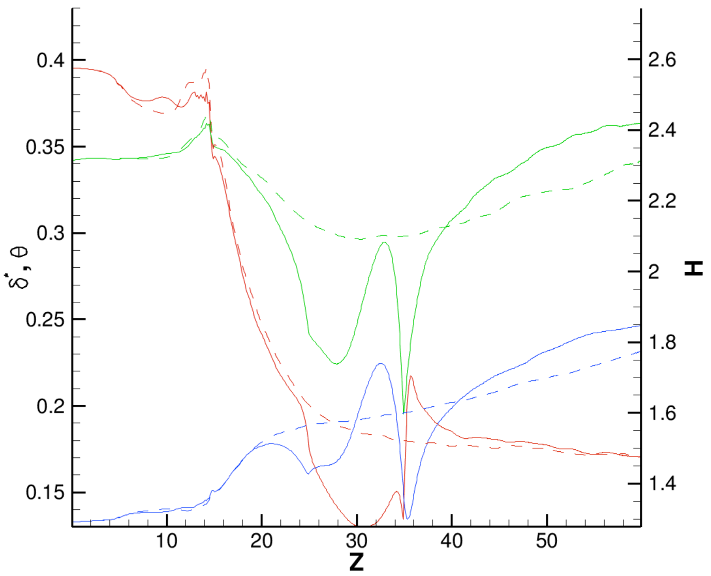

Figure 64. Displacement thickness, δ^*, momentum thickness, θ, and shape factor, H. $-$, 3-row simulation; $--$, 2-row simulation; δ^* and θ on left y-axis and H at $y = 0$.

still does experience the upward "bump" in δ^*. The transition in the location in the span does also occur at a much quicker rate than seen behind the first dimple in the two-row simulation or behind the second in either simulation. Transition occurs at about the same rate between the dimples as it does in the third wake.

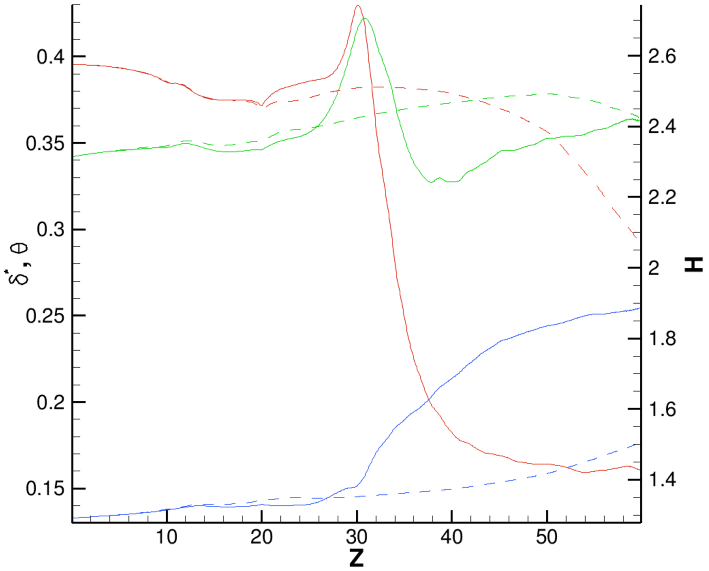

Figure 65. Displacement thickness, δ^*, momentum thickness, θ, and shape factor, H. $-$, 3-row simulation; $--$, 2-row simulation; δ^* and θ on left y-axis and H at $y = 5$.

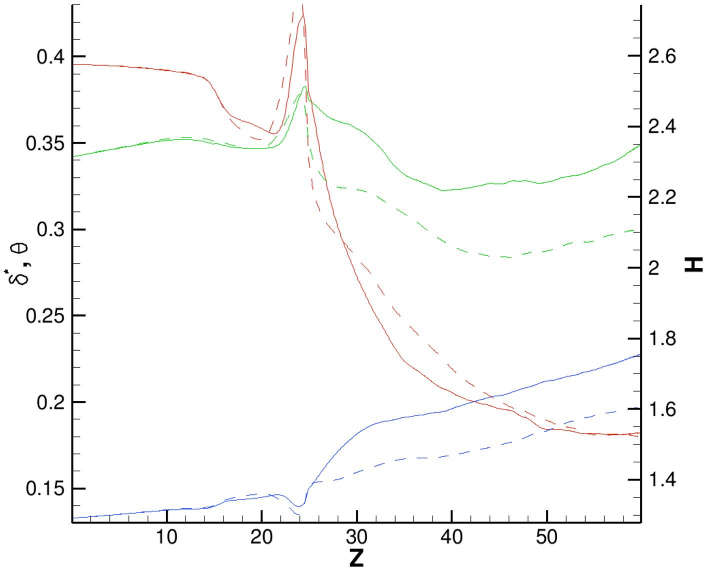

Figure 66. Displacement thickness, δ^*, momentum thickness, θ, and shape factor, H. $-$, 3-row simulation; $--$, 2-row simulation; δ^* and θ on left y-axis and H at $y = 10$.

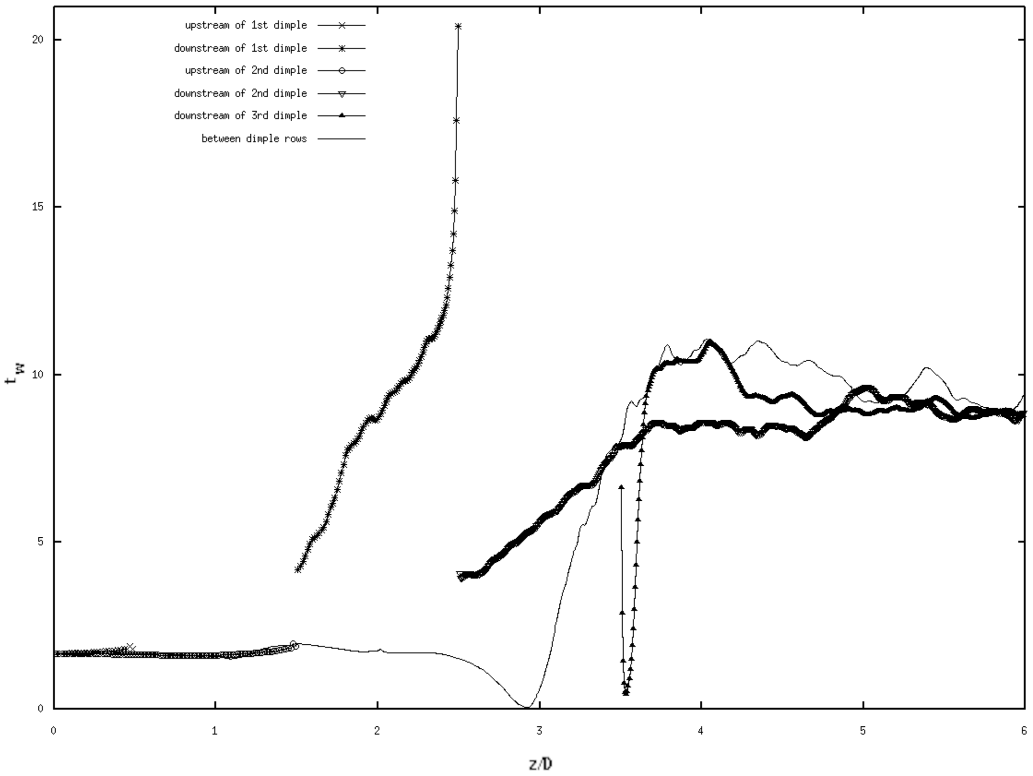

Figure 67. Wall shear stress, τ_W along the flat plate for the three-row simulation.

The wall shear stress is employed to understand the interaction of the boundary layer with the wall upstream and downstream of the dimples. The shear stress (shown in Figure 67) behind the first dimple in the wake region shows the same upward trend, but because there is a third row $1D$ behind this dimple the shear stress looks characteristically different immediately leading to the third dimple row. The effect of the third dimple on the flow can be seen as it squeezes the boundary layer down in the region before it causing the shear stress to spike very high compared to other locations in the boundary. In addition to the differences in the middle of the span due to the third dimple, it is clear that the third dimple is affecting the region behind the second dimple. The shear stress appears to level out at around $z/D = 3.5$ and then rise again to be equal to the rest of the domain at z/D =4.6 to 5 where the wakes converge. As well, instead of having two distinct wakes with a region of laminar flow as in the simulation with two dimple rows the entire span becomes turbulent with similar boundary layer characteristics across the span. The result shown in Figure 67 show that the third row is dominating the flow and forces the entire domain to transition to turbulence much quicker than with two dimple rows. There may be a point downstream of the domain in the two dimple simulation where this occurs, but it is clear that that the third dimple row forces the transition to turbulence to occur very quickly downstream (approximately $1.5D$). The boundary layer does not separate, but there are regions of low shear stresses located between the dimples where the dimple edge, and just downstream of the dimples. The stretching of the boundary layer as a result of the dimples is seen most dramatically immediately behind the third dimple, but can also be seen immediately behind the second dimple. The flow between the dimples at about the halfway downstream of the third dimple shows complete detachment of the flow. In the two row simulation the shear stress there was at the lowest point due to the dimples upstream, but here the third dimple dominates the boundary layer. This separation causes the flow between the dimples to transition faster than the transition behind the first dimple, but slower than the third. This is an important result to understanding how the cumulation of the turbulence causes rapid transition to turbulence due to the addition of dimples downstream.

The spanwise variation at the trailing edge of the last row of dimples is shown in Figure 69 and clearly shows a variation due to the dimples. In contrast to the 2-row simulation, the velocity far downstream of the dimples appears to be generally the same as shown in Figure 70 for $z = 60$. The profiles do not collapse as would be expected for a nominal turbulent boundary layer. Not only does the transition occur firther upstream, but the flow across the span of the domain becomes turbulent as is illustrated by the plots of the xy plane at $z = 60$ in Figure 70. As discussed previously, this is a result of the wakes not converging from the third dimple and the second dimple. The convergence of the wakes would be accelerated with the addition of a fourth dimple row behind the second, but the dimples may be spaced too far apart to directly impact the neighboring dimple columns. The contours in Figure 69 also show that immediately downstream of the dimple there is high velocity fluid very near the wall. The higher energy fluid does dissipate, but does create an effect of a bypass transition effect. The higher turbulent energized fluid in this region has the characteristic “top-down” transition mechanism seen in [24].

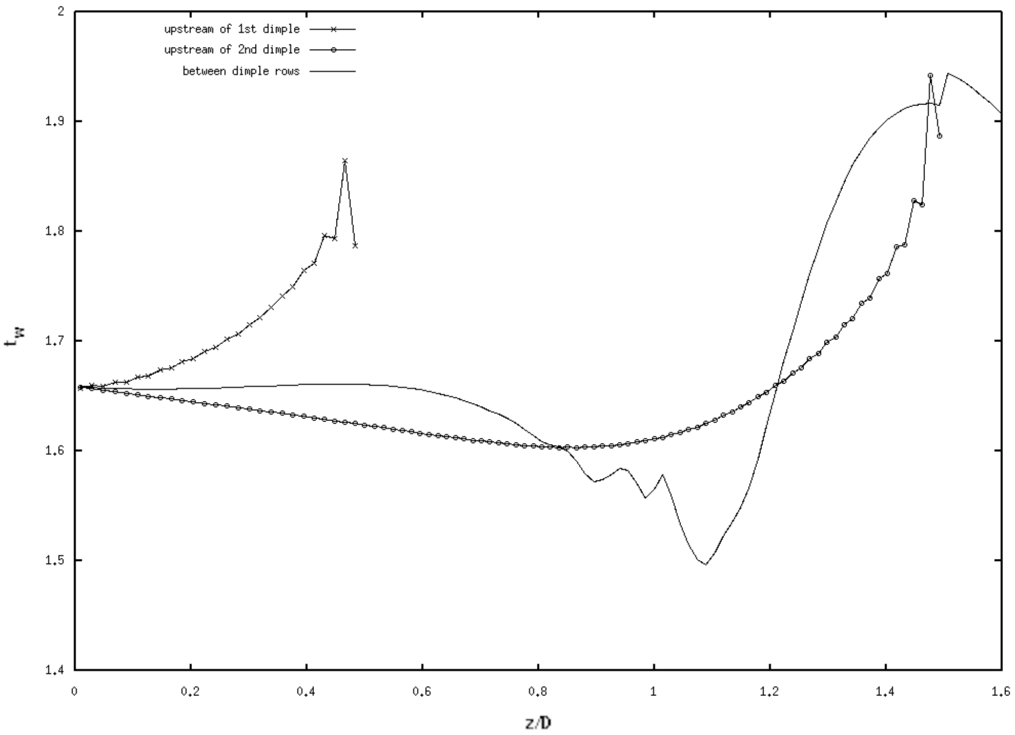

Figure 68. Wall shear stress, τ_W for the three-row simulation shows the same acceleration leading to the firs and second dimples.

Contours of streamwise velocity in Figure 69 show the influence of the dimples on the velocity, and as the flow moves downstream that influence is diminished significantly by the increase in turbulent production because of the addition of the third row. The plot of the velocity contours in a spanwise point of view does show some influence of the dimples still, but is reduced compared to the 2-row configuration. Addition of the third row of dimples causes more turbulent production which forces the fluid to become fully turbulent much further upstream.

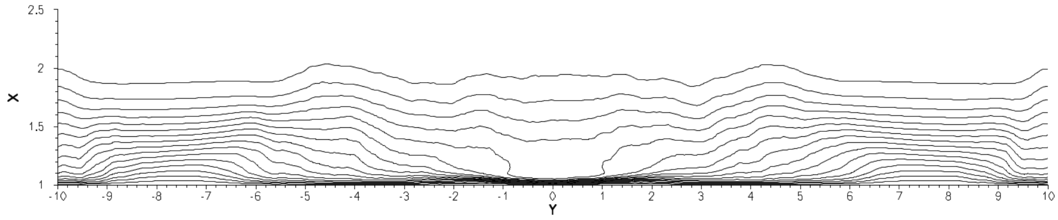

Figure 69. Streamwise velocity contours in an x-y plane at $z = 35$.

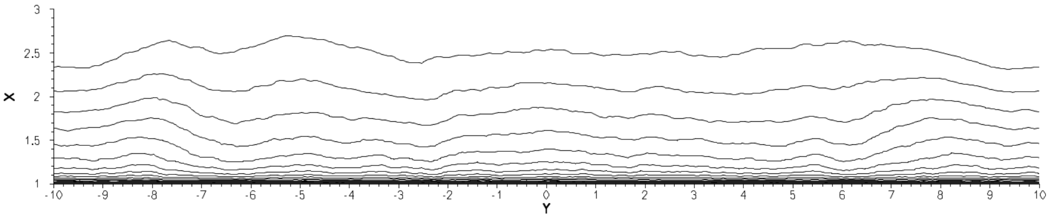

Figure 70. Streamwise velocity contours in an x-y plane at $z = 60$.

By adding the third dimple the boundary layer is forced to transition much further upstream, because the wakes due to the upstream dimples is forced to interact by disturbing the boundary layer already in transition. For the dimples the transitioning boundary layer is favorable to enhance the turbulent production, because there is higher velocity fluid to perturb closer to the wall. The result in the variation of the velocity at $z = 35$ shown in Figure 71 is biased by the dimples upstream, but the wake is not localized and is beginning to deteriorate into one larger wake of the entire array. Much further downstream the plot at $z = 60$ in Figure 72 shows turbulence that is almost completely isotropic in y. Addition of the third dimple induced the turbulence further upstream, which in turn has allowed the fully turbulent wake of the entire array to occur within the computational window. The cumulation of turbulence has a profound effect on the effectiveness in the level of the influence of the dimples on the boundary layer.

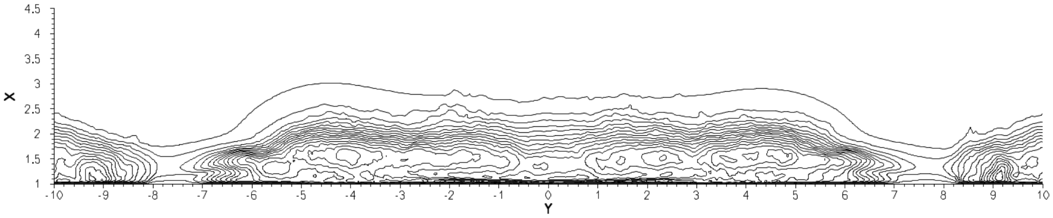

Figure 71. Streamwise RMS velocity in an x-y plane at $z = 35$.

Separation inside the first and second dimples appears to be unaffected by the presence of the third row of dimples. Reattachment of the boundary layer occurs in the upstream dimples on the trailing edge of the dimple in a the same way that occurs in the two row configuration. The flow is almost completely separated over the dimple, but the minimal direct interaction of the flow reattaching inside of the dimple leads to perturbation, which

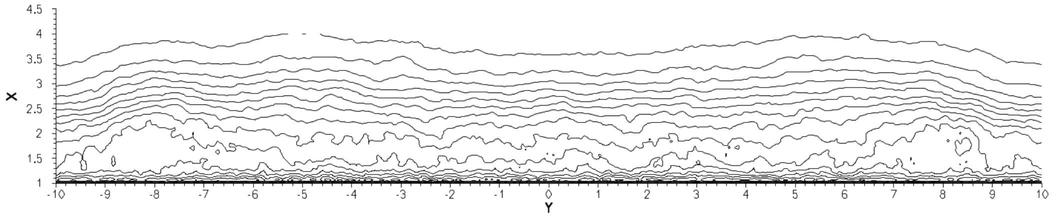

Figure 72. Streamwise RMS velocity in an x-y plane at $z = 60$.

in turn causes the flow to transition to turbulence downstream of the dimple as the two row simulation. It is important that the flow is already perturbed in the wake of the first dimple to increase the effect that the third dimple has on the flow. The separation in the second dimple is also larger in the second dimple than the first, and the reattachment point does occur further along in the dimple. This results again in a smaller perturbation of the boundary layer, and slower transition. For the present thesis, the boundary layer was chosen at the inlet to be the same length as the dimple depth. For a boundary layer that is thicker than that the transition seen in the dimples will be retarded. The transition in the second dimple is already much slower than the first dimple. A laminar boundary layer that is thinner will also interact with the dimple to cause transition, but the mechanisms may be completely different. With higher momentum fluid closer to the boundary layer, the flow detachment and reattachment can have a greater perturbation due to the dimple. Also of note for the present thesis, the geometry of the dimple interface with the flat plate has a sharp corner, whereas the dimples used in applications are typically manufactured to have a beveled edge. This may have implications on how the flow interacts with the edges of the dimples, but even with this in mind, the characteristics of how the boundary reattaches inside of the dimple and the boundary layer stretch at the trailing edge will remain the same though the intensity of this stretch may be reduced with a smoother transition of teh dimple to the flat plate.

The flow inside of the third dimple is informative of the overall cumulative effect of the dimples. The time averaged velocity shown in Figure 75 shows that the separation in the third dimple is almost non-existent in sharp contrast to the first and second dimple rows where most of the flow inside of the dimples is separated. The small separation region is

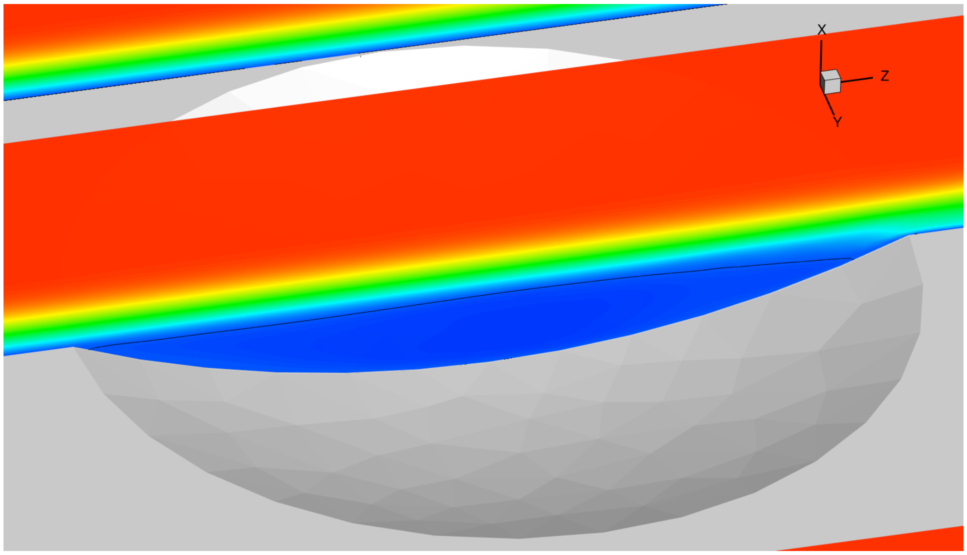

Figure 73. Streamwise time-averaged velocity contours with zero velocity contour line in the first dimple.

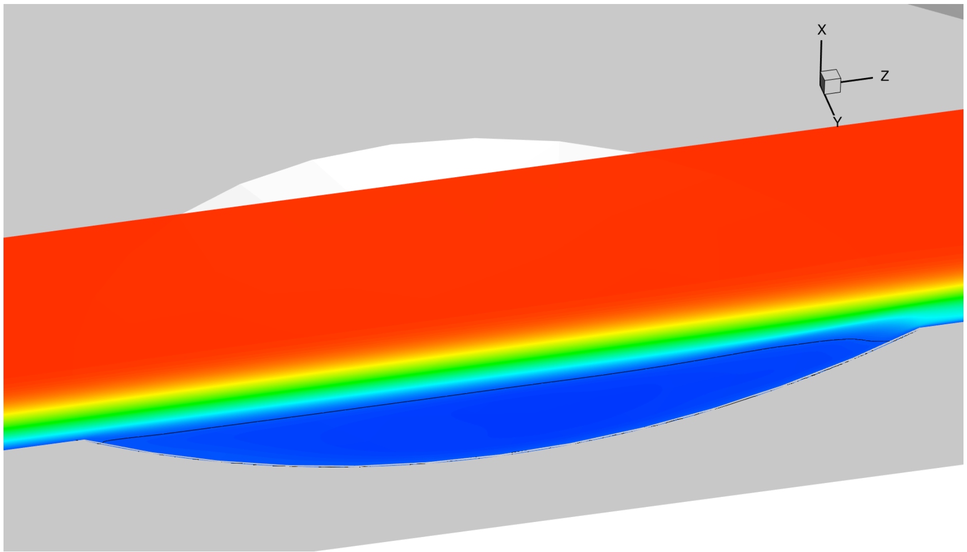

Figure 74. Streamwise time-averaged velocity contours with zero velocity contour line in the second dimple.

highlighted with a zero-velocity contour line as well in Figure 75. The separation is very small at the center of the dimple, but the perturbation on the boundary layer is coming mostly at the edge of the dimple. As the fluid is turned away from the wall at the trailing edge of the dimple the turbulence is forced away from the wall, and the boundary begins again at the edge of the dimple on the flat part of the wall. This insight is key into understanding how the boundary layer remains attached to the surface further downstream. Since the boundary is forced to reform it is inherently shallow, which means that the wall shear stress falls immediately after the dimple, but remains high and does not increase and separate as the wall shear stress drops to nil. The contours in Figure 76 show how the separation at the center of the dimple is minimal, as well as how the boundary layer stretches as the wall moves away from the flow. The boundary layer is very thin at the trailing edge of the dimple as the flow moves out of the dimple and back over the flat plate. The separation zone here will be minimized by a bevel on the edge of the dimple, but the sudden perturbation on the boundary layer will still occur as the wall inflects from a convex to concave shape into the flow.

Since the flow does not separate in the same manner as the first dimple the turbulent production is also much different. θ at the inlet of the third dimple is significantly higher and already beginning to transition to turbulence as a result of the first and second rows of dimples. The result seen in the third row is that the turbulent production occurs over the entire dimple and not as a perturbation due to the trailing edge. The color contours of time averaged streamwise velocity at the trailing edge of the third dimple in Figure 77. The small area of low velocity fluid is a region where the wall shear stress nominally drops just as the flow turns to the flat surface out of the dimple. The boundary layer beginning again is seen clearly here in this figure. Though not explored in the present thesis the proximity of dimples is of interest on the turbulent production.

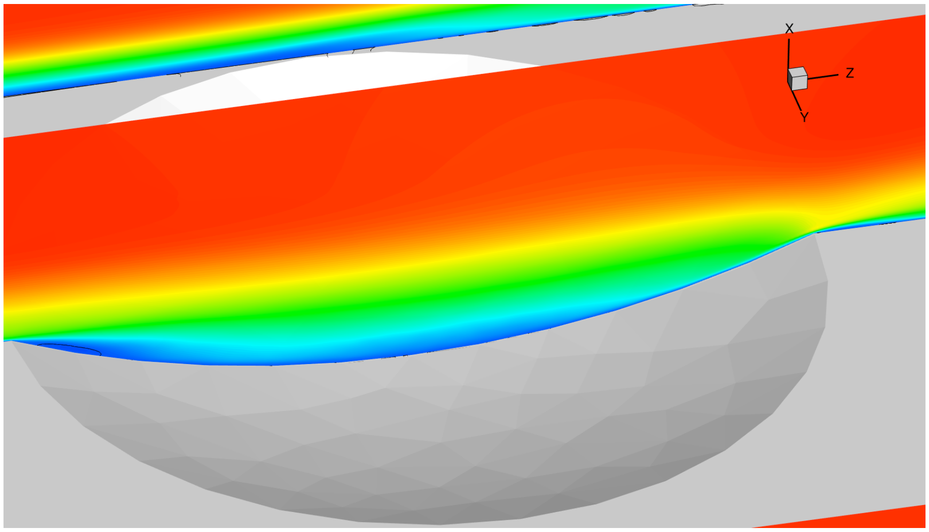

Figure 75. Streamwise time-averaged velocity contours with zero velocity contour line in the third dimple.

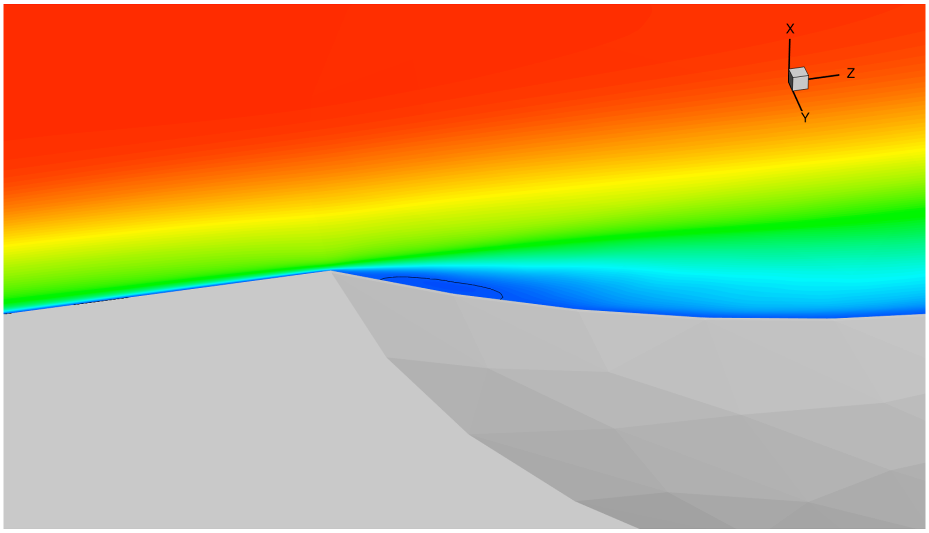

Figure 76. Streamwise time-averaged velocity contours with zero velocity contour line at the leading edge of the third dimple.

For the three-row simulation the flow paths inside of the dimple are the same as in the two-row simulation for the first and second dimples. The streamtraces in Figure 78 show how the flow enters the dimple and there are two large recirculation regions mirrored in the dimple. At the center of the leading edge the flow moves over the leading edge, but this is not part of the recirculation region. The recirculation regions are split at the center of the dimple in the span. The shape is not circular, but has an oblong shape, because of the

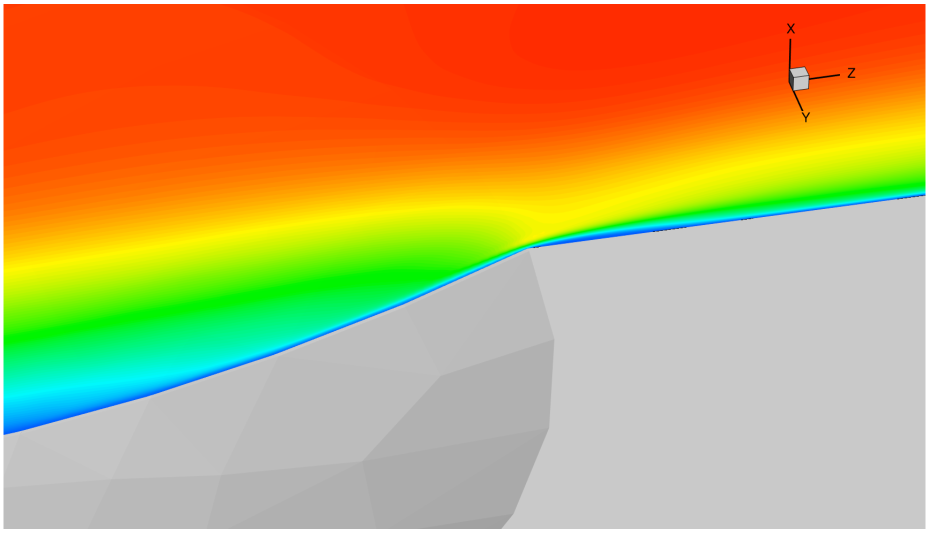

Figure 77. Streamwise time-averaged velocity contours with zero velocity contour line at the trailing edge of the third dimple.

reattachment on the trailing edge of the dimple. In three dimensions the stream traces show that deeper inside of the dimple the recirculation is further down in the dimple and as the further away from the wall of the dimple the recirculation is shorter as the flow reattaches inside of the dimple. The same characterisic flow is seen inside of the second dimple in Figure 79, but the recirculation is much larger, which is indicative of the flow separating for more of the dimple. This same structures and commonality is seen in the two-row simulation.

The streamtraces of the time averaged solution shown in Figure 80 still contain two main recirculation structures, but the reduction in the amount of time a fluid particle will remain inside of the dimple is significantly reduced, due to the amount of separation in the third dimple and the turbulence within the boundary layer already. This is indicated by the number of recirculation loops inside of the dimple, and the RMS velocity plot. Since the mean velocity has more influence inside of the dimple due to diminished separation flow there is essentially no prolonged recirculation though the dimple does cause the boundary layer to rotate over the streamwise dimension. Also not seen in the third dimple row is the turbulent production localized on the back wall of the dimple and the concentration of the flow to the center that occurs in the first and second rows. The flow exiting the dimple has

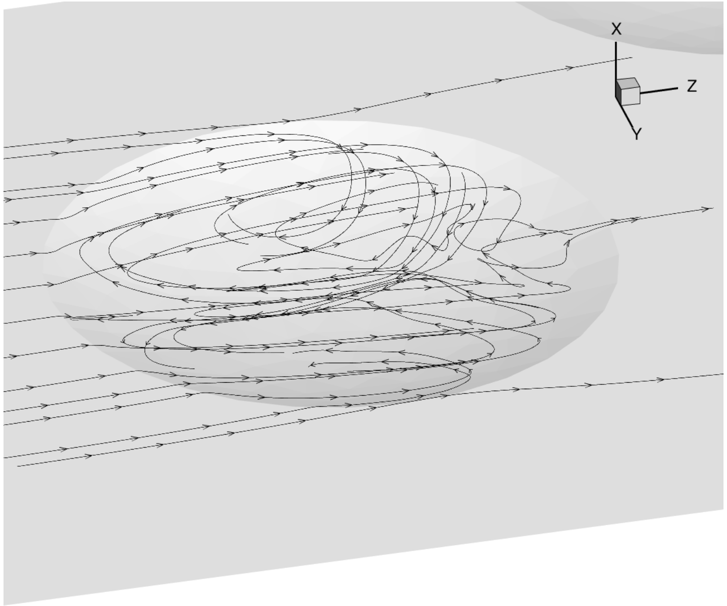

Figure 78. Streamtraces in the time averaged velocity field inside of in the first dimple.

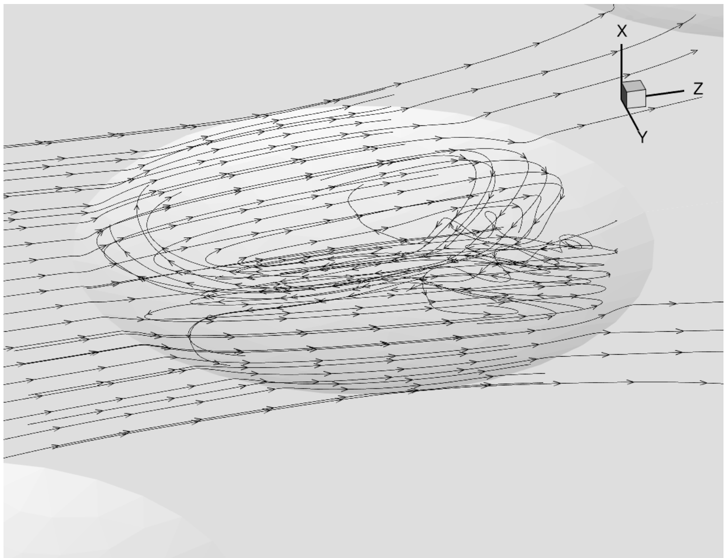

Figure 79. Streamtraces in the time averaged velocity field inside of in the second dimple.

a very strong spanwise component away from the center of the dimple. This will cause the flow over the entire span to transition much faster as the turbulent fluctuations are distributed through the span. The result is seen in the quickly transitioning flow between the dimples that was seen in the plots of the boundary layer statistics, and the RMS velocity contour planes along the length of the plate.

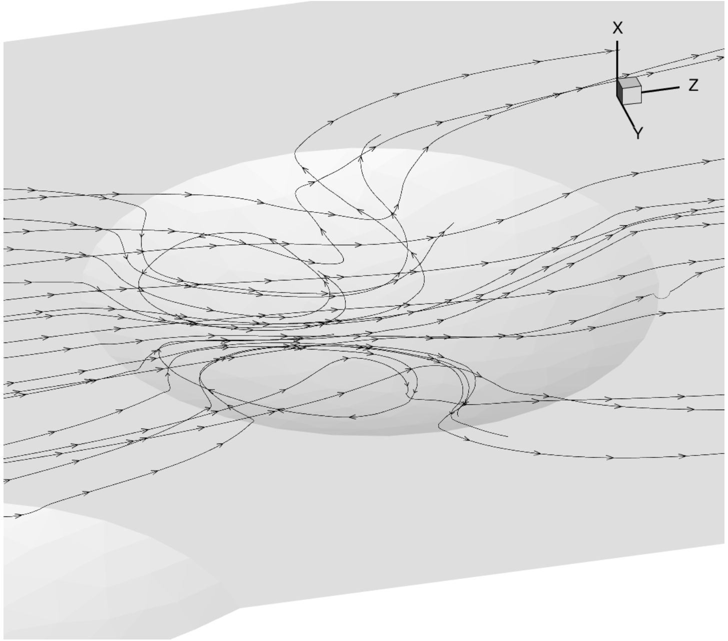

Figure 80. Streamtraces in the time averaged velocity field inside of the third dimple.

The plot of instantaneous streamwise velocity, w, contours in Figure 81 show the beginnings of fluctuations in the velocity field above the first dimple near the trailing edge propagate downstream and result in the flow transitioning to turbulence. The contours seen here highlight that the flow inside of the third row is turbulent and as a result the turbulent transition is forced upstream of the full transition by the second row of dimples. Between the dimples

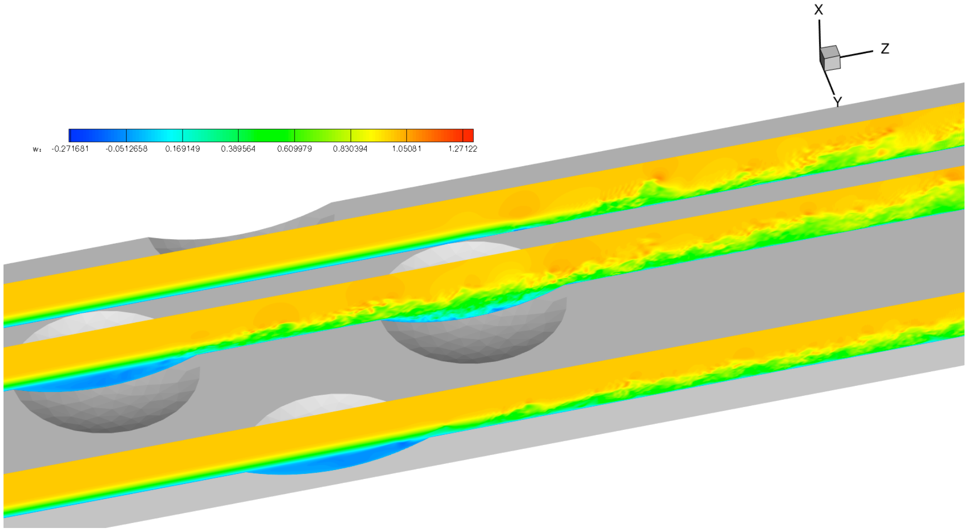

Figure 81. Contours of instananeous streamwise velocity at three planes in the span at $y = -5$, 0 and 10 from top to bottom, respectively.

The structures at the center of the span begin as fluctuations at the end of the first dimple, which perturb the boundary layer enough to initiate the transition just downstream of the dimple seen in Figure 82. The transition in the wake of the first dimple feeds into the the third dimple where the flow is transitioning to turbulence. In the wake of the first dimple just before the third dimple there are a number of very small fluctuations. These fluctuations are amplified by the third dimple as the flow passes over. In the two-row simulation the transition occurs behind the first dimple as a result of only the first dimple, but the transition behind the third dimple forced the turbulent transition to occur further upstream. These fluctuations grow into the turbulence in the wake of the dimples in the center of the span ($y = 0$). The contours in Figure 83 show the transition show smaller scales of turbulence at $1D$ downstream of the dimple. The plot here and for the two-row simulation in Figure 43 show the transition occurs in the same manner for both simulations. The influence of the third dimple into the wake of the second dimple does not extend directly behind the second dimple.

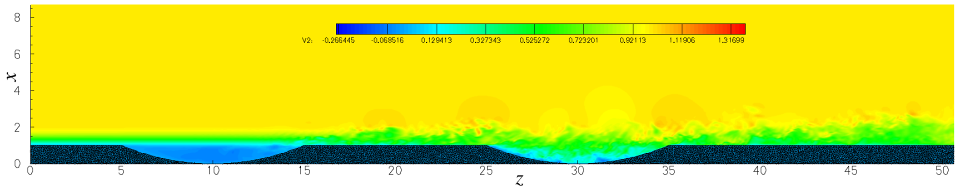

Figure 82. Contours of instananeous streamwise velocity in an x-y plane at $z = 0$.

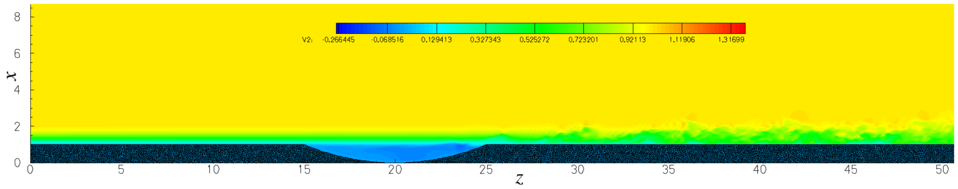

Figure 83. Contours of instananeous streamwise velocity in an x-y plane at $z = 10$.

The contours of velocity at x-y planes along the z-direction show how the turbulence propagates through the span. Behind the first dimple the flow remains quiescent except in the concentrated region in the wake of the first dimple. The contours here also highlight the recirculation regions. The separation is seen over the first and second dimples, and the two small regions on either side of the center of the third dimple. Also apparent in the third dimple is how the separation is localized at the upstream half of the dimple and by the trailing edge the boundary has reattached and is turbulent there. As the boundary layer devlops there are more large structures that exist as turbulent eddies. These structures are not existent near the dimples because of the level of perturbation just behind the dimple causing smaller structures to exist and diminish larger eddies until the flow becomes turbulent and regular structures are able to develop and form eddies that eject out of the boundary layer. These structures can be seen by visualizing the vortical structures. The turbulence propagates from the wake of the third dimple through most of the span. The flow structures in the wake of the third dimple show large eddies that exist in the boundary layer, and these structures homogenize through the span as the flow develops to a turbulent boundary layer.

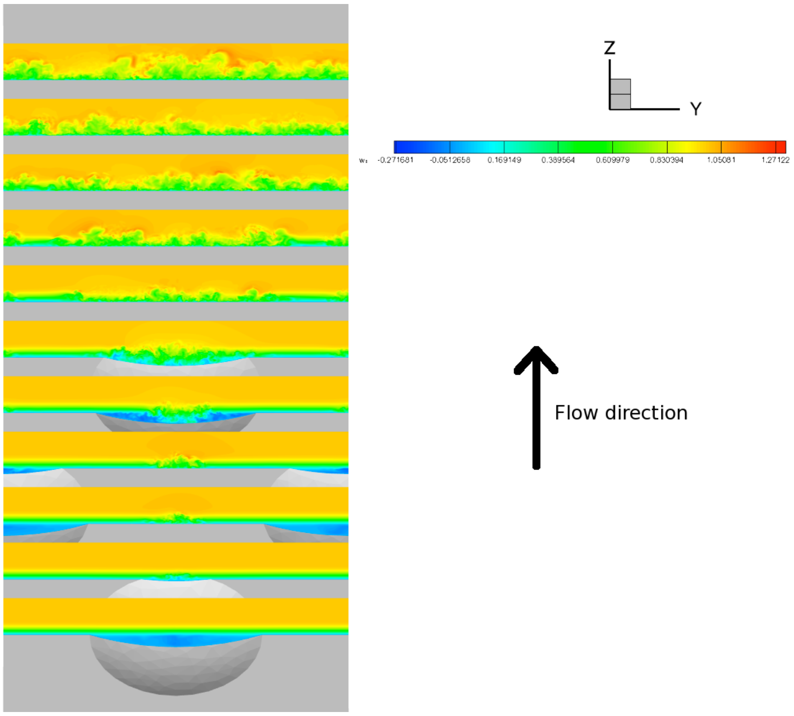

Figure 84. Contours of instananeous streamwise velocity in an x-y planes along the z-axis.

The isosurfaces of the Q-criterion shown in Figures 85 and 86 visualize the turbulent structures present in the flow field. The turbulence is concentrated in the wakes of the dimples as in the two-row simulation, but the transition spreads much faster across the span and is more intense particularly in the third dimple. The wake from the first dimple is also much wider than the second dimple due to the increased thickness of the boundary layer at the second dimple. The wake of the first dimple is also being affected by the presence of the third dimple downstream. As this turbulence is brought into the third dimple there is a significant increase in the turbulent production in the boundary. The flow inside of the third row is hardly separated, because the boundary layer has already begun transitioning upstream of the dimple. The turbulent production in the third dimple is forced outward in the span away from the dimple. This causes the turbulence to propagate through the span much further upstream than the two-row simulation. The wakes of all the dimples are mixed just downstream of the third dimple, and further upstream of the where the wakes converge in the two-row configuration. The flow on the plate exhibits structures that are indicative of turbulent boundary layer flows in both the two-row and three-row configuration [17].

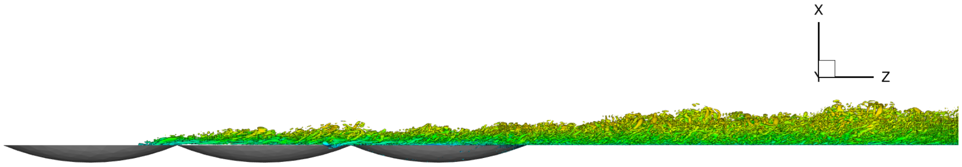

Figure 85. Q isosurface of 0.3 with color contours of streamwise velocity.

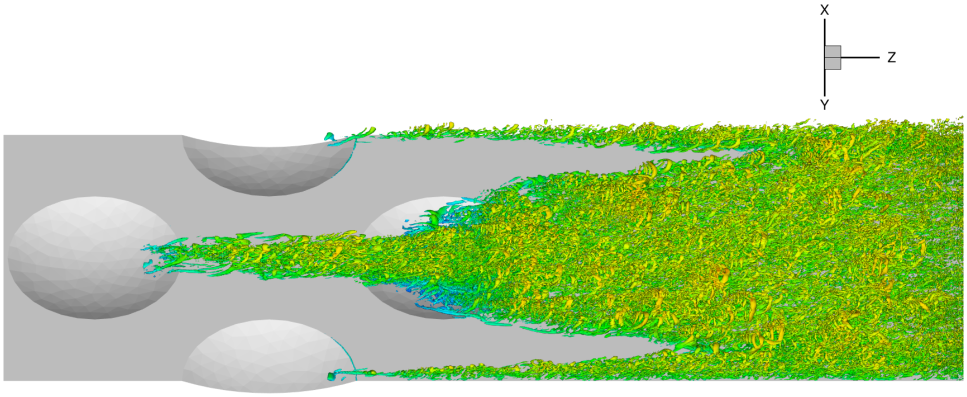

Figure 86. Q isosurface of 0.3 with color contours of streamwise velocity.

Looking closely there are hairpin vortical structures that are visualized by $Q = 0.3$ in Figure 85. These structures exist also in the turbulent boundary layer in the two-row simulation. Further examination shows the structure occurring in the region where the two wakes

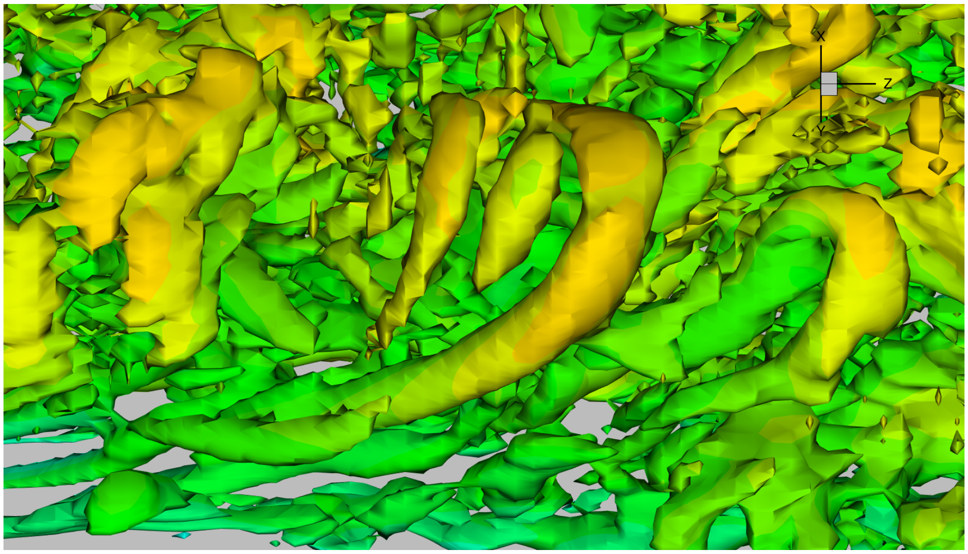

Figure 87. Hairpin vortices present in the turbulent boundary layer highlighted by using Q isosurface of 0.3.

meet between the second and third dimple rows. Plots in Figure 87 show the hairpin vortical structures occurring downstream of the intersection of the wakes from the second and third dimple rows. These structures exist in turbulent boundary layers and are a characteristic of how the turbulence interacts with the wall. As long streamwise vortical structures form pairs with voritcal structures of opposite sign, the structures turn away from the wall and form structures of this shape. The result on the velocity field from this shape causes lower velocity fluid near the wall to be ejected away from the wall. The growth of these structures is regular in the presence of a stable turbulent boundary layer. In the present thesis, these structures occur in the transition between laminar and turbulent boundary layers due to the nature of the transition imposed by the dimples. The dimples cause a high level of perturbation that is inducing high energy streamwise vorticial structures in the wall immediately downstream of the boundary. Also, the transition caused by the dimples is great enough to cause the transition to occur in the immediate wake of the dimples. In contrast the typical bypass transition studied implores the turbulence coming from outside of the boundary in the free stream, whereas in the present thesis the turbulence is coming from the interaction of the boundary layer and the wall. The presence of the turbulent energy in the boundary layer forces the transition to occur much faster, because the boundary itself is already contains the turbulent energy, whereas with free stream turbulence above the laminar boundary layer must disturb the boundary interaction with the wall for the transition to occur.

The streamwise vorticity contours in Figure 89 are plotted in x-y planes at z-locations along the length of the plate. The vorticity visualized in this plot again shows how the turbulence propagates through the wake of the dimples. The turbulence was seen to propagate rather quickly along the span the intense streamwise vorticity is moving through the span in the wake region of the dimples. The transition to turbulence can be identified across the span at different locations along z. In the fully turbulent flow the streamwise vortical structures will be present near the wall as seen in the wake, including between the dimples at approximately $y = 5$ downstream where the influence of the third dimple is causing the flow to transition. In addition the vorticity in the near wall region appears to be in +/- pairs which is indicative of longitudinal vorticities manifest for turbulence over flat plates [17].

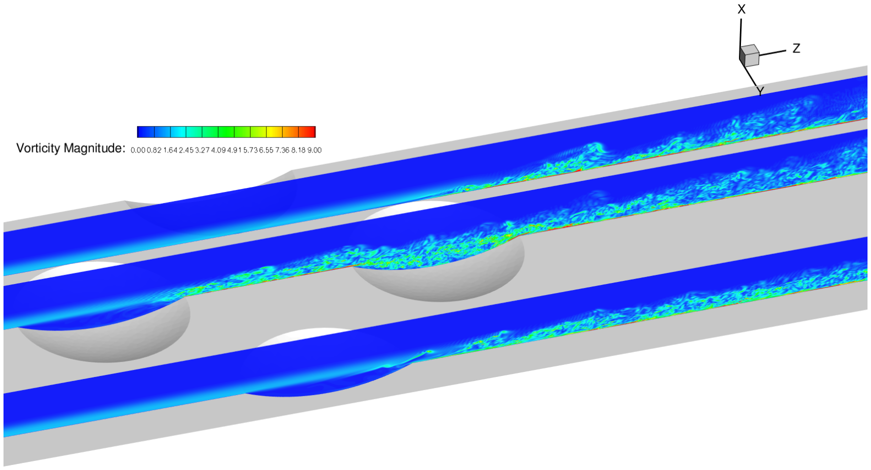

Figure 88. Vorticity magnitude at x-z planes through $y = -5$, 0, and 10. Contour level is from 0 to 10.

The three x-z planes in Figure 88 shows the how the vorticity develops in the center of the span, at the edge of the domain and between the dimple rows. The initiate of the turbulence at the edge of the first dimple shows small disturbances at regular intervals within the boundary layer. These short wavelength disturbances are a result of the structure of the flow within the dimple, and cause the boundary layer to transition immediately in the wake of the first dimple. In contrast, the second dimple shows a much different initiation mechanism because of the nature of the disturbances. The influence of the second dimple on the flow is by a long wavelength perturbation of the boundary layer. This disturbance results in a transition of the boundary layer that takes longer to develop than in the wake of the first dimple, because of the longer wavelength disturbance. The intensity of the energy by the second dimple is therefore less than that in the first dimple. Of course, the influence of the third dimple

The iso-surfaces of vorticity magnitude are used as another method of visualizing the turbulent transition in the flow field. Smaller structures seen in the flow above the third dimple is indicative of how the dimple in the presence of a turbulent boundary layer is forcing smaller high energy turbulence into the boundary layer. These are the vortical structures that cause the transition in the immediate wake. In Figure 90 the shape of the wake of the third dimple shows how the spanwise component out of the dimple influences the transition

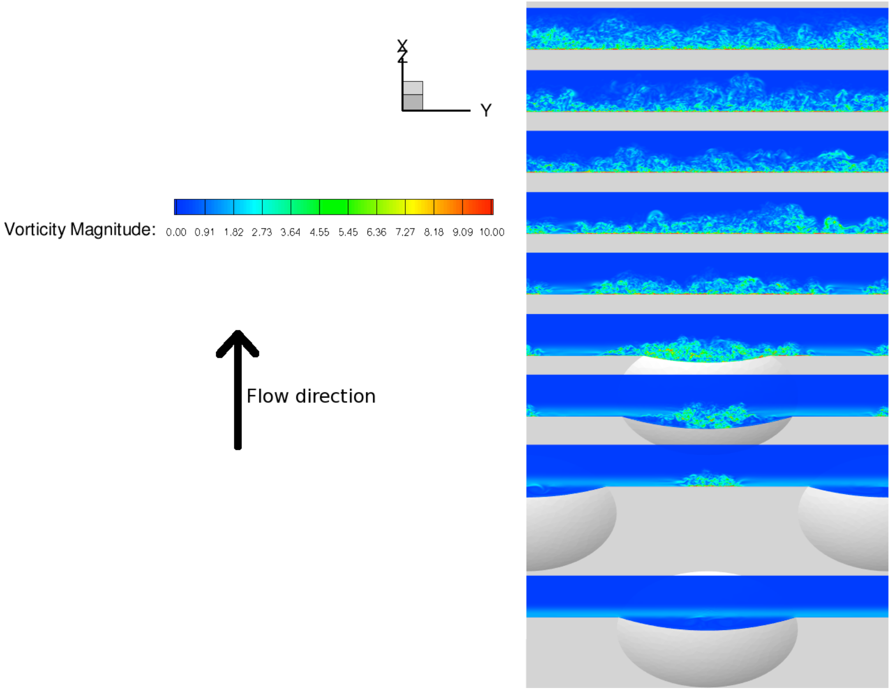

Figure 89. Streamwise vorticity contours at x-y planes along the z-axis.

of the entire span to a turbulent boundary layer. In Figure 91 the higher value of the vorticity shows the large longitudinal structures in the wakes. The structures, however, break over the third dimple, because the boundary layer over the dimple are broken apart. As the wakes converge the longitudinal structures in the near wall region start to develop toward the edge of the domain. As the wakes converge there is a quick convergence that happens as the influence causes the transition to occur as the vorticity on the edge of the wake influences the boundary layer to transition as the wake grows.

Smaller turbulent structures inside of the third dimple are seen in Figure 92 by visualization of the vorticity as before. The structures inside of the dimple are small and incoherent as the dimple is causing turbulent energy to break the structures seen in the wake of the first dimple. In turn this causes more of the boundary layer in the span to transition to turbulence in the wake of the third dimple. Visualization of the higher order vorticity shows how the fluid is turning on the edge of the dimple-plate interface as well as the longitudinal structures at the surface of the wall. These structures are indicative of the high level of vorticity on the wall. It is this level of vorticity, and the difference with the neighboring

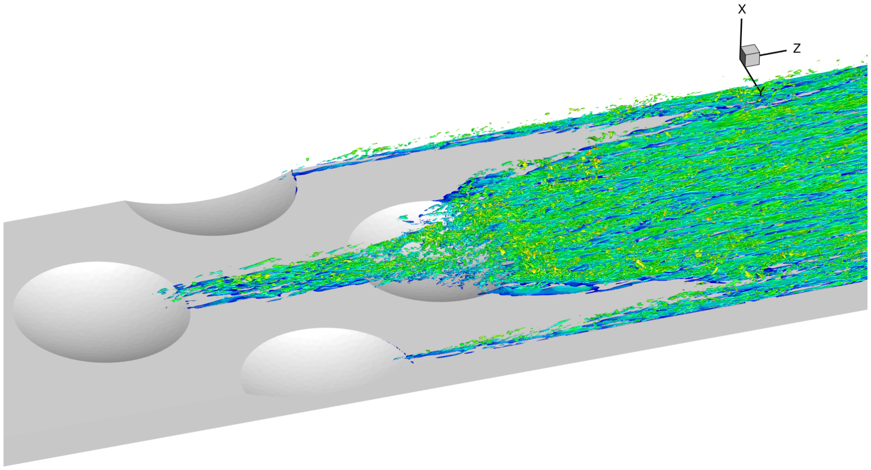

Figure 90. Vorticity magnitude isosurface of 5, with streamwise velocity color.

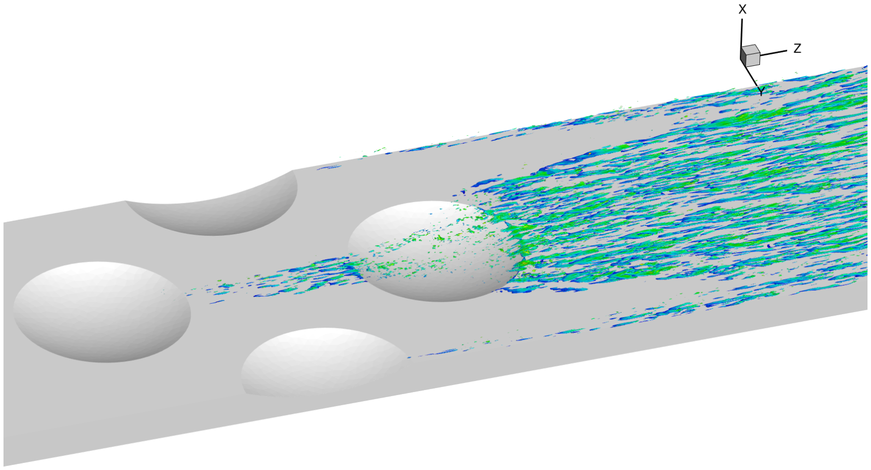

Figure 91. Vorticity magnitude isosurface of 10, with streamwise velocity color.

structures that cause the ejection of fluid away from the wall. As the transition seen in the present thesis highlights the effect of a bottom-up turbulent transition it is important to note how strong and how quick this influence is on the transition on the entire laminar flow into transition. By causing the transition at predictable localized regions the need to control the flow can be satisfied since the boundary layer can be predictable in the interaction with the surface.

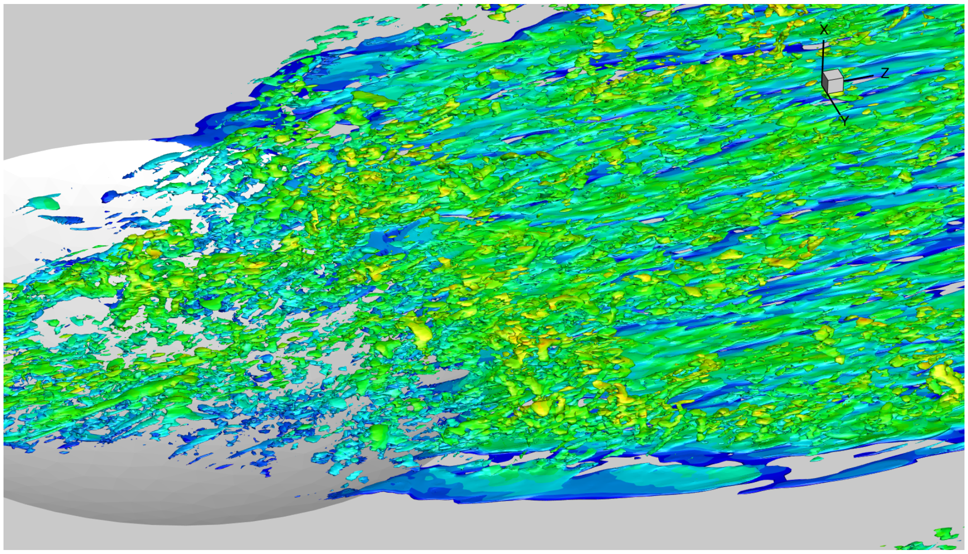

Figure 92. Vorticity magnitude isosurface of 5, with streamwise velocity color in the wake region illustrates turbulent structures in the third dimple vortices.

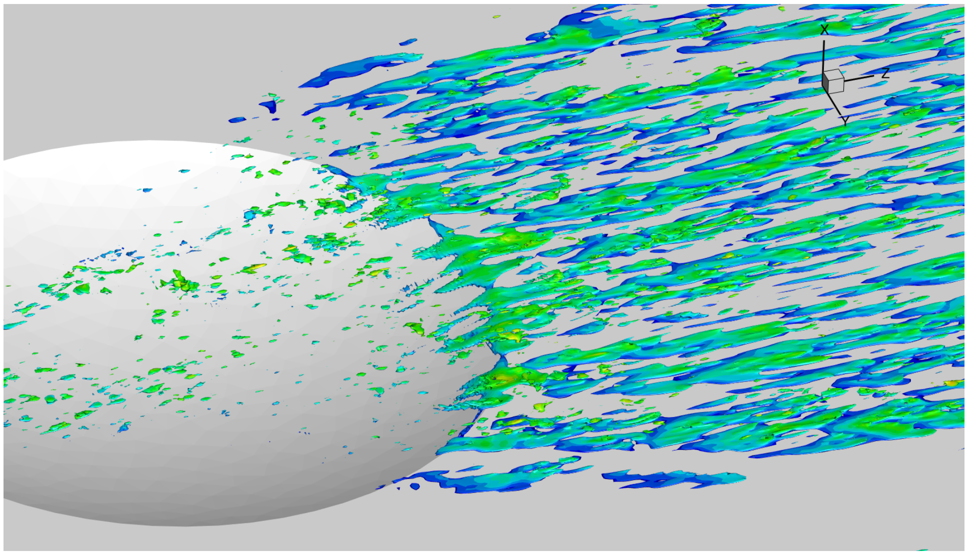

Figure 93. Vorticity magnitude isosurface of 10, with streamwise velocity color in the wake region to illustrate the surfaces on the dimple-plate interface.

VII. GRID CONVERGENCE STUDY

To verify the convergence of the grid two studies were performed to show the independence of the solution from the computational grid and interpolation of the boundary from the surface mesh. The first examination was of the influence of the surface mesh on the quality of the solution. The second was to study the independence of the solution from the fluid grid. Investigation of both w^+ and RMS velocity at a location downstream of the dimples.

A. Independence from the Surface Mesh

The first concern for the quality of the solution is the influence of the surface mesh on the solution. Since the boundary is interpolated onto the solution grid the approximation of the surface mesh as a representation of the geometry can cause errors if not refined enough. In order to evaluate the goodness of this approximation the surface mesh is refined to half the spacing between elements. Simulations with the same fluid grid used for the present thesis were computed with the finer surface mesh, which showed that the solution is independent of the surface mesh as can be seen in the plots of w^+ and RMS velocities in Figures 94 and 95, respectively. The solution downstream is unaffected by the size of the elements used. In general, the surface triangles need to be refined enough to represent the immersed boundary, but the surface used for the first simulations is accurate enough to capture the most important flow features in the present thesis. These results show that the solution is independent of the surface mesh.

B. Grid Refinement

To verify the independence of the solution from the Eulerian grid, the mesh is refined to determine if decreasing the spacing between points affects the accuracy of the solution. In most cases this is a straightforward task in the CFD field, but due to the complexity of the simulations in the present thesis the convergence is studied in a slightly different way. Using the same surface mesh, but using a refined grid is simple enough, but the computation time required to perform the calculation is astronomical compared to the solution already presented in this thesis. The wall-normal and spanwise grids must be refined globally, but it is impractical to refine the points in the streamwise direction globally. As such it

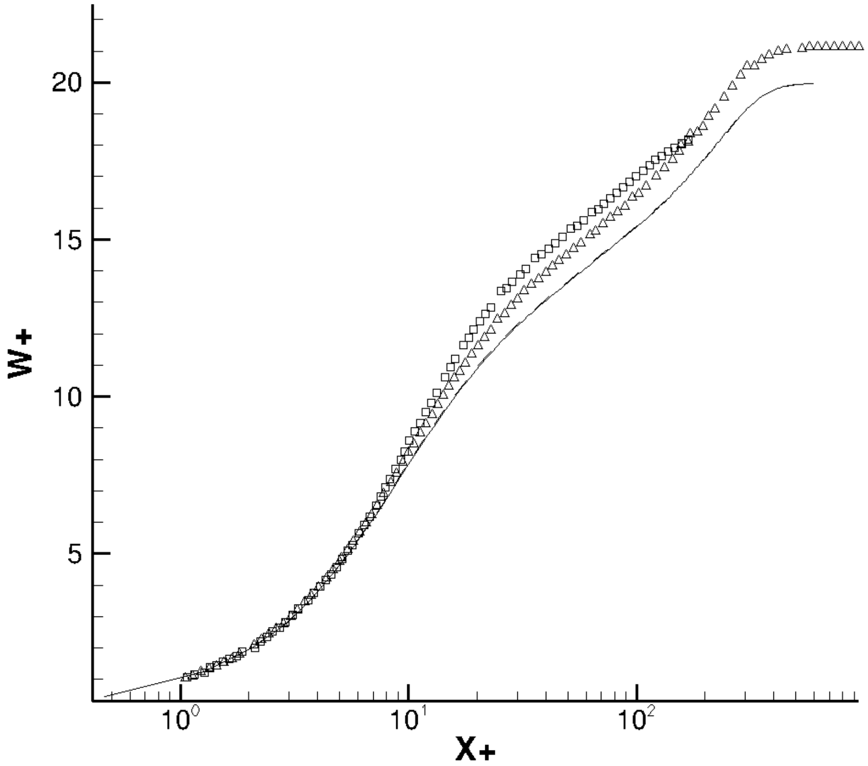

Figure 94. Mean velocity, w^+ vs. x^+ for three dimple rows. $-$, coarse surface mesh; $--$, fine surface mesh; $\square$, [1]; Δ, [2]

is required to use a test domain that is 1unit long in the streamwise, z, direction in the far wake of the solution to determine if the solution is independent. The spacing in the wall-normal and streamwise dimensions were of particular concern in the convergence of the fluid grid so the independence focused primarily on those two dimensions where the spacing was doubled in the near wall region for the wall normal dimension and doubled in the streamwise dimension for the $z = 59$ location. The domain in this location for the solution in the present thesis is $355 \times 322 \times 13$ and for the convergence test is $422 \times 386 \times 31$. In the interest of saving computational resources the spanwise dimension was not refined $2\times$ as the other two dimensions were. This was based off of the spacing in the spanwise dimension where the maximum Δy^+ value is 11.45, which is on the same spacing range as the solutions of the references in Table 1 of values ranging from 5 to 15.

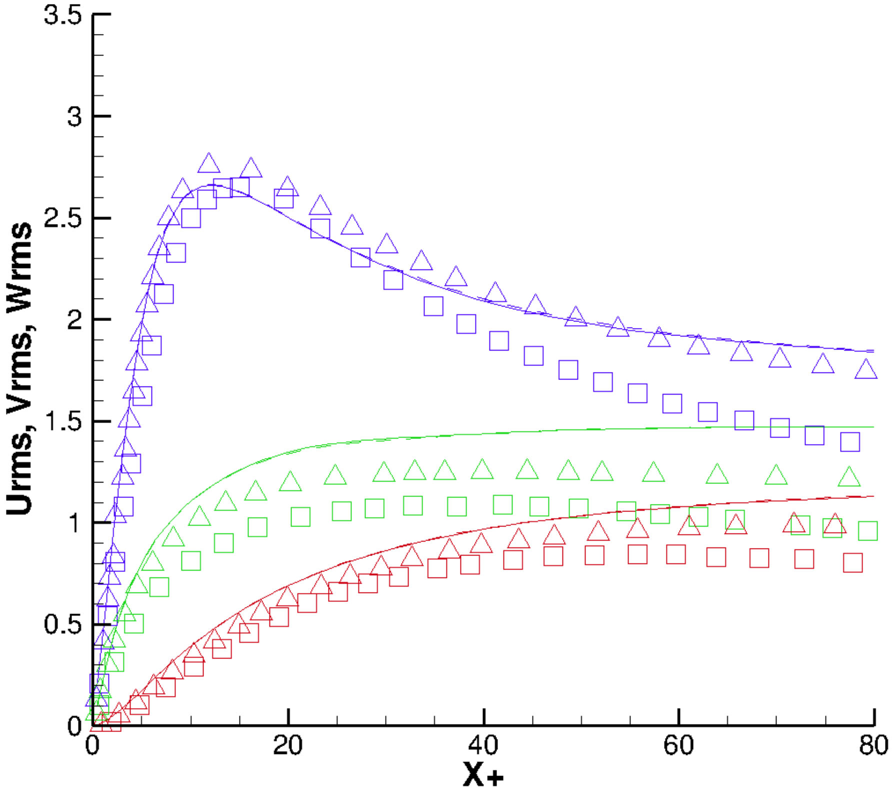

Figure 95. RMS velocity for three dimple rows. $-$, coarse surface mesh; $--$, fine surface mesh; □, [2]; △,[1].

For DNS, grid refinement is straightforward in terms of addition of points in the boundary, but the effective use of the computational resources is always a top priority. The IB method in the present thesis also makes changing the grid simple as the grid can be altered without having to smooth the grid around a curved geometry as would be require without the use of an IB. The plots of w^+ and RMS velocities in figures 96 and 97, respectively, show that there is a large difference in the resolution of the turbulence between grids 2 and 3, and a smaller yet still significant difference between grid 3 and the refined grid. The domain in the spanwise dimension was reduced by half from grid 1 to grid 2 in the interest on concentrating computational resources on a smaller part of the domain. Though the grid influence is significant from grid 2 to grid 3 the results do show that there is no influence from the periodic condition. Determination of how well the grid is resolving turbulence must now rely solely on the grid spacing in wall units. Based upon values from literature the grids used for the simulations are just sufficient enough. The grid spacing in the streamwise direction for the three row simulation is on the higher side of the range used in other DNS work, but should be in the zone for understanding the basic flow properties inherent with flow over the dimples. The values for the grid spacing near the wall is tabulated once again in Table3.

The results presented in the present thesis were computed on grid 3. The grid was chosen such that the grid would not influence the solution. This is done by having enough points to resolve the viscous sublayer, which is approximately the nearest wall region where $x+ < 5$ and having a small enough grid spacing to resolve all scales of turbulence to not cause aliasing of the turbulence. The plot in Figure 96 show that the velocity from the solution over grid 3 is independent of the grid, especially compared to grid 2. The plots in Figures 97, 98, and 99 show w_{RMS}, u_{RMS}, and v_{RMS}, respectively, to show how independent the solution is from the grid. The impact of the second grid to the third is quite significant, and the influence of the grid is still seen from the third grid. This indicates that the turbulent intensity in the solutions presented in the present thesis is being over-predicted. Since the solution is still showing influence from the grid, the simulation should be run with a more refined grid that can show independence in order to capture the turbulence properly for DNS.

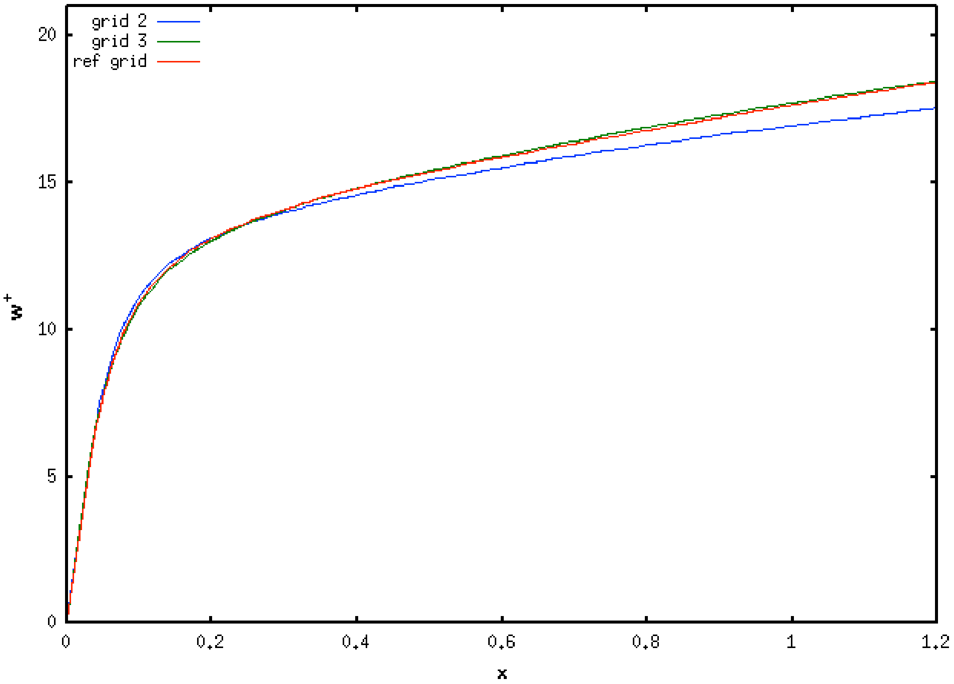

Figure 96. Mean velocity, w^+ vs. x for three dimple rows.

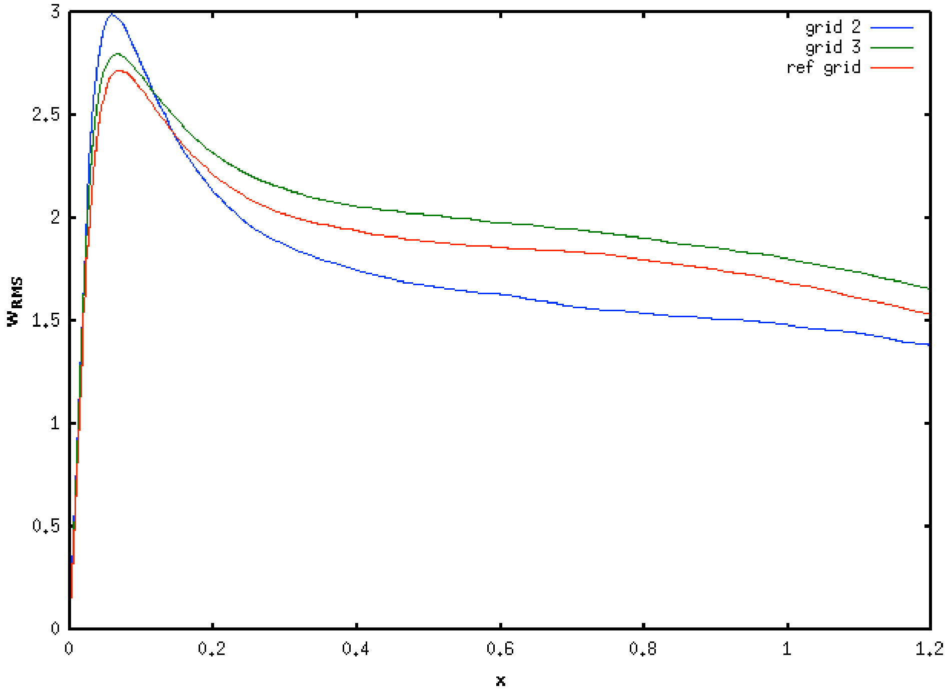

Figure 97. w_{RMS} velocity for three dimple rows.

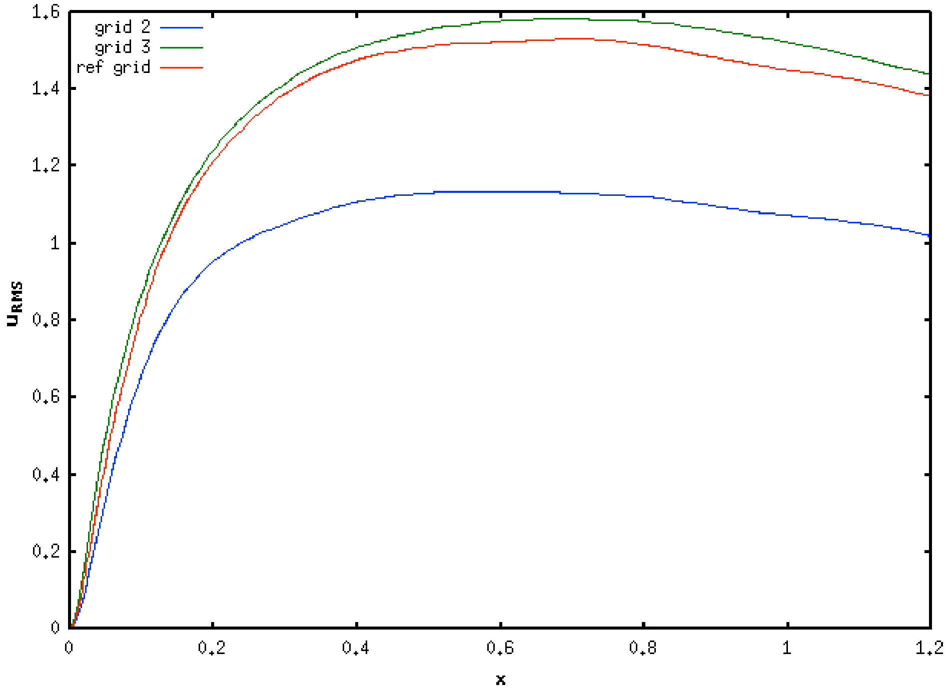

Figure 98. u_{RMS} velocity for three dimple rows.

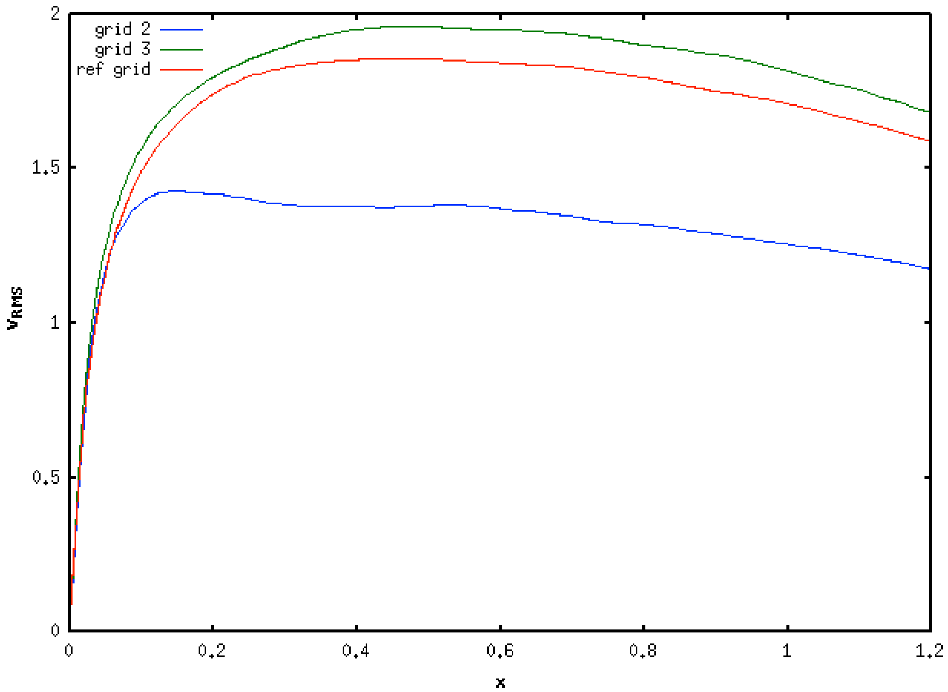

Figure 99. v_{RMS} velocity for three dimple rows.

Table 3. Grid refinement with wall unit values for 3 dimple row simulations used for grid refinement

Grid	1^*	2	3
Min Δx^+ for 3 rows	6.71	1.24	0.80
Max Δy^+ for 3 rows	55.73	32.50	12.42
Max Δz^+ for 3 rows	27.78	31.09	16.56
Min Δx^+ for 2 rows		1.20	0.74
Max Δy^+ for 2 rows		31.46	11.45
Max Δz^+ for 2 rows		30.75	15.51

* Time averaging was not performed for two dimple configuration using grid 1.

VIII. SUMMARY

A. Conclusions

In this thesis, it has been shown that the influence of the dimples on the boundary layer is clear in that it forces transition to turbulence from a laminar boundary layer by imposing fluctuations at the trailing edge of the dimples in the laminar regime and amplify the effectiveness of the transition in the presence of turbulence. As a result, the flow observed transitions in the wake and is generally like a turbulent boundary layer as the wake grows far downstream of the dimples. Periodicity evident in the wake of the dimple indicates influence similar to flow over an open cavity causes a turbulent spot to initiate transition.

Addition of a third row of dimples shows that there is a cumulative effect of the influence of the dimples on the turbulent production. Higher energy fluid interacts with the dimples as a result of the dimple upstream, and allow the third dimple to increase the turbulent energy much more than the dimples upstream. The boundary layer separates in a smaller region in the third dimple, and plots of the RMS velocity in the streamwise dimension coupled with the plots of Q show that turbulent production is higher inside of the third dimple compared to the first two dimple rows.

B. Future Work

Further investigation is required into the dimple as a cavity with emphasis on shape of the dimple itself and how this influences vortex shedding in relation to modes that initiate transition within the dimples. This will shed light into how the shape of the dimples i.e. aspect ratio influences the level of turbulent production by the dimples. Finally, addition of more rows of dimples needs to be investigated for a thorough analysis of the cumulative effect of having dimples. The question as to whether there is a limit to the number of dimples that will influence the boundary layer in the streamwise dimensions remains unanswered, as it is definitely more than three staggered dimple rows. From the results of the grid independence study, more refined mesh in the wall-normal and streamwise dimensions in order to fully resolve the turbulent structures.

References

[1] Kim, J., Moin, P., and Moser, R., "Turbulence Statistics in Fully Developed Channel Flow at Low Reynolds Number," *Journal of Fluid Mechanics*, Vol. 177, 1987, pp. 133–166.

[2] Wu, X. and Moin, P., "Direct Numerical Simulation of Turbulence in a Nominally Zero-Pressure-Gradient Flat-Plate Boundary Layer," *Journal of Fluid Mechanics*, Vol. 630, 2009, pp. 5–41.

[3] Ansys, "Fluent NEWS - Spring 04 - Speedo Goes for Gold with CFD," 2004, [http://www.fluent.com/about/news/newsletters/04v13i1/a1.htm. Accessed 11/3/2010.].

[4] Casey, J. P., *Effect of Dimple Pattern on the Suppression of Boundary Layer Separation on a Low Pressure Turbine Blade*, Master's thesis, Air Force Institute of Technology, WPAFB, OH, March 2004.

[5] Bruneau, C.-H. and Mortazavi, I., "Numerical Modelling and Passive Flow Control Using Porous Media," *Computers & Fluids*, Vol. 37, 2008, pp. 488–498.

[6] Bernard, P. S. and Wallace, J. M., *Turbulent Flow*, John Wiley & Sons, inc, Hoboken, New Jersey, 1st ed., 2002.

[7] Spalart, P. R., "Direct Simulation of a Turbulent Boundary Layer Up to R_Θ = 1410," *Journal of Fluid Mechanics*, Vol. 187, 1988.

[8] Kim, J. and Moin, P., "Application of a Fractional-Step Method to Incompressible Navier-Stokes Equations," *Journal of Computational Physics*, Vol. 59, 1985, pp. 308–323.

[9] Jiménez, J. and Moin, P., "The Minimal Flow Unit in Near-Wall Turbulence," *Journal of Fluid Mechanics*, Vol. 225, 1991, pp. 213–240.

[10] Le, H., Moin, P., and Kim, J., "Direct Numerical Simulation of Turbulent Flow Over a Backward-Facing Step," *Journal of Fluid Mechanics*, Vol. 330, 1997, pp. 349–374.

[11] Spalart, P. R. and Strelets, M. K., "Mechanisms of Transition and Heat Transfer in a Separation Bubble," *Journal of Fluid Mechanics*, Vol. 403, 2000, pp. 329–349.

[12] Ligrani, P. M., Harrison, J. L., Mahmmod, G. I., and Hill, M. L., "Flow Structure Due to Dimple Depressions on a Channel Surface," *Physics of Fluids*, Vol. 13, No. 11, November 2001, pp. 3442–3451.

[13] Park, J. and Ligrani, P. M., "Numerical Predictions of Heat Transfer and Fluid Flow Characteristics for Seven Different Dimpled Surfaces in a Channel," *Numerical Heat Transfer*, Vol. 47, 2005, pp. 209–232.

[14] Park, J., Desam, P. R., and Ligrani, P. M., "Numerical Predictions of Flow Structure Above a Dimpled Surface in a Channel," *Numerical Heat Transfer*, Vol. 45, 2004, pp. 1–20.

[15] Mahmmod, G. I. and Ligrani, P. M., "Heat Transfer in a Dimpled Channel: Combined Influence of Aspect Ratio, Temperature Ratio, Reynolds Number, and Flow Structure," *International Journal of Heat and Mass Transfer*, Vol. 45, No. 10, May 2002, pp. 2011–2020.

[16] Saini, R. and Verma, J., "Heat Transfer and Friction Factor Correlations for a Duct Having Dimple-Shape Artificial Roughness for Solar Air Heaters," *Energy*, Vol. 33, 2008, pp. 1277–1287.

[17] Adrian, R. J. and Meinhart, C., "Vortex Organization in the Outer Region of the Turbulent Boundary Layer," *Journal of Fluid Mechanics*, Vol. 422, 2000, pp. 1–54.

[18] Mahmood, G. I., Hill, M. L., Nelson, D. L., Ligrani, P. M., Moon, H.-K., and Glezer, B., "Local Heat Transfer and Flow Structure on and Above a Dimpled Surface in a Channel," *ASME Journal of Turbomachinery*, Vol. 123, January 2001, pp. 115–123.

[19] Kanokjaruvijit, K., Thawonngamyingsakul, C., and Wongwises, S., "Numerical Investigation of an Axi-symmetric Laminar Jet Impinging on a Dimpled Surface Under Uniform Heat Flux Using a Finite Element Method," *Journal of Mechanical Science and Technology*, Vol. 24, May 2010, pp. 1809–1818.

[20] Smith, C., Beratlis, N., Balaras, E., Squires, K., and Tsunoda, M., "Numerical Investigation of the Flow Over a Golf Ball in the Subcritical and Supercritical Regimes," *International Journal of Heat and Fluid Flow*, Vol. 31, 2010, pp. 262–273.

[21] Choi, J., Jeon, W., and Choi, H., "Mechanisms of Drag Reduction by Dimples on a Sphere," *Physics of Fluids*, Vol. 18, April 2006.

[22] Bearman, P. W. and Harvey, J. K., "Control of Circular Cyninder Flow by the Use of Dimples," *AIAA Journal*, Vol. 31, No. 10, October 1993, pp. 1753–1756.

[23] Zaki, T. A. and Durbin, P. A., "Continuous Mode Transition and the Effects of Pressure Gradient," *Journal of Fluid Mechanics*, Vol. 563, 2006, pp. 357–388.

[24] Jacobs, R. G. and Durbin, P. A., "Simulations of Bypass Transition," *Journal of Fluid Mechanics*, Vol. 428, 2001, pp. 185–212.

[25] Zaki, T. A. and Durbin, P. A., "Mode Interaction and the Bypass Route to Transition," *Journal of Fluid Mechanics*, Vol. 531, 2005, pp. 85–111.

[26] Andersson, P., Berggren, M., and Henningson, D. S., "Optimal Disturbances and Bypass Transition in Boundary Layers," *Physics of Fluids*, Vol. 11, No. 1, 1999, pp. 134–150.

[27] Balaras, E., "Modeling Complex Boundaries Using an External Force Field on Fixed Cartesian Grids in Large-Eddy Simulations," *Computers & Fluids*, Vol. 33, 2004, pp. 375–404.

[28] White, F., *Viscous Fluid Flow*, McGraw-Hill, 3rd ed., 2006.

[29] Panton, R. L., *Incompressible Flow*, John Wiley & Sons, inc, Hoboken, New Jersey, 3rd ed., 2005.

[30] Balaras, E. and Yang, J., "Nonboundary Conforming Methods for Large-Eddy Simulations of Biological Flows," *ASME Journal of Fluids Engineering*, Vol. 127, September 2005.

[31] Yang, J. and Balaras, E., "An Embedded-Boundary Formulation for Large-Eddy Simulation of Turbulent Flows Interacting with Moving Boundaries," *Journal of Computational Physics*, Vol. 215, 2006, pp. 12–40.

[32] Smits, A. and Wood, D., "The Response of Turbulent Boundary Layers to Sudden Perturbation," *Annual Review of Fluid Mechanics*, Vol. 17, 1985, pp. 321–358.